

New Methods of Improving the Orbit Determination and Stability at LEP

Von der Mathematisch-Naturwissenschaftlichen Fakultät
- Fachbereich 1 -
der Rheinisch-Westfälischen Technischen Hochschule Aachen
zur Erlangung des akademischen Grades
eines Doktors der Naturwissenschaften
genehmigte Dissertation

Vorgelegt von

Diplom-Physiker
Frank Andreas Tecker
aus Haan

Referent: Privatdozent Dr. Manfred Tonutti
Korreferent: Universitätsprofessor Dr. A. Böhm
Tag der mündlichen Prüfung: 26. Juni 1998

Abstract

The orbit quality is of particular importance for a good performance of an accelerator. Beam parameters like the interaction rate of a collider or the level of spin polarization strongly depend on the orbit. Two new methods to improve the orbit measurement and stability are demonstrated.

The beam position monitors in an accelerator are carefully aligned to the centres of the quadrupole magnets. A residual mechanical but also electronical offset can persist. This offset is measured by a beam based alignment method developed at LEP. The method and its installation are described. Measurement procedures as well as results for different magnet types and BPM electronics are shown. The impact of the BPM offsets on the achievable spin polarization level is outlined.

The vertical orbit has shown large variations during LEP operation. Frequent orbit corrections were required to avoid a decrease of the interaction rate. Low-beta insertion quadrupoles were suspected to be the origin of the drifts. The positions of these magnets have been monitored by different systems. The movements are compared to the orbit variations and the correlation is shown. An orbit feedback based on the mechanical measurements has been put into operation to keep the LEP orbit stable.

Contents

1	Introduction	1
2	Orbit impact on accelerator performance	3
2.1	Linear beam dynamics	3
2.2	Closed orbit	9
2.3	Transverse Spin Polarization	11
2.4	Harmonic Spin Matching	16
3	LEP	21
3.1	High energy physics at LEP	21
3.2	The LEP e^+e^- collider	22
3.3	The LEP energy calibration	24
4	Calibration of orbit monitor offsets	29
4.1	Principle of quadrupole strength modulation	29
4.2	Hardware description for k-modulation	31
4.2.1	Modulation of quadrupole strength	31
4.2.2	The Beam Orbit Measurement system	32
4.2.3	Detection of beam oscillations	33
4.2.4	Data acquisition system	34
4.3	Data analysis	35
4.3.1	Harmonic analysis	36
4.3.2	Sampling effects	37
4.3.3	Windowing	39
4.3.4	Cuts	42
4.4	Determination of the orbit monitor offsets	45
4.4.1	The superconducting low-beta insertion quadrupoles	49
4.4.2	Normal conducting magnets with Wide Band BOM	50
4.4.3	Magnets with Narrow Band BOM	51
4.4.4	Impacts of BPM offsets on transverse spin polarization	53
4.5	Beta-function measurement	59

5	Low-beta insertion quadrupole movements	63
5.1	Implications from the beam optics	64
5.2	Hardware for position monitoring	68
5.2.1	Hydrostatic Levelling Systems	69
5.2.2	Differential pressure system	72
5.2.3	Potentiometer based system	72
5.3	Observed movements	73
5.4	Correlation of orbit drifts and quadrupole movements	74
5.4.1	Orbit analysis	74
5.5	Orbit correction system	81
5.6	Corrector Reload	83
6	Conclusions	85
 Appendices		
A	Frequency Analysis	89
A.1	Discrete Harmonic Analysis	89
A.2	Aliasing	90
A.3	Time averaging	92
B	Hydrostatic Levelling System	95
B.1	Database tables	95
B.2	HLS layout	96
B.3	Proportionality factors	98
Bibliography		101
Acknowledgements		106

Chapter 1

Introduction

Particle accelerators have been used since the beginning of this century to investigate the properties of matter and the fundamental interactions between particles. The energy of the colliding particles has been increased in order to study particles with higher masses. The production cross section of heavy particles is often very small. To reach a high rate of interactions, the dimensions of the colliding particle beams have to be kept small at the collision points. High statistics open the possibility for precision measurements of the particle properties. Hence, the predictions of present theoretical models can be verified and differences from the model can lead to new insights and understanding.

The world's largest particle accelerator is currently the electron-positron storage ring LEP* [LEP84] at CERN[†], the European Laboratory for Particle Physics near Geneva, Switzerland, with a circumference of 26.7 km. It has been built to allow precision tests of the *Standard Model* of electroweak and strong interactions [Gla70, Sal68, Wei67]. It was operating until autumn 1995 at energies around 45.6 GeV per beam to produce the neutral vector boson of the weak interaction, the Z-boson. The decays of more than 20 million Z particles have been observed in four experiments: ALEPH, DELPHI, L3 and OPAL. The mass m_Z and decay width Γ_Z have been determined with high precision.

Starting in 1995, LEP has been upgraded in beam energy [LEP96] to permit operation above the W^+W^- pair production threshold in order to study the W-boson, the charged counterpart of the Z. This also extended the mass range for searches of new particles predicted by theory like the Higgs boson or supersymmetric particles.

An accurate alignment of the different accelerator components and a good knowledge of the orbit are prerequisites for obtaining small transverse dimensions of the colliding beams. Specifically the focusing elements, the quadrupoles, have to be aligned with tight tolerances to form a reference system, and the beam has to pass centred through these magnets. Beam position monitors (BPM) are installed at the quadrupole magnets to measure the orbit with respect to this reference. Both careful mechanical alignment and electronical calibration of the monitors can still leave a residual offset between the centres of monitor and magnet. Beam based alignment techniques can further improve the knowledge of the beam position in the quadrupoles. A new technique has been developed at LEP to calibrate the beam position monitors relative to the magnetic centre of the quadrupole magnets.

*Large Electron Positron Collider

[†]Conseil Européen pour la Recherche Nucléaire

Maintaining the optimum performance of a collider also requires a good orbit stability. The orbit can change due to movements of quadrupole magnets, causing larger beam sizes and a lower interaction rate. Past experience at LEP showed that the orbit is slowly drifting away from the optimum position. Frequent orbit corrections were required to compensate this orbit motion. Strong low-beta insertion quadrupoles were suspected to be the source of the drifts, and different systems have been installed to investigate their movements.

In addition to the high interaction rate for a precise determination of the process cross sections, it is important to know the beam energy with a great accuracy to be able to define the energy scale for the colliding particles. Transversal spin polarization opens the possibility to measure the beam energy at LEP with a precision of the order of one MeV.

The spins in an electron-positron storage ring align due to an asymmetry in the probability of spin flips caused by the emission of synchrotron radiation (Sokolov-Ternov-Effect [Sok64]). The spins of the particles precess in the bending field with a frequency directly proportional to their energy. The polarization can be destroyed by applying a radio frequency magnetic field in resonance with the spin precession. The energy can be calculated from the frequency at which depolarization occurs. The method is very accurate because the proportionality constants (the electron rest mass and gyromagnetic anomaly) are known to a high precision.

The energy measurement by resonant depolarization requires a certain degree of polarization. The polarization level is decreased by depolarizing processes which strongly depend on the vertical closed orbit. These depolarizing effects can be significantly reduced for a stable orbit with a good knowledge of the beam position in the quadrupole magnets.

The influence of the depolarizing processes strongly increases with energy and the polarization level above the W production threshold is too small to perform a direct measurement of the energy by resonant depolarization. Measurements at lower energies have to be extrapolated by other methods, and the extrapolation error for the W mass depends on the highest energy where resonant depolarization is possible. Beam based alignment techniques can help to increase the level of polarization, thus allowing a resonant depolarization measurement at a higher energy.

After introducing the required accelerator physics in Chapter 2, the effects of orbit errors are described. Then the basic terms of spin polarization are outlined with an emphasis on the compensation of depolarizing resonances to increase the polarization level. The LEP storage ring is explained in Chapter 3 with a focus on the beam energy determination, where the importance of beam based alignment becomes visible.

Chapter 4 introduces the new technique for beam based alignment, presenting the principle of the method and its installation at LEP in detail. The results of the BPM offset measurements are shown. The influence of the offsets on the achievable polarization level has been studied in simulations. An example to use the installation for a beta function measurement concludes the chapter.

Chapter 5 deals with variations of the vertical orbit of LEP. The orbit analysis and the measurements of magnet movements are shown. The correlation of orbit drifts and quadrupole movements leads to the development of a new feedback system which will be demonstrated.

Chapter 2

Orbit impact on accelerator performance

The performance of a particle accelerator is strongly influenced by the mechanical alignment of the different accelerator components and the resulting orbit of the accelerated particles. To understand this influence, the following chapter introduces some of the concepts of accelerator physics. There are more detailed descriptions available, for example in [San70], [Wie93] or [Wil92].

Particle accelerators can be divided into two classes: linear and circular accelerators. The basic difference is that particles in linear accelerators only traverse the structure once while in circular accelerators they can circulate for many revolutions. This implies that the bunches in a circular accelerator can repeatedly collide and the particles which do not undergo a physical reaction are not lost as the reaction can occur in the next turn.

Alignment errors in linear accelerators only have effects downstream of their location while in circular machines they influence the orbit at every location in the machine.

This chapter will mainly concentrate on circular machines but the differences for linear accelerators will be explained.

2.1 Linear beam dynamics

The guidance of the particles in an accelerator is achieved by electromagnetic fields. The force \vec{F} which acts on the particle of charge e travelling with the velocity \vec{v} is described by Lorentz law

$$\vec{F} = e (\vec{E} + \vec{v} \times \vec{B}) \quad (2.1)$$

where \vec{E} is the electric and \vec{B} the magnetic field. Longitudinal electric fields are used to accelerate the particles while the design path and the transverse focusing is created by transverse magnetic fields.

Any magnetic field transverse to the motion of the particle will bend its trajectory. For a vertical field B_y the instantaneous bending radius ρ for a particle with momentum p travelling in the horizontal plane follows from the equality of centrifugal and Lorentz force

$$\rho = \frac{p}{e B_y}. \quad (2.2)$$

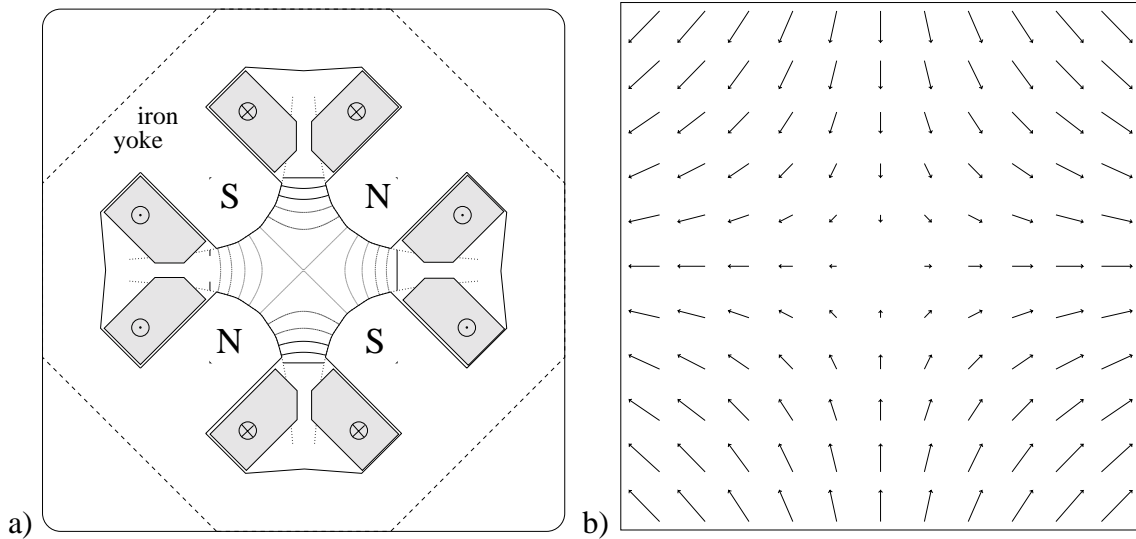


Figure 2.1: a) Transverse cross section of a quadrupole magnet with the magnetic field lines. The pole faces of the magnet have a hyperbolic shape to ensure the linearity of the field. b) Force on a particle traversing a quadrupole magnet. The force rises linearly with the distance from the centre. It is focusing in one plane while it is defocusing in the perpendicular plane.

The most important type of magnets used in an accelerator to create the guiding fields are dipole and quadrupole magnets. Dipole magnets bend the particles onto a closed path in circular accelerators. They have $B_y = \text{const.}$ and the bending of the particles' path is independent from its transverse position inside the magnet.

Quadrupole magnets are used to focus the particle trajectories both in linear and circular accelerators. The magnetic field inside a quadrupole is given by

$$B_x = \frac{\partial B_x}{\partial y} y_Q \quad B_y = \frac{\partial B_y}{\partial x} x_Q \quad (2.3)$$

where $\partial B_x/\partial y$ and $\partial B_y/\partial x$ are the field gradients of the quadrupole and x_Q and y_Q are the distances from its magnetic centre. A particle passing the centre of the quadrupole will not see any magnetic field and will traverse the magnet without deflection. The particle's deflection rises linearly with the distance from its centre (see Fig. 2.1). This property of the quadrupole magnets ensures the focusing of the particles. Particles further away from the centre feel a larger deflection and are more strongly driven back. The focusing is needed to keep the particles in a limited area in the aperture of the accelerator.

From Maxwell's equations it follows that $\partial B_x/\partial y = \partial B_y/\partial x$ and hence quadrupole magnets are focusing in one plane while they are defocusing in the other plane. Consequently, a combination of magnets must be chosen to focus in both planes. The most common structure in accelerator systems is a repetition of short identical units called FODO cells. Each FODO cell is built up of a horizontally focusing (F) quadrupole, a drift space (O), a horizontally defocusing (D) quadrupole and another drift space. This structure is also known as the *alternating gradient* structure [Cou58]. In a circular accelerator, the dipole magnets are placed in between the quadrupoles. They also have an effect on the focusing but it is small compared to the quadrupoles. Higher order multipoles like sextupoles and octupoles are usually included in the FODO cell. Their effect is considered as perturbations of the linear approximation and will not be treated here.

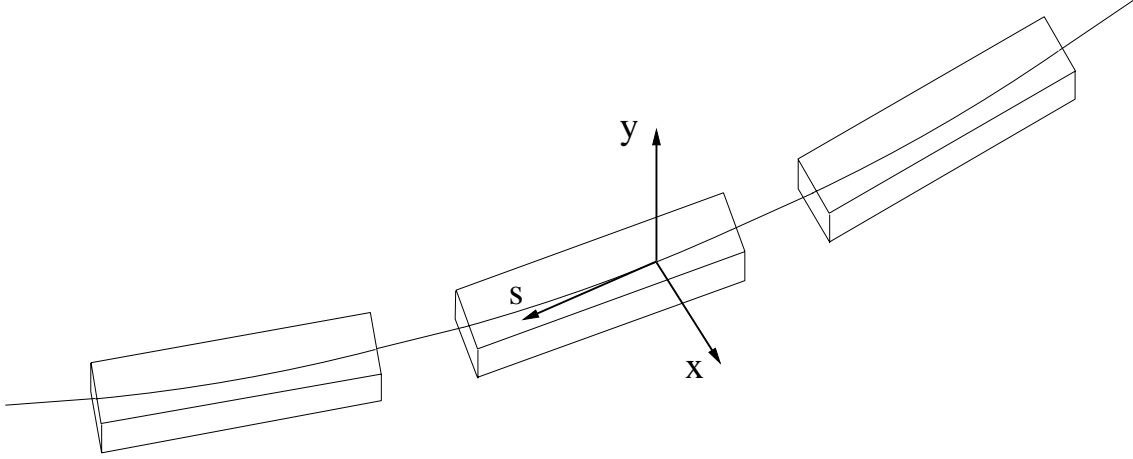


Figure 2.2: Curvilinear coordinate system of the reference orbit

The design path in a circular accelerator is a trajectory that closes after one turn. It is a combination of bending sections in dipole magnets and drift spaces. Quadrupole magnets are interspaced with the dipoles to focus the particles' trajectories. The quadrupoles are arranged such that the design path passes through the centre of the quadrupoles. An ideal particle of design momentum (without emission of synchrotron radiation) would circulate on this reference orbit forever. In the design of most accelerators, there is only a vertical component B_y of the magnetic bending field and the orbit is in a plane with no vertical kicks present.

In a real accelerator, however, field and alignment errors of the magnets and the emission of synchrotron radiation by the particles lead to deviations from this ideal path. A curvilinear coordinate system, as it is shown in Fig. 2.2, is used to describe the motions of a particle with respect to the ideal reference orbit. The longitudinal coordinate s is pointing in the direction of motion of an ideal particle and is the path length from some starting point s_0 . The transversal coordinates are x in the horizontal plane pointing away from the centre of the machine and y in the vertical plane pointing upwards.

The movement of a particle in linear approximation can be described by the following linear differential equations (Hill's equations)

$$\frac{d^2x}{ds^2} + \left(\frac{1}{\rho^2(s)} + k(s) \right) x = \frac{1}{\rho(s)} \frac{\Delta p}{p} \quad (2.4)$$

$$\frac{d^2y}{ds^2} - k(s) y = 0 \quad (2.5)$$

where ρ is the bending radius in the dipole magnets, as in Eq. 2.2, Δp is the deviation from the design momentum p and $k(s)$ is the quadrupole strength defined by

$$k(s) = \frac{e}{p} \frac{\partial B_y}{\partial x}. \quad (2.6)$$

A positive quadrupole strength $k > 0$ implies horizontal focusing while for a horizontally defocusing quadrupole $k < 0$. s is the path length from a starting point s_0 and for a circular accelerator the functions $\rho(s)$ and $k(s)$ are periodic in s with the circumference L of the ring. The differential equations are similar to a harmonic oscillator with a restoring force that varies.

For a particle with design momentum ($\Delta p = 0$) the trivial solution to Eq. 2.4 and Eq. 2.5 is

$$x_0 \equiv 0, \quad y_0 \equiv 0. \quad (2.7)$$

This is the *reference path* or in a circular accelerator the *ideal closed orbit*.

Most of the particles do not travel on this ideal orbit but perform oscillations about it. A general solution which satisfies Eq. 2.4 in the case of $\Delta p = 0$ has the form

$$x_\beta(s) = \sqrt{\varepsilon} \sqrt{\beta(s)} \cos(\mu(s) - \mu_0) \quad (2.8)$$

where $\beta(s)$ shows the same periodicity with L . ε and μ_0 are dependent on the initial conditions. $\beta(s)$ and $\mu(s)$ are linked by the condition

$$\frac{d\mu}{ds} = \frac{1}{\beta}. \quad (2.9)$$

The function $\beta(s)$ is called *betatron function* or *beta function*. It can be seen from Eq. 2.8 that $\beta(s)$ determines together with the constant ε (which is called *emittance*) the maximum amplitude of the transverse oscillation of a particle at a given position of the ring. For an ensemble of particles the beam emittance is defined by the beam size σ and beta function by

$$\sigma(s) = \sqrt{\varepsilon \beta(s)}. \quad (2.10)$$

$\mu(s)$ is called *phase function* and the integral around the ring determines the number of betatron oscillations a particle performs per turn, the *tune* Q of the machine

$$Q_{x,y} := \frac{1}{2\pi} \int_s^{s+L} \frac{dz}{\beta_{x,y}(z)}. \quad (2.11)$$

In general, the particles have a finite spread in energy and $\Delta p \neq 0$. Especially in circular electron accelerators the particles lose energy by the emission of synchrotron radiation and RF cavities at some locations replace the lost energy again. As a consequence, the energy of the particles depends on the position in the ring. A particle with a deviating energy has a different deflection in a magnetic field and will travel on a different trajectory as a particle of design momentum. The solution of Eq. 2.4 can be written in the form

$$x_D(s) = D_x(s) \frac{\Delta p(s)}{p}. \quad (2.12)$$

$D(s)$ is called *dispersion function*. In linear approximation, the trajectory of a particle with an energy deviation can be expressed as a superposition of the dispersion orbit and the free betatron oscillation of a particle of design momentum

$$x(s) = x_\beta(s) + x_D(s). \quad (2.13)$$

In an ideal accelerator without vertical bendings, the vertical dispersion D_y is zero. Misalignment in a real accelerator results in an orbit passing off-centre in quadrupoles and also creates dispersion in the vertical plane but it is generally much smaller than in the horizontal plane.

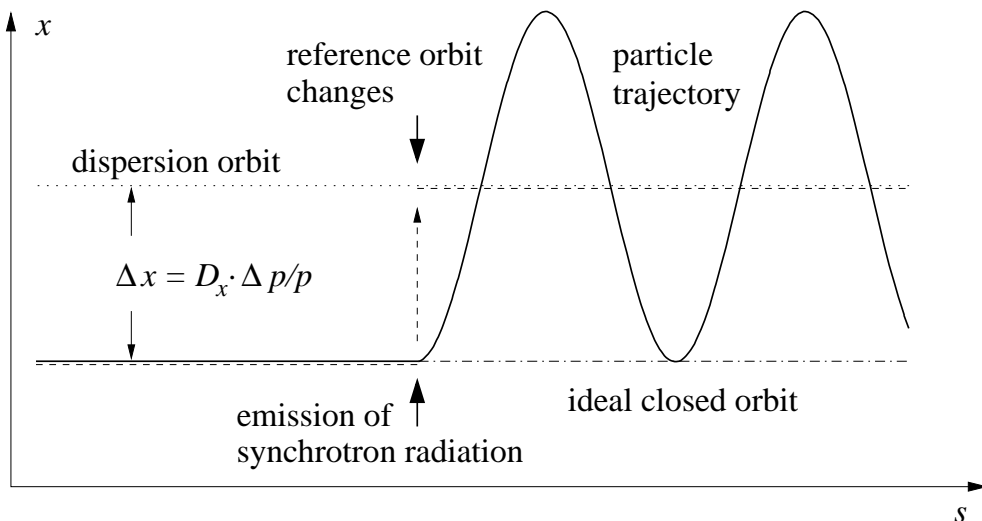


Figure 2.3: A particle of design momentum without betatron oscillation travels on the ideal closed orbit. Due to the emission of a synchrotron radiation photon it loses energy. Its reference orbit changes to the corresponding dispersion orbit for the energy deviation. In a dispersive region, the particle is not on this orbit and it starts to perform betatron oscillations about the new reference orbit.

In an electron machine, the equilibrium emittance is determined by the emission of synchrotron radiation which leads to an excitation of betatron oscillations but is also responsible for damping. A detailed explanation of this process can again be found in [San70, Wie93, Wil92]. Due to the larger dispersion in the horizontal plane this is much more important for the horizontal emittance. The process is depicted in Fig. 2.3. When a particle with design momentum on the ideal closed orbit loses energy by the emission of synchrotron radiation, its reference orbit changes and the new reference is $x_D(s)$ according to Eq. 2.12. If it is in a dispersive region ($D(s) \neq 0$) its physical position is not on this orbit and it starts to oscillate about this new reference orbit. This excitation of betatron oscillations leads to an increase of the emittance.

On the other hand there is some damping caused by the emission of synchrotron radiation. The photons are emitted with a finite angle relative to the trajectory ($\theta \sim 1/\gamma$) and take away some of the transverse momentum. Since the acceleration by the RF cavities is only longitudinal, the oscillations are damped. The equilibrium emittance results from the interplay of the two processes.

The emittance has an immediate effect on the *luminosity* of a particle collider. The luminosity \mathcal{L} relates the event rate \dot{N} of a given process to its reaction cross section σ by

$$\dot{N} = \frac{dN}{dt} = \mathcal{L} \cdot \sigma. \quad (2.14)$$

The luminosity can be expressed in terms of the number of particles N_1 and N_2 of the counter-rotating bunches, the number of bunches per beam k_b , the revolution frequency f_{rev} and the beam sizes σ_x^* and σ_y^* at the collision point

$$\mathcal{L} = \frac{k_b f_{\text{rev}} N_1 N_2}{4\pi \sigma_x^* \sigma_y^*}. \quad (2.15)$$

The beam size at the collision point depends on the emittance as $\sigma^* = \sqrt{\varepsilon \beta^*}$ with β^* the beta function there. The emittances have to be kept as small as possible to maximise the luminosity.

The horizontal emittance in a circular accelerator is always finite due to the dispersion created by the bending magnets. The vertical dispersion in an ideal accelerator without vertical bending is zero and would lead to a vanishing emittance. But the recoil of the synchrotron radiation photons emitted with a finite opening angle excites betatron oscillations. This sets the lower limit for the vertical emittance. It can be approximated by [Wie93]

$$\varepsilon_y = \frac{C_q \bar{\beta}_y \langle 1/\rho^3 \rangle}{2J_y \langle 1/\rho^2 \rangle} \quad C_q = \frac{55}{32\sqrt{3}} \frac{\hbar}{m_0 c} \quad (2.16)$$

with $\bar{\beta}_y$ the average beta function, $J_y \approx 1$ and ρ the bending radius. Since $C_q = 3.84 \cdot 10^{-13}$ m, this fundamental lower limit is also of the order of 10^{-13} m. It is much smaller than the achievable emittance in a real accelerator which is determined by the misalignment of the magnets. Every vertical bending by misaligned quadrupoles and corrector magnets creates vertical dispersion which increases the vertical emittance. In addition, the horizontal betatron oscillations are coupled into the vertical plane by tilted magnets and by particles passing off-centre through sextupole magnets. The vertical emittance caused by these effects in real machines is usually of the order of a percent of the horizontal one.

Consequently, the misalignments and steering errors in the vertical plane have to be kept as small as possible to obtain a small vertical beam emittance. The resulting small vertical beam size leads to a high luminosity.

The particles do not only perform oscillations in the transverse plane but also in the longitudinal direction and in their energy. The energy changes are provoked by the emission of synchrotron radiation when the particle's path is bent. The radiated power P_{rad} for a particle with the energy $E = \gamma m_0 c^2$ on a trajectory with the bending radius ρ is [Iva48]

$$P_{\text{rad}} = \frac{1}{6\pi} \frac{ce^2}{\varepsilon_0} \frac{\gamma^4}{\rho^2} \quad (2.17)$$

where c is the velocity of light and ε_0 is the absolute permittivity of free space.

The energy loss ΔE_{rad} of a particle per turn is obtained by integration over the circumference L of the ring and can be approximated for identical bending around the ring to

$$\Delta E_{\text{rad}} = \oint P_{\text{rad}} ds = \frac{1}{3} \frac{ce^2}{\varepsilon_0} \frac{\gamma^4}{\rho}. \quad (2.18)$$

Since the energy loss scales with the fourth power of the energy, it rapidly increases for higher energies. While the loss per turn at LEP for a particle of 45.6 GeV is 120 MeV, it is 2 GeV at 92 GeV.

The lost energy is replenished by radio-frequency cavities which operate at a multiple of the revolution frequency. The energy gain must be sufficient to compensate the losses and limits the highest operating energy of a circular accelerator. The equilibrium of energy losses and acceleration results in a stable oscillation in energy and longitudinal position. The frequency of this oscillation is called synchrotron tune Q_s and represents the number of synchrotron oscillations per revolution.

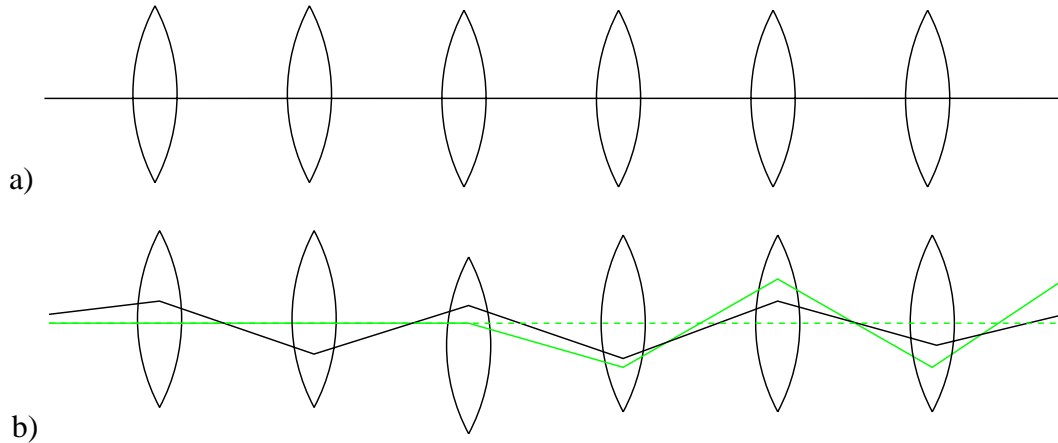


Figure 2.4: a) The closed orbit in an ideal accelerator passes through the centres of the quadrupole magnets (indicated by lenses) b) An additional kick in the orbit distorts the orbit downstream of the error source in a linear accelerator and changes the closed orbit all around a circular accelerator.

The ensemble of particles has a certain relative spread σ_ε/E in energy which is given by

$$\frac{\sigma_\varepsilon}{E} = \gamma \sqrt{\frac{C_q}{2\rho}} \quad (2.19)$$

which is proportional to the energy.

2.2 Closed orbit

In general, the tune Q in a circular accelerator is not an integer (this leads to resonances, which will be shown later) and the trajectories of the oscillating particles do not close after one turn. There is only one unique periodic path existing where the particle returns to the identical position after one revolution with*

$$y_{\text{co}}(s) = y_{\text{co}}(s + L). \quad (2.20)$$

For an ideal accelerator this path is the trivial solution of Hill's equation, $y_{\text{co}} \equiv 0$. This ideal closed orbit is the design path which passes through the centres of the quadrupole magnets (Fig 2.4 a).

Any field errors, misalignment or tilt of the magnet will create an additional deflection in the orbit and the trivial solution is not a physical path any more. For a linear accelerator this will only alter the orbit downstream of the error source. In a circular accelerator the particles will pass the same error source in the next turn again. Finally, the orbit will move to a new stable equilibrium position (Fig 2.4 b). The new *distorted closed orbit* is nothing other than a closed betatron oscillation around the undistorted ideal closed orbit which has an additional angular kick at the position of the error source (Fig 2.5). Particles which are not on this distorted closed orbit will now perform betatron oscillations about it as a reference.

*The equations given for the vertical plane in this section are analogous for the horizontal plane.

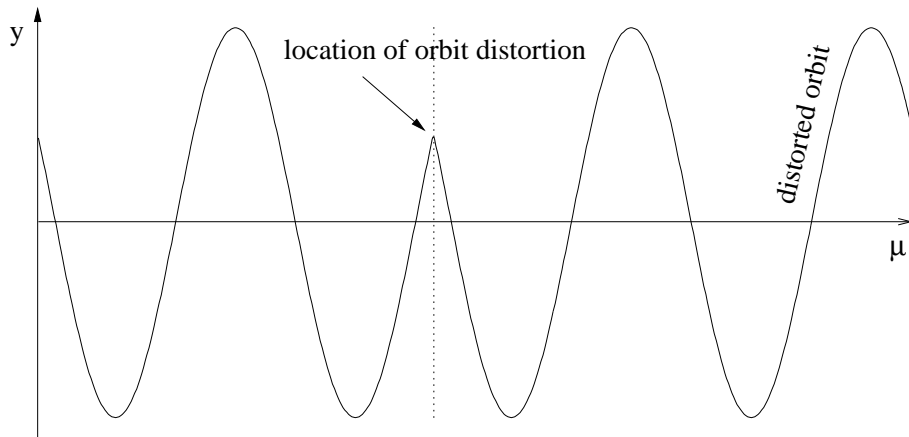


Figure 2.5: A dipole error at one location s_0 causes the closed orbit in a circular accelerator to change. The new solution is a closed betatron oscillation with an additional deflection at the location of the error.

The additional orbit kick can have several reasons. It can be

- a field error in a dipole magnet
- a gradient error in a quadrupole for a particle passing off-centre
- a misalignment of a quadrupole
- a tilted magnet
- an orbit correction magnet.

For a misaligned quadrupole with a misalignment of Δy at the location s_0 the angular orbit kick $\Delta y'$ is

$$\Delta y'(s_0) = k \cdot l \cdot \Delta y \quad (2.21)$$

with k the quadrupole strength and l the magnetic length of the magnet. This is an additional dipole kick in the orbit which is independent of the particle's position inside the magnet.

For a gradient change Δk in a quadrupole at the location s_0 the angular kick is

$$\Delta y'(s_0) = \Delta k \cdot l \cdot y_Q(s_0) \quad (2.22)$$

where $y_Q(s_0)$ is the beam position relative to the magnetic centre of the quadrupole. In this case, the angular kick is proportional to the distance from the centre of the magnet.

Any additional kick at a position s_0 changes the closed orbit at any location s of the circular accelerator by $\Delta y(s)$ according to

$$\Delta y(s) = \frac{\sqrt{\beta(s_0) \cdot \beta(s)} \cos(|\mu(s) - \mu(s_0)| - \pi Q)}{2 \sin(\pi Q)} \cdot \Delta y'(s_0) \quad (2.23)$$

where β , μ and Q are respectively the betatron function, phase advance and tune in the plane of motion under consideration. The local orbit error changes the orbit all around the ring. The amplitude of the displacement changes with the square root of the betatron function and is modulated by the phase advance to the error source. It only vanishes where the cosine term becomes zero.

This formula shows that a tune Q which is integer or close to it has to be avoided. The denominator becomes large and any small kick leads to large orbit distortions. A particle would come to the location of the distortion with a similar phase and the kicks coherently add up. The amplitude of the oscillation grows and the particle is eventually lost.

Higher multipole errors such as quadrupole, sextupole errors in the beam optics lead to similar expressions for the orbit distortions with $\sin(n\pi Q)$ ($n \in \mathbb{N}$) in the denominator. This causes half-, third-integer and higher order resonances for the tunes which have to be avoided.

The magnet errors not only cause the orbit to change, but also changes in other machine parameters like beta function and tunes. The tune shift ΔQ due to a small change Δk in the strength of a quadrupole of length L at location s_0 is given by

$$\Delta Q = -\frac{1}{4\pi} \int_{s_0}^{s_0+L} \beta(s) \Delta k \, ds \simeq -\frac{\beta_Q \Delta k L}{4\pi} \quad (2.24)$$

with β_Q the average beta function in the quadrupole. Observing the tune change permits the calculation of the average beta function in a quadrupole magnet when the gradient is changed by a known Δk .

Small dipole correction magnets are used to compensate the effect of the errors and to steer the orbit close to the design path. Most accelerators have less correction magnets per plane than quadrupole magnets. This implies that the effect of the misalignment cannot be completely compensated but only minimised. The orbit kicks in quadrupole and corrector magnets create dispersion which increases the emittance, particularly in the vertical plane. Consequently, the vertical emittance and hence the luminosity depend on the vertical closed orbit.

The aim of the orbit correction is to minimise orbit excursions and dispersion. An apparent flat orbit can still cause dispersion through the misalignments. So the orbit is usually corrected to a reference orbit which gives small beam sizes and high luminosity. This reference, often called *Golden Orbit*, does not necessarily have the smallest orbit excursions and is found empirically during operation of a machine. The details for the good performance of the golden orbit are not yet understood. It is assumed that this orbit gives the optimum vertical emittance ε_y due to a favourable distribution of the vertical dispersion D_y .

2.3 Transverse Spin Polarization

The preceding sections were describing the influence of the magnetic fields on the trajectory of the particles. The following section will lay out the effects of the magnetic fields on the magnetic moment. This part is only intended to explain the main phenomena. An extensive description can be found in [Mon84].

The magnetic moment $\vec{\mu}$ is related to the spin \vec{S} of the particles by

$$\vec{\mu} = g \frac{e}{2m_e} \vec{S} \quad (2.25)$$

with g the gyromagnetic ratio (Landé-factor), e the elementary charge and m_e the electron mass. The magnetic moment is parallel to the spin for positrons and anti-parallel for electrons.

The ensemble polarization vector \vec{P} for N particles is defined as the classical normalised centre of mass of the spin vectors \vec{S}_i as

$$\vec{P} = \frac{1}{N} \sum_{i=1}^N \vec{S}_i. \quad (2.26)$$

The absolute value of the polarization vector is the degree of polarization P . This corresponds to the stochastic definition

$$P = \frac{N_{\uparrow\downarrow} - N_{\uparrow\uparrow}}{N_{\uparrow\downarrow} + N_{\uparrow\uparrow}} \quad (2.27)$$

where $N_{\uparrow\uparrow}$ and $N_{\uparrow\downarrow}$ are the number of electron spins parallel and anti-parallel to the direction of the magnetic field, respectively.

Electrons and positrons circulating in a storage ring tend to polarize their spins transversely to their direction of motion due to the emission of spin-flip synchrotron radiation (Sokolov-Ternov-Effect, [Sok64]). Positrons are polarized parallel to the main bending field and electrons anti-parallel. Only a small fraction of the synchrotron radiation causes a spin-flip. The ratio to non spin-flip synchrotron radiation is

$$\frac{W_{\text{spin-flip}}}{W_{\text{nospin-flip}}} = 3 \left(\frac{\hbar\gamma^2}{m_e c \rho} \right)^2 \cdot \left(1 \pm \frac{35\sqrt{3}}{64} \right) \quad (2.28)$$

where the sign in the bracket depends on the initial spin orientation to the magnetic field. For LEP at 45 GeV ($\gamma \sim 8.8 \cdot 10^4$, $\rho \sim 3000$ m) this is of the order of 10^{-12} . The build-up of polarization is hence a very slow process compared to other phenomena in a storage ring.

For initially unpolarized electrons or positrons in an ideal ring, the polarization level changes according to

$$P_{\tau_{\text{ST}}}(t) = P_{\text{ST}} \left(1 - \exp \left(-\frac{t}{\tau_{\text{ST}}} \right) \right) \quad (2.29)$$

with the asymptotic polarization of

$$P_{\text{ST}} = \frac{8}{5\sqrt{3}} = 0.9238 \quad (2.30)$$

and a characteristic build-up time

$$\tau_{\text{ST}} = \left(\frac{5\sqrt{3}r_e\hbar}{8m_e} \right)^{-1} \cdot \left(\frac{\gamma^5}{|\rho|^3} \right)^{-1}. \quad (2.31)$$

The build-up time τ_{ST} at LEP for energies around 45 GeV is of the order of five to six hours.

Inside a magnetic field \vec{B} , the spin precesses about the direction of the field. The Thomas-Bargmann-Michel-Telegdi (T-BMT) equation [Tho27, Bar59] describes the motion in an electro-magnetic field

$$\frac{d\vec{S}}{ds} = \vec{\Omega}_l \times \vec{S} \quad (2.32)$$

where $\vec{\Omega}_l(\vec{B}, \vec{E}, \gamma)$ is a function of fields and energy and s is the longitudinal coordinate. In the case of an ultra-relativistic electron ($\gamma \gg 1$) in a magnetic field[†]

$$\vec{\Omega}_l = \frac{e}{cm_e\gamma} \left((1+a)\vec{B}_{\parallel} + (1+a\gamma)\vec{B}_{\perp} \right) \quad (2.33)$$

where \vec{B}_{\parallel} and \vec{B}_{\perp} are the magnetic fields parallel and perpendicular to the trajectory, respectively, and $a = (g-2)/2$ is the gyromagnetic anomaly ($a = 0.001159652193(10)$). For an ideal accelerator with $\vec{B}_{\perp} \parallel \hat{e}_y$ and vanishing \vec{B}_{\parallel} , this transforms to

$$\vec{\Omega} = \frac{e\vec{B}_{\perp}}{cm_e\gamma} \cdot a\gamma \quad (2.34)$$

in a frame moving with the particle. The first expression is the relativistic cyclotron frequency ω_c and $a\gamma$ is called *spin tune* ν . The spin of the particle performs ν revolutions around the bending field axis for one revolution around the ring. The number of spin revolutions is proportional to the energy E with the relation

$$\nu = \frac{a}{m_e c^2} \cdot E = \frac{E [\text{MeV}]}{440.6486(1)}. \quad (2.35)$$

This relation is the basis for a very precise energy measurement at LEP (see Section 3.3) since the gyromagnetic anomaly a and the electron rest mass m_e are known to very high accuracy.

The spin motion has to be generalised for a real storage ring in the presence of magnetic fields which are not vertical ($\vec{B}_{\perp} \nparallel \hat{e}_y$). It can be achieved by integration of the T-BMT equation on the periodic closed orbit. This leads to the periodic spin vector \vec{n}_0 which is defined as the periodic solution of Eq. 2.32 on the closed orbit with $\vec{n}_0(s+L) = \vec{n}_0(s)$ [Der70]. The \vec{n}_0 -axis plays the same role for the spin motion as does the closed orbit for the orbital motion. The spin vectors of the individual particles precess around \vec{n}_0 . The spin tune ν is the number of spin precessions for one revolution on the closed orbit. In a perfect planar machine, the vector \vec{n}_0 would be always parallel to the main bending field.

The build-up of polarization is still in the direction of the main bending field but only the component along \vec{n}_0 can persist. The value of the asymptotic polarization now depends on the projection of \vec{n}_0 onto the bending field direction $\hat{b} = \vec{v} \times \vec{v}' / |\vec{v} \times \vec{v}'|$ as

$$P_{\infty} = P_{\text{ST}} \frac{\oint \frac{ds}{|\rho(s)|^3} (\vec{n}_0 \cdot \hat{b})}{\oint \frac{ds}{|\rho(s)|^3} \left[1 - \frac{2}{9} (\vec{n}_0 \cdot \hat{v})^2 \right]} \quad (2.36)$$

with a build-up time τ_p

$$\frac{1}{\tau_p} = \frac{5\sqrt{3} r_e \hbar \gamma^5}{8m_e L} \oint \frac{ds}{|\rho(s)|^3} \left[1 - \frac{2}{9} (\vec{n}_0 \cdot \hat{v})^2 \right]. \quad (2.37)$$

[†]The effect of electric fields is much smaller and can usually be neglected. A magnetic field of 1 T corresponds to an electric field of $3 \cdot 10^8$ V/m.

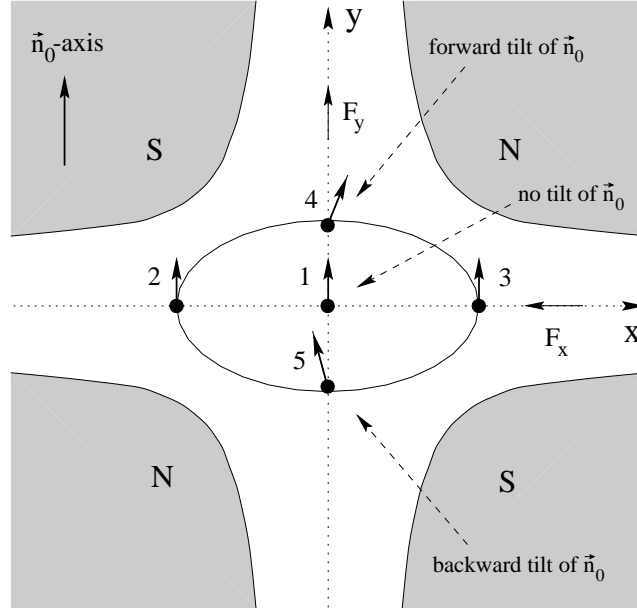


Figure 2.6: Additional tilts of a particle passing a quadrupole magnet at a location where $\vec{\eta}_0 \parallel \hat{e}_y$. Particles passing vertically centred (1,2,3) do not get an additional tilt with respect to the $\vec{\eta}_0$ -axis. For particles off-centre (4,5) the direction of their spin vector changes. If $\vec{\eta}_0$ is not vertical the spin vector gets a tilt even on the horizontal axis.

The direction of the asymptotic polarization is now the direction of $\vec{n}_0(s)$. This is the direction of a stable polarization in a storage ring.

It is obvious from Eq. 2.36 that a maximum polarization is obtained when \vec{n}_0 is parallel to \vec{B} . Any horizontal field will tilt \vec{n}_0 from the vertical direction and decrease the polarization. This implies that the closed orbit passing vertically off-centre in a quadrupole magnet will cause a tilt of the \vec{n}_0 -axis (see Fig. 2.6).

The same effect in combination with synchrotron radiation leads to a diffusion of the spins away from the direction of the \vec{n}_0 -axis [Bai66]. The particles change their energy due to the photon emission and perform longitudinal and transverse oscillations (see Section 2.1). Due to the stochastic nature, the particles of the ensemble will pass the quadrupoles at different locations and the individual spins \vec{S}_i will undergo different tilts. The oscillations are damped and the orbital motion disappears but the spins remain tilted away from \vec{n}_0 . Hence the average projection onto the \vec{n}_0 -axis is reduced which decreases the polarization value. The reduction is strongest when the spin motion is in resonance with the orbital motion which means the condition

$$\nu = k + k_x Q_x + k_y Q_y + k_s Q_s \quad (2.38)$$

is fulfilled with k, k_x, k_y, k_s being integer.

The diffusion process leads to a decrease of the achievable polarization level. Eq. 2.36 can be rewritten in the approximate form

$$P_{\text{eff}} = \frac{P_{\infty}}{1 + (\tau_p/\tau_d)} \quad (2.39)$$

where the polarization time τ_p is defined as in Eq. 2.37 and the depolarization time τ_d as

$$\frac{1}{\tau_d} = \frac{55r_e\hbar\gamma^5}{48\sqrt{3}m_eL} \oint \frac{ds}{|\rho(s)|^3} |\vec{d}(s)|^2. \quad (2.40)$$

The *spin-orbit coupling vector* $\vec{d}(s)$ describes the effect of quantum emission at a location s on the spin. In linear approximation it is given as the change in the orientation of \vec{n}_0 after damping of the orbital oscillations caused by photon emission with a relative energy change $\partial\gamma/\gamma$.

$$\vec{d}(s) = \gamma \frac{\partial \vec{n}_0(s)}{\partial \gamma}. \quad (2.41)$$

It is perpendicular to \vec{n}_0 and is entirely determined by the lattice of the storage ring only depending on the position where the photon is emitted.

The build-up of the polarization is still exponential

$$P_{\tau_{\text{eff}}}(t) = P_{\text{eff}} \left(1 - \exp\left(-\frac{t}{\tau_{\text{eff}}}\right) \right) \quad (2.42)$$

with the effective build-up time

$$\tau_{\text{eff}} = \frac{\tau_p \tau_d}{\tau_p + \tau_d}. \quad (2.43)$$

When the characteristic depolarization time τ_d is significantly smaller than τ_p , the maximum polarization level in Eq. 2.39 is drastically reduced. The depolarizing effects have to be well controlled to achieve a high degree of polarization.

The depolarizing effects become more important at higher energy. The magnetic field of the accelerator's magnets is proportionally scaled to energy to keep the angular deflection θ constant. So the effect from misalignment on orbit errors remains constant. The situation for the spin motion is different. Every orbit kick $\Delta y'$ perturbs the spin motion by a movement of the spin vector of $|\Delta \vec{\gamma}| = a\gamma \cdot \Delta y'$. Therefore the spin kicks scale with energy. With increasing beam energy, the spin motion becomes more sensitive to magnet misalignments. The beam polarization becomes more vulnerable to the depolarization resonances.

Not only does the influence of the integer resonances become stronger, but also the higher order spin resonances ($\sum |k_i| > 1$ in Eq. 2.38) become more and more important at higher energies. The strength of these resonances can be calculated in a formalism introduced by J. Buon [Buo89], S. Mane [Man90] and K. Yokoya [Yok83]. The strength of the higher order sidebands is quantified by the *tune modulation index* λ

$$\lambda^2 = \left(\frac{a\gamma \sigma_\varepsilon}{Q_s E} \right)^2. \quad (2.44)$$

The strength of the sidebands depends on the integer resonance strength and powers of λ^2 , i.e. the n^{th} order sideband enters with a factor λ^{2n} . Since the relative energy spread σ_ε/E is proportional to the energy (see Eq. 2.19), the tune modulation index varies with the fourth power of γ .

2.4 Harmonic Spin Matching

Not all orbit deviations lead to a strong decrease of the polarization value. Only a coherent summation of distortions causes a strong depolarization. The depolarization through deviation of the \vec{n}_0 -axis from the vertical is driven by Fourier components of the vertical closed orbit. This is clear from the fact that horizontal fields are only present in excited vertical corrector magnets and for a particle passing vertically off-centre in quadrupole magnets. The magnetic field B_x is proportional to the distance y_Q from the centre of the quadrupole.

Derbenev and Kondratenko [Der79] demonstrated that the contribution of the (complex) Fourier components c_k of the vertical closed orbit influence the depolarization by the \vec{n}_0 -axis tilt as

$$\frac{\tau_p}{\tau_d} \propto \nu^2 \sum_k \frac{|c_k|^2}{(\nu - k)^4}. \quad (2.45)$$

The derivation assumes that synchrotron oscillations are the dominating depolarization process neglecting betatron oscillations. This is a good approximation for plane storage rings at high energies close to half integer spin tunes. The resulting degree of polarization can be calculated from Eq. 2.39. When the spin tune ν is chosen close to a half integer ($\nu = k_0 + 0.5$, $k_0 \in \mathbb{N}$), only the closest Fourier components c_{k_0} and c_{k_0+1} have a strong influence on the depolarization. Due to the $(\nu - k)^4$ term, the effect of the next closest components is nearly two orders of magnitude less.

A special orbit correction scheme allows the reduction of the closest Fourier components and the deviation of the \vec{n}_0 -vector which increases the degree of polarization. This spin resonance compensation is known as *Harmonic Spin Matching* (HSM). The Harmonic Spin Matching minimises the integer spin resonances ($\sum |k_i| = 0$ in Eq. 2.38) which depend on the \vec{n}_0 -axis tilt. The higher order spin resonances which are proportional to the integer resonances are weakened accordingly.

A set of closed vertical orbit bumps can be generated which change a particular harmonic each [Sch82, Ros85]. A symmetry imposed in the bumps assures that nearby components are not affected. A set of four different bumps is sufficient to compensate the closest Fourier components. The effect from the bumps on the orbital motion of the particles is small.

Basically, the Fourier components c_k can be computed from the vertical closed orbit measurement (*Deterministic HSM*) [Ass94a, Ass94b]. The complex c_k are derived from the cosine (a_k) and sine (b_k) components of the vertical orbit measurements y_i in the spin precession frame. The bending angle α in the bending magnets is used for the analysis since it is proportional to the spin precession. A discrete Fourier transform of the set of N orbit measurements y_i is performed

$$a_k = \frac{1}{\pi} \sum_{i=1}^N y_i \cos(k\alpha_i) \delta\alpha_i \quad (2.46)$$

$$b_k = \frac{1}{\pi} \sum_{i=1}^N y_i \sin(k\alpha_i) \delta\alpha_i \quad (2.47)$$

$$c_k = \sqrt{a_k^2 + b_k^2} \quad (2.48)$$

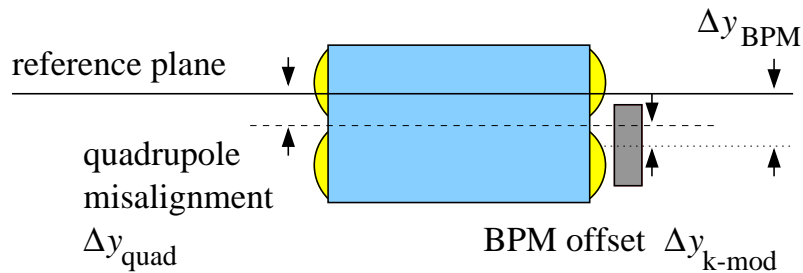


Figure 2.7: Different positioning errors influence the calculation of the orbit harmonics. The read error Δy_{BPM} of the BPM relative to the ideal plane orbit can be expressed as the sum of the offset $\Delta y_{k\text{-mod}}$ to the quadrupole and the quadrupole misalignment Δy_{quad} .

where k is the harmonic number of the Fourier component, α_i the integrated bending angle and $\delta\alpha_i = (\alpha_{i+1} - \alpha_{i-1})/2$ is the bending around the location of the orbit measurement.

The calculation is based on the vertical closed orbit positions relative to an ideal plane. In practice, the success of this method crucially relies on the precision of the orbit measurements y_i . Both an offset $\Delta y_{k\text{-mod}}$ of the beam position monitors with respect to the magnetic centre of the quadrupoles and the misalignment Δy_{quad} of the quadrupole magnets lead to an error Δy_{BPM} of the BPM with respect to the ideal closed orbit in a plane (see Fig. 2.7). This has implications for LEP which will be explained in Section 3.3 and the dependencies will be studied in more detail in Section 4.4.4.

If the calculation of the coefficients from the vertical orbit is not possible or too limited in precision one can vary the amplitude of the compensation bumps and observe the changes in the polarization level. This method is known as *Empirical HSM*.

It is very time consuming to perform an optimisation by empirical HSM when the build-up time of polarization is slow. The parameter space of the Fourier components has to be scanned by variation of orbit bumps. The variation of the polarization level is slow due to the large build-up time. Furthermore, the change of polarization has to be above the statistical fluctuations of the polarimeter to be observable. This becomes impossible if the initial degree of polarization is too low.

For a spin tune close to half-integer ($\nu \approx i+0.5, i \in \mathbb{N}$), the level of polarization P can be expressed from Eq. 2.45 in the approximation that only the closest Fourier harmonics equally contribute as

$$P = \frac{P_{\text{max}}}{1 + d \cdot (a_i^2 + b_i^2 + a_{i+1}^2 + b_{i+1}^2)} \quad (2.49)$$

where P_{max} is the maximum achievable polarization at the particular machine settings (energy, tunes, etc.) for perfect harmonic correction. a_k and b_k are the Fourier components of the orbit from Eq. 2.46 and Eq. 2.47. The constant d can be calculated by a fit from the simulations for different strengths of the harmonics. An example is shown in Fig. 2.8.

Since the parameter space of the significant Fourier components is four-dimensional the empirical HSM can be problematic. To illustrate this difficulty, the dependence of the polarization level on the two adjacent harmonics $c_i = (a_i^2 + b_i^2)^{1/2}$ and c_{i+1} is drawn in Fig. 2.9. If one harmonic (c_i in the figure) is relatively well compensated, a variation of the other leads to a significant change in polarization. This change is only minor – and possibly not experimentally observable – when the compensation is not good and the harmonic is still large. One has to keep in mind that each c_i depends again on two

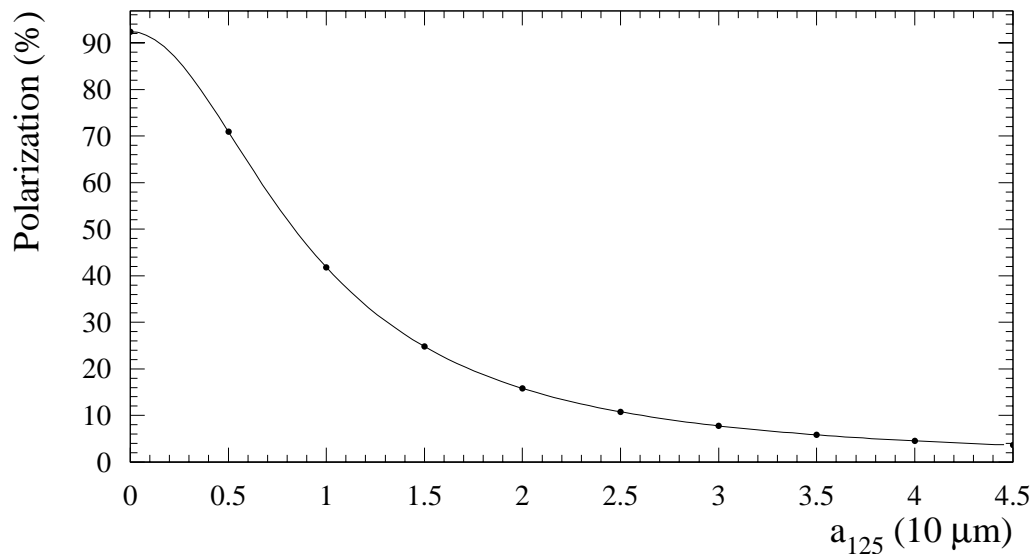


Figure 2.8: Dependence of the polarization level on the strength of the adjacent harmonic q . The results are from SITF calculations for an ideal LEP machine at a spin tune of $\nu = 125.5$ for varying amplitude of the harmonic bump. The fitted function has the form of Eq. 2.49.

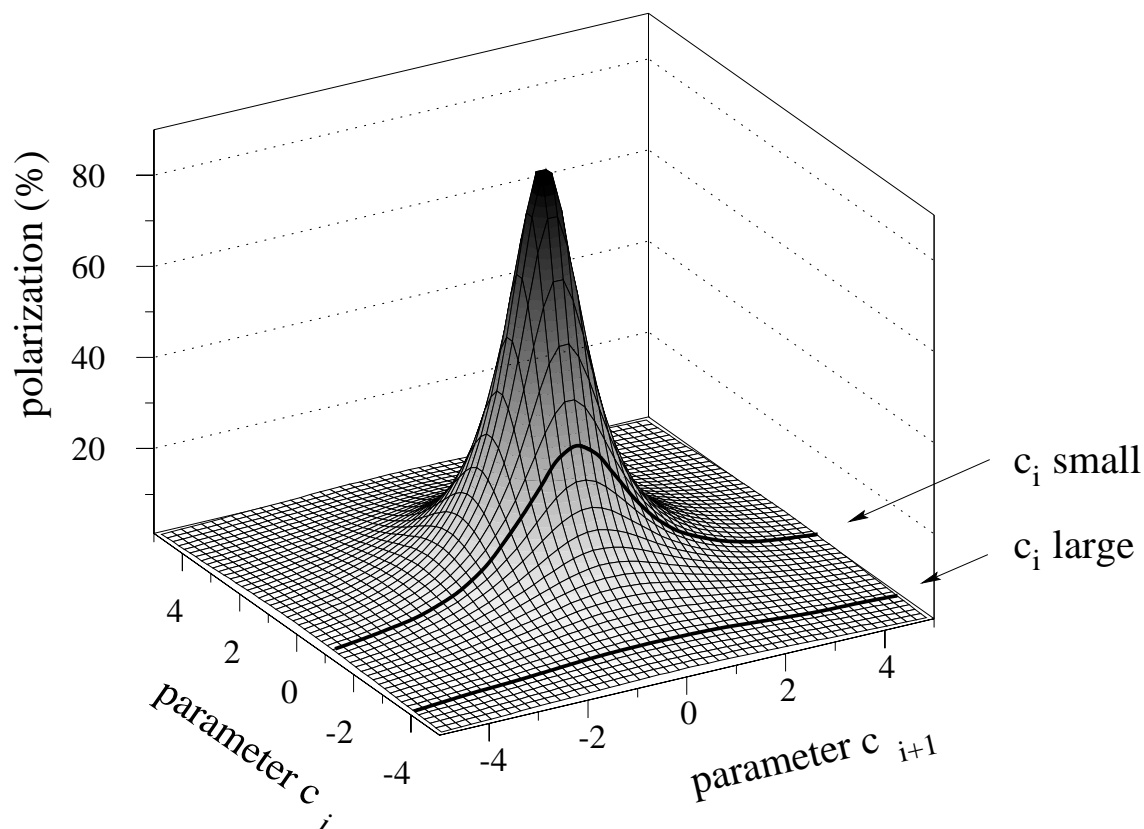


Figure 2.9: Dependence (in the linear model) of the polarization level on the strength of the adjacent depolarizing resonances c_i and c_{i+1} . The bold lines indicate the variation of the polarization degree with c_{i+1} for relatively well corrected c_i in one case and a worse correction in the other.

parameters. A figurative view of this is to imagine a similar figure with the dependence of the remaining two parameters at any point of the surface of Fig. 2.9.

The dependence on one harmonics parameter keeping the others constant is seen by rearranging Eq. 2.49 (in the case of varying b_{i+1}) to

$$\begin{aligned}
 P &= \frac{P_{\max}}{1 + d(a_i^2 + b_i^2 + a_{i+1}^2) + d \cdot b_{i+1}^2} = \frac{\frac{P_{\max}}{1 + d(a_i^2 + b_i^2 + a_{i+1}^2)}}{1 + \underbrace{\frac{d}{1 + d(a_i^2 + b_i^2 + a_{i+1}^2)}}_{d'} \cdot b_{i+1}^2} \\
 &= \frac{P'_{\max}}{1 + d' \cdot b_{i+1}^2} \tag{2.50}
 \end{aligned}$$

which shows the same functionality but with a lower maximum degree of polarization $P'_{\max} = P_{\max}/[1 + d(a_i^2 + b_i^2 + a_{i+1}^2)]$ and a weaker dependence d' on the particular harmonic. This shows that empirical HSM can be practically impossible if the initial harmonics are too large. It also makes it obvious that the variation of one component has the biggest impact on polarization if the other harmonics are already well corrected.

Therefore, the deterministic HSM must provide already a relative accurate prediction of the strength of the Fourier harmonics a_k and b_k . Only then, the empirical variation of the harmonics will lead to detectable changes in the polarization level, in particular at higher energies where the maximum level is small. So the determination of the BPM offsets $\Delta y_{k\text{-mod}}$ is important for a successful optimisation of the polarization.

Chapter 3

LEP

3.1 High energy physics at LEP

The LEP collider was built to probe the *standard model* of strong and electroweak interactions [Gla70, Wei67, Sal68]. Since its development, the model has been a successful theory to describe three of the four fundamental forces. All present experimental data are consistent with this theory, however our understanding of the standard model is far from complete. Precise measurements of its parameters and experiments at higher energies are required to gain further insights and to probe theories beyond the standard model.

One of the main aims at LEP was the precise measurement of the mass and the decay width of the Z particle, the neutral carrier of the weak force. The dominant process for the study is

$$e^+e^- \longrightarrow Z^0 \longrightarrow f\bar{f}$$

where the production of a Z is followed by decay into various channels of fermion-antifermion pairs. The annihilation cross section for decay into hadrons is shown in Fig. 3.1. The Z resonance leads to a strong increase in the cross section around $m_Zc^2 = 91.2$ GeV. The mass and decay width of the Z can be determined from cross section measurements. The precision of the mass and width determination critically depends on the accurate measurement of the beam energy which is explained in Section 3.3. The exact shape around the Z resonance demonstrated that only three families of light neutrinos exist [LEP95].

Measurements around the Z peak particularly profited from the very large statistics available for a well-defined initial state. The results are also sensitive to particles with masses beyond the direct production which enter via radiative corrections. Predictions can be made for masses of heavier particles like the top quark and the Higgs boson.

For direct searches of new physics at higher energy, nevertheless, the beam energy of LEP had to be increased. A detailed report on the physics prospects of this LEP II project can be found in [Alt96]. One major goal is the precise determination of the mass of the W boson [Kun96], the charged partner of the Z, to improve the present best measurements from the Tevatron.

When LEP is operated at centre of mass energies above $2m_Wc^2 = 2 \cdot 80.3$ GeV W particles are produced in pairs in the reaction

$$e^+e^- \longrightarrow W^+W^- \longrightarrow 4f$$

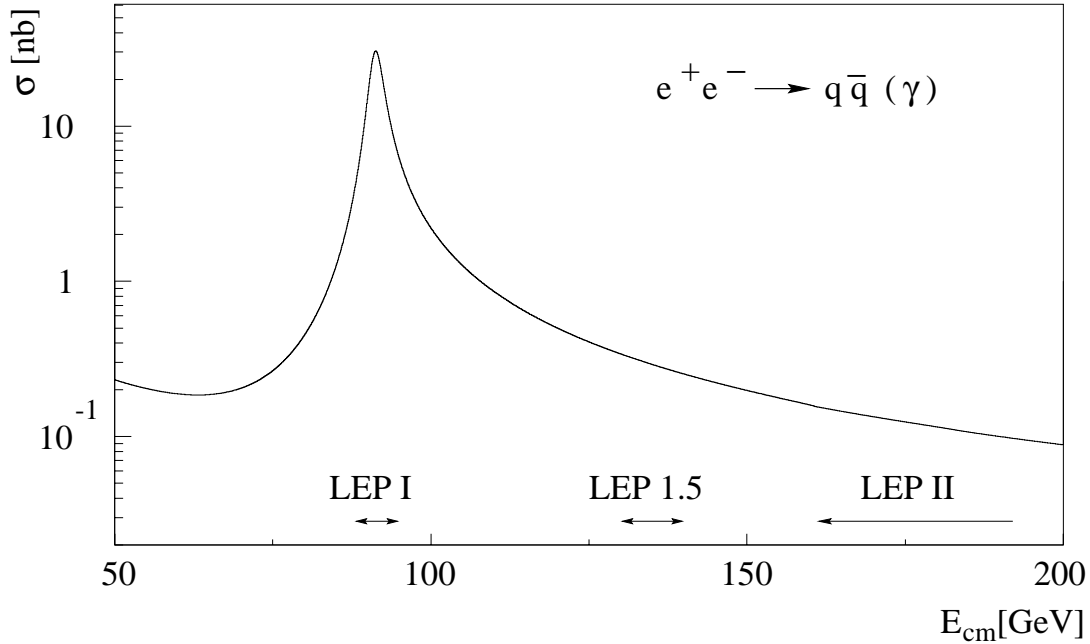


Figure 3.1: Hadronic cross section (Initial State Radiation included) as a function of the centre of mass energy.

with a following decay of the W bosons. Each W can decay into a quark antiquark pair or to a charged lepton and an unobservable neutrino.

The mass of the W can be determined by two different methods. One way is from the total W -pair cross section σ_{tot} just above the W^+W^- production threshold where it is most sensitive to m_W . The second is the direct reconstruction of the invariant mass from its final state decay products. Due to the small production cross section of the W -pairs (< 20 pb) a very high integrated luminosity has to be provided by LEP to reach the desired statistics. The aim is to reach 500 pb^{-1} per experiment which corresponds to about 8000 W^+W^- events. The envisaged error for m_W is about $30\text{--}50 \text{ MeV}/c^2$ which requires a precise knowledge of the beam energy of the order of $\delta E_{\text{beam}} \leq 15 \text{ MeV}$ [Pla96]. The improved accuracy makes the test of the electroweak theory more stringent.

Besides the W studies, the further aims of increasing the LEP energy are the search for the Higgs boson, both standard and supersymmetric, as well as other supersymmetric particles like charginos and neutralinos. The W -pair production will also provide some information about the triple gauge-boson couplings for ZWW and γWW interactions.

3.2 The LEP e^+e^- collider

LEP [LEP84] is an e^+e^- colliding beam storage ring with a circumference of 26.7 km. It has an eightfold symmetry and consists of eight straight sections connected by circular arcs (see Fig. 3.2). Four of the straight sections house a physics experiment, i.e. L3, ALEPH, OPAL and DELPHI. These experiments are all general purpose detectors with almost complete solid angle coverage. They analyse the decay products of the collisions between the counter-rotating electrons and positrons.

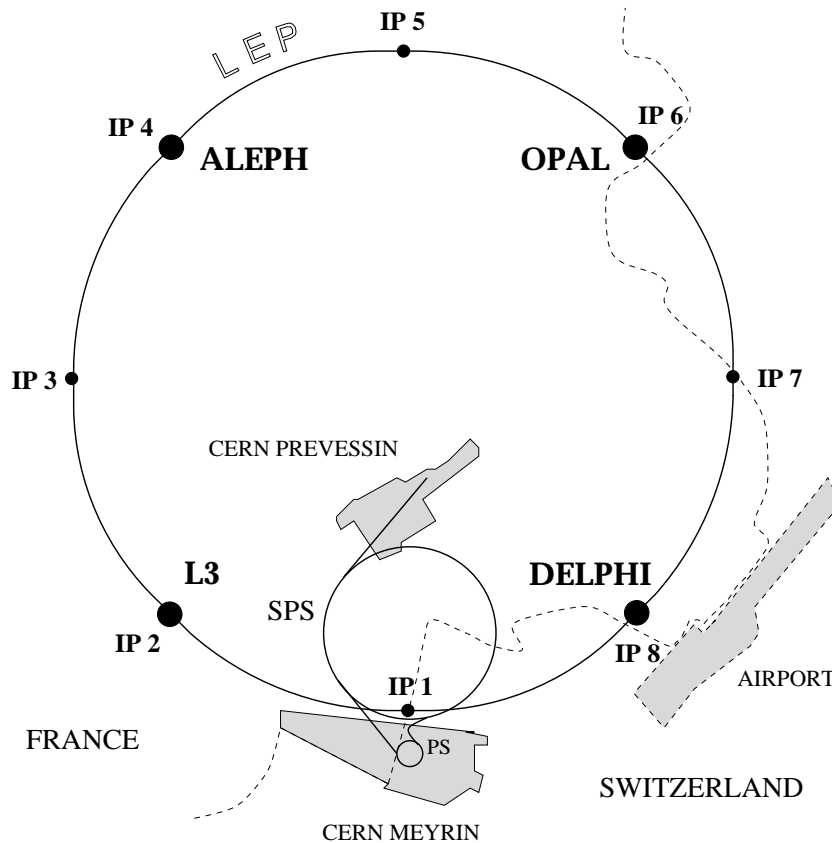


Figure 3.2: Schematic view of the LEP collider with its eight interaction points (IP). The four even-numbered IPs are equipped with experimental detectors.

QL1 – QL12	non-experimental straight section
QL13 – QL18	non-experimental dispersion suppressor
QS0 – QS12	experimental straight section
QS13 – QS18	experimental dispersion suppressor
QF19 – QF49	(odd numbers) horizontally defocusing regular FODO quadrupoles
QD20 – QD48	(even numbers) horizontally focusing regular FODO quadrupoles

Table 3.1: Naming scheme for the quadrupole magnets at LEP. A suffix $.Ln$ or $.Rn$ is added where L and R stand for left and right (seen from the centre of LEP) of the IP number n .

The magnetic lattice consists of a total of 808 quadrupole magnets. The magnets are numbered starting from each IP. The naming scheme is explained in Table 3.1. Some of the magnets are arranged in doublets and an suffix A or B is added to the name. The location of the magnet in the ring is given by the suffix $.Ln$ or $.Rn$ where L and R stand for left and right of the IP (seen from the centre of LEP) and n is the IP number. As an example, QS0.L2 stands for the first magnet at the left side of the experimental IP 2.

The eight quadrupole magnets (QS0) left and right of each of the four experimental IPs are superconducting to reach the desired strong gradient needed to squeeze the vertical beam size at the interaction points. All other magnets are normal conducting. Two different types of magnets are used which are different in magnetic length and number

of turns per pole. One type (MQ, 1.60 m long, 29 turns) is used for the regular arc FODO cells (QF, QD) and some insertion magnets (QL4 and QS2). The remaining quadrupoles in the straight sections and dispersion suppressors are of the second type (MQA, 2.00 m long, 59 turns).

An injector chain of linear and circular accelerators (e.g. PS, SPS) increases the energy of electrons and positrons to 22 GeV before they are injected into LEP. The particles are accumulated in a number of bunches. The initial design foresaw four equidistant bunches of electrons and positrons. This implies 8 collision points in the 8 interaction points of LEP. Electrostatic separators close to the interaction points separate the beams vertically and prevent unwanted collisions between the different bunches outside the experimental detectors.

Different schemes were used to raise the number of bunches to eight or more in order to increase the luminosity. A ‘*pretzel*’ scheme [Jow91] was used from 1992 to 1994 with 8 equidistantly spaced bunches. The unwanted collisions that would occur in the middle of the arcs were avoided by horizontal electrostatic separation at the beginning of the arcs. The horizontal electron and positron orbits are intertwined in the arcs (which lead to the name) and separated at the place where the bunches would encounter each other.

The present *bunch train* scheme [Her94] which was used since 1995 has four equally spaced *trains* which consist of up to four bunches each which follow one another at a distance of about 100 m. The separation for the unwanted collision points is obtained by vertical electrostatic separation bumps close to the interaction points.

After accumulation of the particles at injection energy they are accelerated to the collision energy. Until the end of 1995 LEP was operated at centre of mass energies around the Z resonance ($m_Z = 91.2 \text{ GeV}/c^2$) to profit from the high cross section for an accurate measurement of the Z mass m_Z and the width of the Z resonance Γ_Z . An important error in addition to statistic and systematic errors from the experimental detectors comes from error of the LEP beam energy. A careful absolute calibration was essential for a small error. The energy calibration at LEP will be described in Section 3.3.

Since the end of 1995, the maximum beam energy of LEP has been increased in steps. It is limited by the total installed RF voltage needed to replenish the energy lost by the emission of synchrotron radiation. The synchrotron radiation power increases with the fourth power of the energy, i.e. from a loss per turn of 120 MeV at 45.6 GeV to 2 GeV at 92 GeV. So the required RF voltage increases drastically.

Superconducting RF cavities were subsequently added and the beam energy increased from 65 and 68 GeV at the end of 1995, 80.5 GeV and 86 GeV in 1996, to 91.5 GeV in 1997. The beam energy will be increased to 94.5 GeV for the 1998 running period. A last upgrade is foreseen for the 1999 operation and it is envisaged to run LEP until the year 2000 to collect data above the W-threshold. A total of 288 superconducting RF cavities will be installed after full completion of the upgrade to compensate for the synchrotron radiation losses.

3.3 The LEP energy calibration

The accurate measurement of the average LEP beam energy is based on the resonant spin depolarization. The achievable precision is more than an order of magnitude better than that from other methods.

As described in Section 2.3, the spins of the circulating particles become polarized with time. This transverse spin polarization is measured at LEP by a Compton laser polarimeter [Deh95, Ass94b]. A circularly polarized laser beam is brought into collision with the electron or positron beam of LEP at IP 1. The cross section depends on both the polarization for electron and photons. The distribution of the backscattered photons is shifted for left- and right-hand circularly polarized light if the electron beam is polarized. This shift is proportional to the polarization P . The photon distribution is measured by a W-Si strip detector 250 m away from the interaction point.

The average statistical error of the polarization level ΔP_{stat} is of the order of [Ass94b]

$$\Delta P_{\text{stat}} = 0.6 \% \text{ min}^{-1/2}. \quad (3.1)$$

The polarization can be destroyed in a resonant way by applying an oscillating horizontal RF field to the beam. This field rotates the spin vector by a small amount every turn. The small rotations add up coherently if the frequency f_{dep} of the depolarizing RF field meets the resonance condition with the spin precession frequency

$$f_{\text{dep}} = (k \pm q_\nu) \cdot f_{\text{rev}} \quad \nu = k_\nu + q_\nu \quad (3.2)$$

where $f_{\text{rev}} = 11\,246$ Hz is the revolution frequency of LEP, k is any integer, and k_ν and q_ν are the integer and fractional part of the spin tune ν , respectively. In that case the polarization vector is rotated into the horizontal plane in about 10^4 turns (~ 1 s) and the polarization is destroyed by the spin diffusion. For the measurement, the frequency f_{dep} of the RF field is varied until depolarization is observed.

Only the fractional part q_ν is measured but the integer part k_ν can be derived from measurements of the main bending field. There is still an ambiguity since depolarization also occurs when $(1 - q_\nu)$ meets the resonance condition (mirror ambiguity). This is resolved by a second depolarization after a known energy shift by changing the RF frequency. Another uncertainty from depolarization from synchrotron sidebands $q_{\text{side}} = q_\nu \pm Q_s$ can be disentangled by a depolarization after change of the synchrotron tune Q_s since the main resonance does not change with a change of Q_s .

The average beam energy is derived from this measurement using Eq. 2.35. The method has a small error of a few ppm since the values entering the calculation (f_{dep} , f_{rev} , m_e and a) are known to a high precision. The total systematic error was calculated to be $\Delta E = 0.2$ MeV at 45.6 GeV and an experimental verification with limited accuracy showed an upper limit of this error of $\Delta E = 1.1$ MeV [Arn95].

An indispensable prerequisite for this precise measurement is a sufficient degree of polarization. If the level of polarization is not high enough, the depolarization can not be clearly identified in the statistic fluctuations of the measurement. The experience has shown that measurement with a polarization level of 4-5 % is usually possible. Lower levels make the measurement extremely difficult or impossible.

Different strategies are applied to attain a high degree of polarization. First of all, the vertical orbit is carefully corrected to minimise horizontal fields passing off-centre in quadrupole magnets. While a vertical rms of 0.5 mm is common for physics data taking, the orbit for polarization experiments is usually corrected to below 0.3 mm. The longitudinal magnetic fields of the experimental solenoids (if excited) are compensated by vertical closed orbit bumps close to the solenoids. The spin rotation by the bumps is calculated such that it nulls the rotation by solenoids.

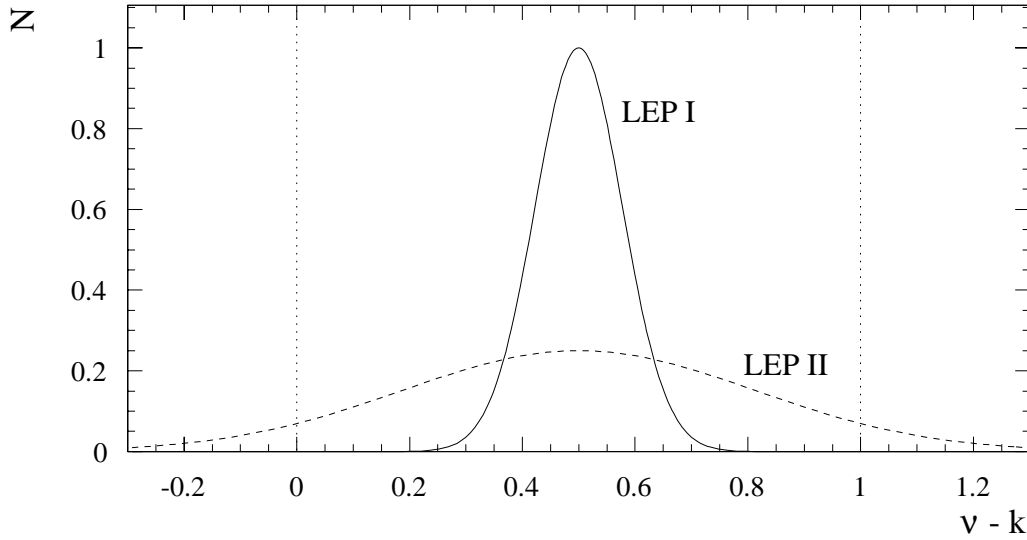


Figure 3.3: Energy spread σ_ε at LEP for a particle distribution centred at a half integer spin tune $k + 0.5$ ($k \in \mathbb{N}$). The width of the distribution is 30 MeV for LEP I around 45 GeV beam energy and increases to 125 MeV for LEP II.

The energy of LEP is set such that the spin tune is near $\nu = k + 0.5$ ($k \in \mathbb{N}$) and far from the main resonances. The tunes are carefully chosen to avoid depolarizing resonances from betatron and synchrotron sidebands as in Eq. 2.38. The tunes were usually smaller than in conditions for physics data taking since the strength of the resonances decreases with their order.

The most successful method of increasing the polarization level at LEP was the *Harmonic Spin Matching* (HSM) (see Section 2.4). A record polarization level of $(57 \pm 3)\%$ was achieved at 44.7 GeV [Ass94b]. This was obtained with initial deterministic HSM from the Fourier analysis of the closed orbit followed by empirical HSM.

The depolarizing effects become more severe with the increase in energy. According to Eq. 2.19, the energy spread σ_ε scales proportional to the square of the energy itself. While it is around 30 MeV for LEP operated at 45 GeV, it increases to more than 120 MeV for LEP II. A significant fraction of the particles in the distribution passes the depolarizing integer resonances which are 440 MeV apart (see Fig. 3.3). In the mathematical picture, this effect becomes obvious in the strength of the synchrotron sidebands by the increase of the tune modulation index λ (see Eq. 2.44) with the fourth power of the energy.

This effect will limit the polarization level for higher energies below the threshold needed for resonant depolarization. The level is certainly insufficient at the operation energy above the W-threshold and a direct measurement is impossible. The precise measurements by depolarization have to be extrapolated to the operation energy by other means which are based on the measurement of the LEP bending field.

Different devices measure the field of the LEP dipole magnets. A total of 16 NMR probes are installed in bending magnets in the 8 octants of LEP [Deh96]. While the intrinsic precision of the probes is better than $5 \cdot 10^{-6}$, the field measurements are limited to the order of 10^{-4} by the local differences and irreproducibility due to the magnetic properties of the LEP concrete-iron dipole magnets. Hence, these local field measurements have to be related to the average beam energy by resonant depolarization measurements.

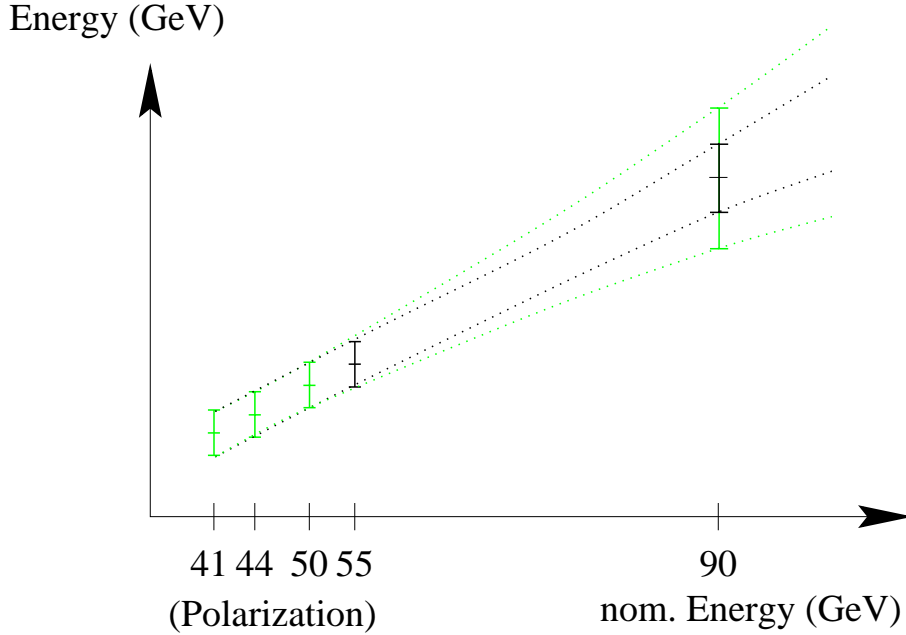


Figure 3.4: The error in the energy measurement by flux-loop and NMR will depend on the linearity in the lower region and on the length of the lever arm for extrapolation. A calibration at higher energy reduces the lever arm and extrapolation error. The graph is not to scale.

A special *flux-loop* [Bil90] coil inside the LEP main dipoles forms a loop all around the ring covering 96.5 % of the total bending field. The total flux induced inside during a special hysteresis loop is used to monitor the magnetic induction of the dipoles. The precision of the method is about $\Delta E/E = 2.6 \cdot 10^{-4}$. While it has the advantage of essentially sampling the whole ring, it is not applicable with stored beams and does not take into account other magnetic fields like the earth magnetic field.

Both methods are not necessarily linear over the energy range to be covered for the extrapolation. It is thus indispensable to perform calibration measurements between NMR, flux-loop and the precise resonant depolarization at several energies to get information about the linearity of the methods. The final error on the extrapolation to the operation energy will crucially depend on the energy range which has to be covered. This is indicated in Fig 3.4.

A resonant depolarization measurement has to be performed at the highest possible energy where a sufficient degree of polarization is achievable. Since the strength of the depolarizing resonances scales with γ^2 (see Eq. 2.45) and the strength of the sidebands scales with γ^4 (see Eq. 2.44), it becomes much more difficult to reach a high degree of polarization. The compensation of the resonances by Harmonic Spin Matching therefore has a more important role. In particular, the deterministic HSM which depends on the BPM offsets has to be accurate enough to provide an observable level of polarization for further empirical optimisation. Accordingly, the determination of the BPM offsets is of specific importance for the energy calibration at higher energies. This beam based alignment can help to decrease the error on the W mass.

Chapter 4

Calibration of orbit monitor offsets

For a good performance of an accelerator it is important that the beam passes centred through the quadrupole magnets, as it was shown in Chapter 2. The precise knowledge of the vertical orbit is also relevant for the compensation of depolarizing spin resonances.

Beam position monitors are installed near the quadrupoles to measure the orbit position at these locations. Due to cost reasons, the number of monitors is limited. For example, there are 504 BPMs installed at LEP. They are located in the straight sections and at the vertically focusing quadrupoles in the arcs where the beta function is large and the adverse effects of a beam passing off-centre is bigger. They are manufactured with tight mechanical tolerances and are carefully aligned relative to the quadrupoles. Nevertheless, a residual mechanical offset can persist and an electrical offset can also lead to an error on the determination of the beam position.

A beam based technique has been developed to find the offset of the beam position monitors [Bar94].

4.1 Principle of quadrupole strength modulation

The underlying principle of the offset determination of the beam position monitors is based on the focusing properties of a quadrupole magnet. Eq. 2.22 shows that a particle gets an additional angular deflection $\Delta y'$ when the strength of a quadrupole changes by some small Δk . This kick depends linearly on the orbit position y_Q relative to the centre of the magnet. This leads to an orbit change $\Delta y(s)$ according to Eq. 2.23 which is detectable all around the ring (except the locations where $\cos(|\mu(s) - \mu(s_0)| - \pi Q) \simeq 0$). This orbit change is also proportional to the distance the particle passes from the centre of the magnet where the gradient is changed. A measurement of this orbit change $\Delta y(s)$ for different beam positions y_Q in the quadrupole allows the determination of the centre of the magnet, as it is shown in Fig. 4.1. A simultaneous reading of the beam position monitor at the quadrupole magnet shows the offset of this BPM.

This technique is used at various accelerators [Ric83, Lit85, Røj94, Bög95]. Usually, the orbit is measured, the strength of the quadrupole changed and the orbit is remeasured for different beam positions in the particular quadrupole magnet. The orbit change is minimal when the beam is centred in the magnet.

A different technique has been developed at CERN to adapt better to the special requirements there. The quadrupole strength k is *harmonically* varied at a low frequency f

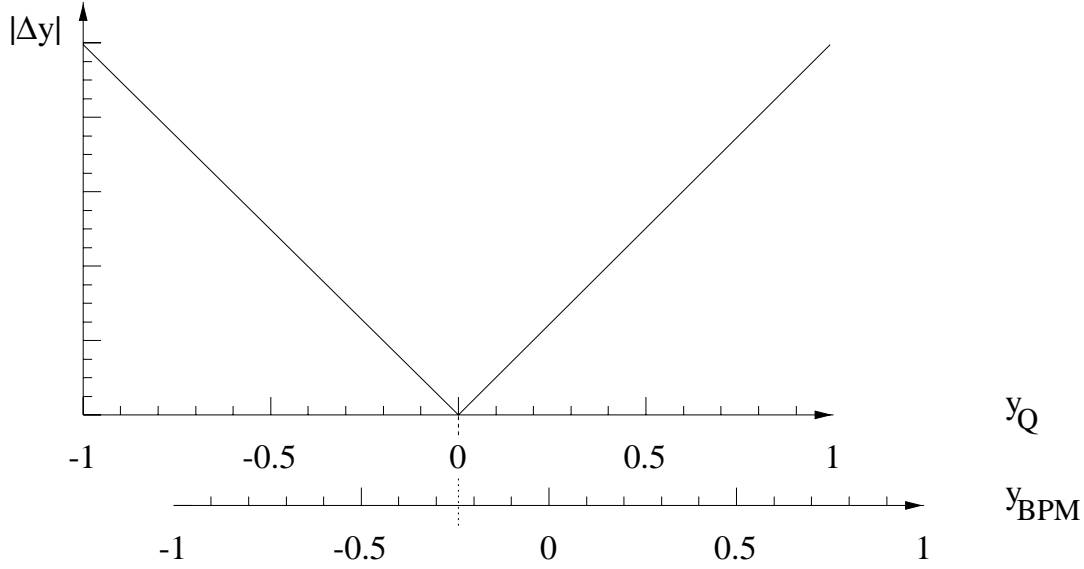


Figure 4.1: Measurement of the orbit change Δy for different beam positions y_Q in the quadrupole where the field strength k is changed. The offset of the beam position monitor is obtained from reading at the position of minimum orbit change Δy .

well below the betatron frequency

$$\Delta k = \Delta k_0 \cdot \cos(2\pi f t + \phi_0) \quad (4.1)$$

where ϕ_0 is the initial phase of the excitation.

According to Eq. 2.22 and Eq. 2.23, this leads to a beam oscillation with the same frequency. The induced beam oscillations are measured by a sensitive beam position monitor. A harmonic analysis of this signal determines the amplitude of the beam oscillation at the excitation frequency. The amplitude shows the same behaviour as $|\Delta y|$ in Fig. 4.1 and the BPM reading at its minimum is the BPM offset.

This variation of the technique has a few advantages compared to the other. The method is rather insensitive to orbit movements from other sources when these do not have the same frequency as the modulation and the measurement is not perturbed. This is important in the case of LEP since the vertical orbit is strongly drifting (see Chapter 5).

Consequently, the relative gradient change $\Delta k_0/k$ can be very small and the modulation signal is still detectable. The modulation can be kept so small that the changes in any other beam parameters like orbit, tunes and betatron functions are negligible for normal operation. Hence, it does not disturb the physics data taking by the experiments. So the offset determination can be performed in parallel to physics data taking which is the main fraction of the LEP running time. No specially scheduled machine time is needed for the offset determination.

The harmonic excitation also allows to measure the offsets of several beam position monitors at the same time by choosing different excitation frequencies. The harmonic analysis can extract the oscillation amplitude when the spacing between the frequencies is sufficiently large (see Section 4.3.3).

4.2 Hardware description for k-modulation

4.2.1 Modulation of quadrupole strength

A necessary prerequisite for the offset determination is the possibility to change the gradient of a particular quadrupole magnet independently.

Most of the quadrupoles at LEP are powered in series, only a few have individual power converters (QS0, QS1 and QS5 at the experimental interaction points). The other quadrupole magnets in the straight sections and dispersion suppressor are powered in symmetrical pairs around the interaction point. All quadrupoles in the arcs are connected in one series each for the horizontally focusing (QF) and the defocusing (QD) magnets.

These quadrupole magnets had to be equipped with additional (back leg) windings to allow a modulation of the quadrupole strength. These additional windings are made from a 8 wire cable with 0.75 mm^2 cross-section which is wound once around the poles on top of the main windings of the magnet. The wires are connected to form 8 turns. The cable is galvanically isolated from the main windings. 16 power converters with a maximum current of $I_{p-p} = 12 \text{ A}$ excite the back leg windings. The power converters can perform a harmonic excitation with frequencies between 0.72 and 50 Hz. Two power converters are installed at every interaction point of LEP. One quadrupole magnet in the half-octant on each side of the IP can be connected via the power cable to the harmonic generator. A multi-wire control cable selects the desired back leg winding with the help of a diode selection matrix and a relay near each quadrupole.

Very low frequencies have to be used for the offset determination. The back leg winding and the main winding act like a transformer. The harmonic excitation of the back leg winding induces a voltage in the main winding of the magnet. This leads to a current change in the main windings and also changes the magnetic field in the magnets which are powered in series with this magnet. The induced voltage is smaller for lower frequencies. In addition, the current regulation loop of the main power supply has a better rejection of current variations for small frequencies.

The coupling between the magnets of a pair connected in series was measured as a function of the excitation frequency. The magnetic field change inside the quadrupole was measured when the modulation was on this magnet and then on the magnet connected in series. Fig. 4.2 shows the ratio of the two measurements. The modulation frequency has to be chosen below about 2 Hz to keep the influence on the second quadrupole magnet connected in series small enough. For higher frequencies, the field in the second magnet changes by nearly the same amount as in the magnet with the modulation. A badly centred orbit in the second quadrupole magnet can result in a significant measurement error.

All defocusing regular lattice quadrupole magnets (QD) in the arcs are connected in series with a total of 240 magnets in the string. The induced voltage by the back leg excitation of a single magnet has thus a smaller effect on the relative change of the total voltage compared to the case of a quadrupole pair. This results in a smaller current change in the main windings. In addition, the orbit positions in the different magnets can be assumed to be statistically distributed. The additional kicks are like a random walk to the beam which again decreases the effect by the order of $\sqrt{240}$. So the error by the unwanted modulation of quadrupoles other than the excited one is smaller than for a commonly powered magnet pair. Nevertheless, frequencies below 2–3 Hz were usually chosen for the excitation.

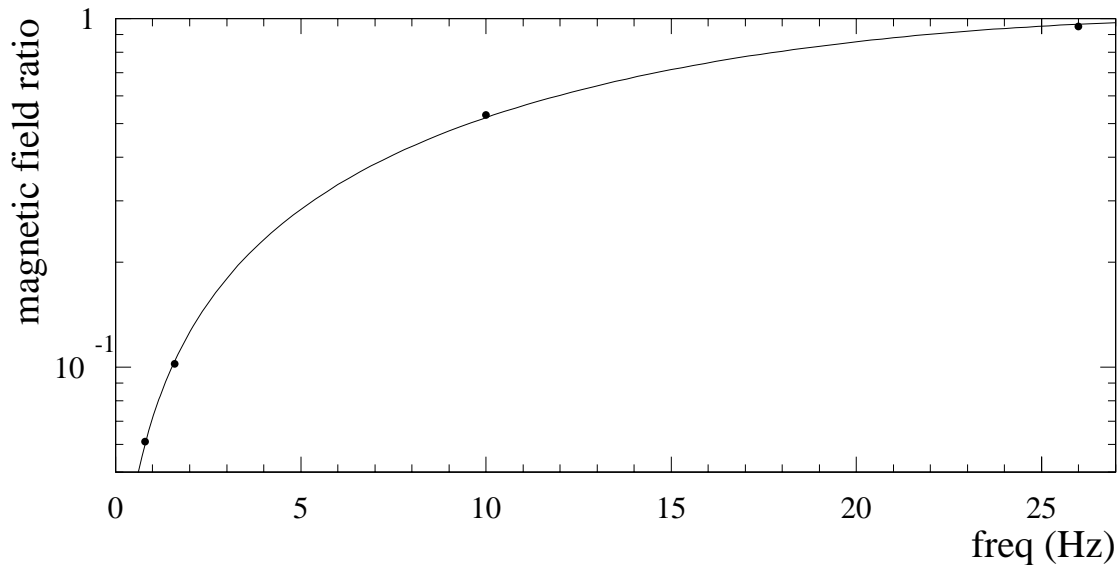


Figure 4.2: Ratio between the magnetic field when the excitation is on the back leg winding of the magnet itself and on the magnet connected in series for a string of two magnets.

The field in the magnets with an individual power supply can be modulated at higher frequencies by changing the current in the winding of the magnet. For these magnets, modulation frequencies in the range of 10 to 16 Hz were chosen since beam oscillations in this range are relatively small (see also Fig 4.5). Due to technical reasons, the excitation is not harmonic but the current is periodically changed between two values. The inductance of the coil prevents the current changes from being purely rectangular. But higher odd harmonics of the fundamental frequency will be present in the frequency analysis.

The signals to ramp these magnets up and down are generated by the LEP Master Timing Generator (MTG) and are distributed around the ring. A 2.5 s table contains a synchronisation event at the beginning of the table and the events for 8 excitation frequencies between 10.0 and 15.6 Hz, spaced by 0.8 Hz.

4.2.2 The Beam Orbit Measurement system

The Beam Orbit Measurement (BOM) system of LEP consists of 504 pickups that are capable of measuring the positions of the two beams in the two planes with a relative precision of a few microns. The pickups are made of an Al blocks (stainless steel in the straight sections) and contain four round stainless steel button-type electrodes of 34 mm diameter. The passing bunch induces a signal in the electrodes which is proportional to the bunch currents and depends on the distance from the electrode. The bunch position is calculated from the ratios of the different signals.

The BOM pickups are rigidly fixed by a mount to the quadrupole magnets. Nearly every quadrupole in the straight section and the dispersion suppressor is equipped with a pickup. In the arcs of LEP, only the vertically focusing magnets, the QDs (every other quadrupole magnet), have a pickup.

Two different types of processing electronics are used to determine the beam position. A wide band type is used for pickups close to the IPs where the time separation between

the counter-rotating bunches is small and time resolution is critical. A narrow band type with lower time resolution is used for most of the pickups. The different types are briefly described below. A more complete description is given in [Bor90, Bor95].

The BOM system has two parallel acquisition modes. The orbit can be acquired by request of the operator and an automatic orbit acquisition takes a new measurement every fixed time interval. The automatically acquired orbit which is measured every 60 s is used for the offset determination*. More frequent automatic acquisition would make an orbit measurement for the operator unavailable. For this reason, the repetition period of the automatic acquisition is limited to 40–60 s.

Wide Band BOM

Until end of 1996, only 56 pickups were read by a wide band processing electronics, 3 at each side of the non-experimental interaction points (at QL1B, QL2B and QL4B) and 4 at each side of the experimental IPs (at QS0, QS1A, QS3 and QS4). The electronics for four additional pickups (at QS5 to QS8) at each side of the experimental IPs has been changed to the wide band type for 1997. This allows the observation of both particle types which had been impossible for the bunch train operation.

A 12 bit resolution ADC is used to digitise the signal of each of the four electrodes separately. The electronics is not self adjusting and is dependent on the bunch currents. A gain must be selected to set the working point corresponding to the bunch currents. The gain is changed usually once in normal physics data taking conditions.

Narrow Band BOM

The processing electronics for most of the pickups is of the narrow band type. The electronics is self adjusting to the bunch current, no gain settings have to be selected. It uses a 8 bit Flash ADCs to digitise the difference signals for the two diagonally opposite electrodes of the pickup.

The initial resolution with 8 bit was $\simeq 140 \mu\text{m}$ in the vertical plane. The resolution is increased by an equivalent of 3 bits by ramping the FADC input pedestal in steps of 1/8 of a bin at each revolution period. This technique has increased the resolution to $16 \mu\text{m}$ in the vertical and $11 \mu\text{m}$ in the horizontal plane.

4.2.3 Detection of beam oscillations

The change in the quadrupole strength should be small enough not to interfere with the accelerator operation for data taking by the physics experiments. The relative change $\Delta k/k$ is typically of the order 10^{-3} to 10^{-4} . The induced beam oscillations have an amplitude of only up to a few micrometres. The resolution of the normal BPM system is marginal for these small oscillations.

Two high resolution beam position monitors have been installed at LEP for general purpose use [Vos94]. They are directional coupler type strip line monitors with four electrodes of 18 cm length.

*For some time this was decreased to 40 s.

	name	s [m]	β_x [m]	β_y [m]	μ_x [2π]	μ_y [2π]
until 1996	BPCO.QF31.R1	957.03	115.03	43.35	3.104	3.152
until 1996	BPCO.QF31.L1	25 701.84	116.76	42.82	87.184	73.042
1997	BPCO.QL8.R1	175.95	58.72	63.25	0.638	0.917
1997	BPCO.QL8.L1	26 482.92	58.72	63.26	89.647	75.277

Table 4.1: Characteristic values for the strip line beam position monitors (couplers) for an optics with 90/60° phase advance per FODO cell (1996: m05p80_v2, 1997 n0520p97_v2).

The position of the couplers has been changed in the 1996/97 shutdown since they were suffering from the higher amount of synchrotron radiation at LEP II. They were located in the arc near the quadrupole magnet QF31, about 950 m left and right of interaction point 1. They were moved into the straight section close to QL8, 175 m from IP 1. The strip lines of the couplers are in the horizontal and vertical plane. One of the couplers was turned by 45° before the relocation and a hybrid electronics was used to generate the signals for the horizontal and vertical plane. Some details of the location of the couplers and the betatron functions and phases there are given in Table 4.1.

Using two couplers assures that any beam oscillation can be detected. The betatron phase advance between the source of the orbit oscillation and one coupler can make the oscillation nearly vanish at the location of the coupler. The cosine term in Eq. 2.23 should not become zero for both couplers at the same time.

This condition is fulfilled depending on the phase μ of the source of an oscillation for a phase advance $\Delta\mu = \mu_2 - \mu_1$ between the two couplers with phases μ_1 and μ_2 if

$$\Delta\mu \not\approx \begin{cases} n\pi & : \mu < \mu_1 \\ 2\pi Q + n\pi & : \mu_1 < \mu < \mu_2 \\ n\pi & : \mu_2 < \mu \end{cases} \quad (4.2)$$

If the phase advance $\Delta\mu$ between the two couplers is not close to a multiple of π and not close to $2\pi Q + n\pi$, the oscillation is detectable in at least one of the couplers, no matter where the source is located.

The displacement $\Delta y(s_{\text{cpl}})$ of the beam at the location of the coupler for an orbit kick is $\Delta y'$ at a location s is given by Eq. 2.23. Let us define the sensitivity s_x and s_y of the couplers for orbit kicks at any location as the beam displacement in the coupler divided by the strength of the kick. It follows in the case of the vertical plane

$$s_y = \frac{\Delta y(s_{\text{cpl}})}{\Delta y'(s)} = \frac{\sqrt{\beta(s) \cdot \beta(s_{\text{cpl}})} \cos(|\mu(s_{\text{cpl}}) - \mu(s)| - \pi Q)}{2 \sin(\pi Q)}. \quad (4.3)$$

The expression for the horizontal plane is similar.

Fig. 4.3 shows an example in the vertical plane for the 1997 coupler configuration for the optics with phase advances μ_x/μ_y of 90/60° per FODO cell. The graph shows the variation of the sensitivity with the beta function. It can be seen that there is always one coupler where the sensitivity is not zero.

4.2.4 Data acquisition system

The data acquisition system has 8 channels to measure simultaneously the signals of both couplers in both horizontal and vertical plane for the two particle types.

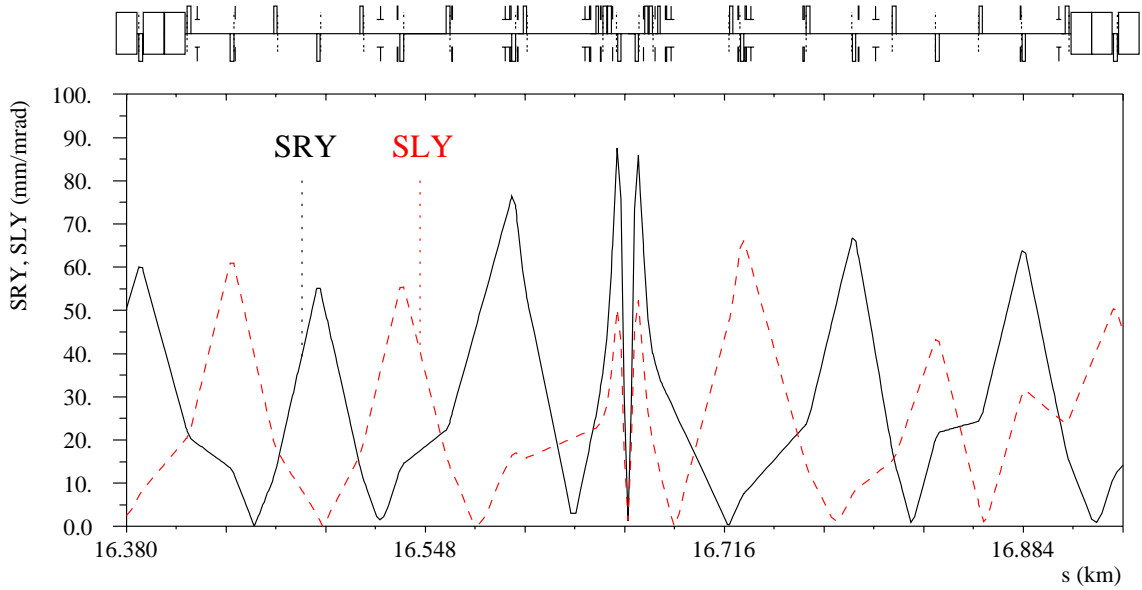


Figure 4.3: Sensitivity (see Eq. 4.3) of the two couplers for vertical orbit kicks around one interaction point (IP 6) for the 1997 90/60° phase advance optics (n0520p97_v2). The drawing on top of the graph depicts the magnet structure for the region shown.

The difference signal of the strip-line pairs for each of the planes is used for the detection of the oscillations. The amplitude is proportional to the bunch current and changes during the fill. The normalisation for the bunch current is made by software with the on-line current readings from the LEP measurement database.

The difference signal is fed into an integrate and hold circuit (I/H). Four multiplexed 12 bit ADC digitise the signal and a DSP is used for data processing. A detailed description of the acquisition electronics can be found in [Rei94].

The electronics needs $13 \mu\text{s}$ for the digitisation. Four bunch passages can be measured per revolution period of LEP. The electronics is not fast enough to measure all successive bunchlets in a bunch train but the trigger allows to select any of them. The data for each channel is averaged by the DSP over n_{av} turns. The DSP is capable of storing 16k of data. If all 8 channels are to be simultaneously measured, 2048 data points can be acquired for each channel.

The data acquisition is synchronised by the master timing generator of LEP. A VME timing module (TG3) [Bee90] detects the synchronisation timing event and triggers the data acquisition. So the excitation and measurement are synchronised and the phase of the oscillation can be used as an additional information.

4.3 Data analysis

The beam position is sampled over a number of successive turns. The average is calculated for n_{av} bunch passages (see also Section 4.3.2). The sampling frequency f_{sampl} is determined by

$$f_{\text{sampl}} = f_{\text{rev}} \cdot N_{\text{bunch}} / n_{\text{av}} \quad (4.4)$$

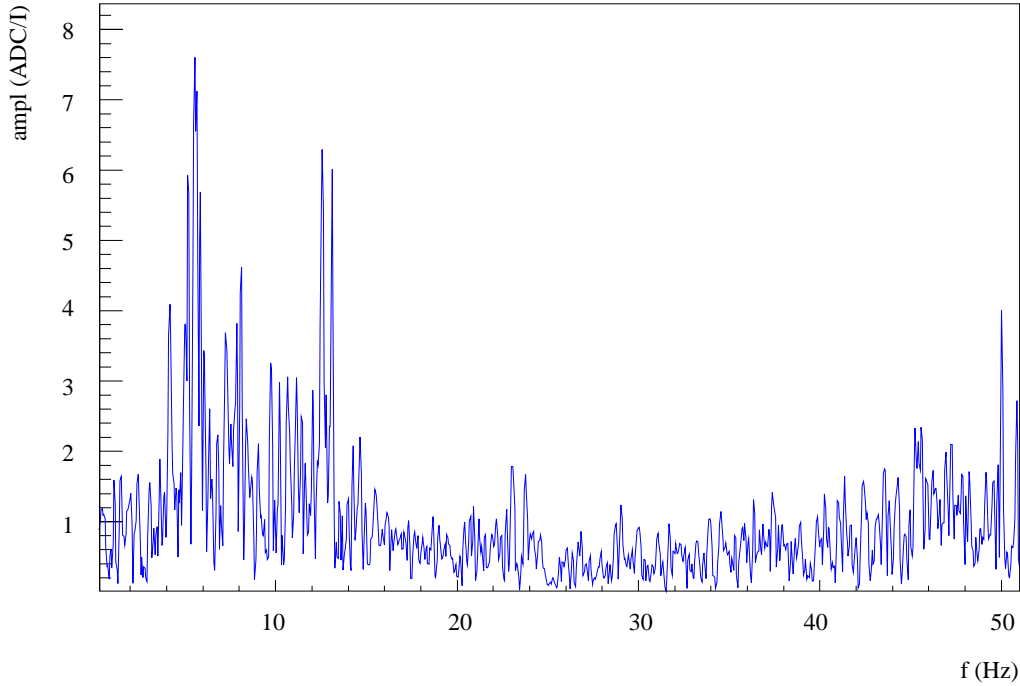


Figure 4.4: Spectrum of beam oscillations in the horizontal plane. The sampling frequency was 112.46 Hz. Data are from the coupler BPCO.QL8.R1 for the positrons.

where $f_{\text{rev}} = 11\,245$ Hz is the revolution frequency of LEP and $N_{\text{bunch}} = 4$ is the number of bunches that are measured per revolution cycle. The sampling period is $\tau = 1/f_{\text{sampl}}$.

A number of data points N_{data} has to be acquired for each data set for the frequency analysis. The acquisition time T needed for one data set is

$$T = N_{\text{data}} \cdot n_{\text{av}} / (N_{\text{bunch}} \cdot f_{\text{rev}}) \quad (4.5)$$

The nearest power of 2 smaller or equal to N_{data} is used for a Fast Fourier Transform (FFT) of the data for display. The FFT is described in [Rei94]. Examples of the spectra for the horizontal and vertical plane are shown in Fig. 4.4 and Fig. 4.5. While the FFT is suited for a fast calculation of the spectrum for display purposes, it has certain disadvantages for the precise analysis of the data. The amplitude can only be calculated for a discrete set of frequencies which are a multiple of the frequency f_{bin} given by

$$f_{\text{bin}} = f_{\text{sampl}} / N_{\text{data}}. \quad (4.6)$$

When the frequency does not coincide with one of this set, the calculated amplitude has a strong dependence on the frequency [Har78]. To avoid this problem, a harmonic analysis is performed for the exact calculation of the oscillation amplitude.

4.3.1 Harmonic analysis

The harmonic analysis by a discrete Fourier Transform (DFT) allows a precise calculation of the amplitude of a harmonic oscillation

$$u(t) = A \cdot \cos(2\pi ft + \phi) \quad (4.7)$$

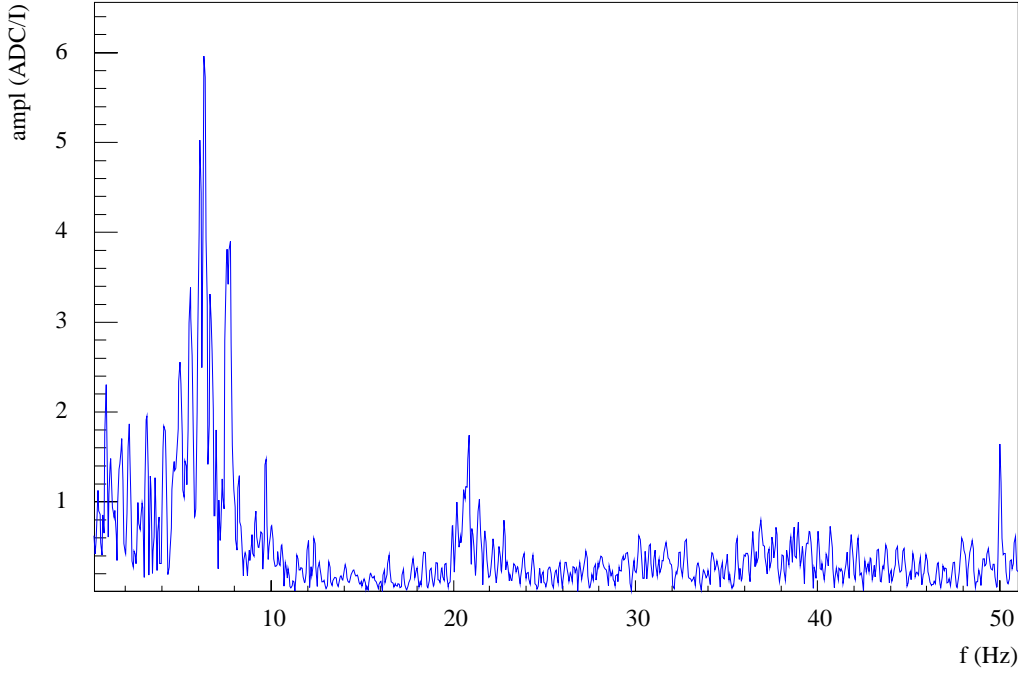


Figure 4.5: Spectrum of beam oscillations in the vertical plane. The sampling frequency was 112.46 Hz. Data are from the coupler BPCO.QL8.R1 for the positrons.

if the frequency f is smaller than the Nyquist frequency $f_N = f_{\text{sampl}}/2 = 1/(2T)$.

It is based on the function

$$\tilde{u}(f) = \sum_{k=0}^{N-1} u(t_k) \cdot e^{-2\pi i f t_k} \quad (4.8)$$

where $u(t_k)$ is the transverse beam position sampled at equidistant times $t_k = k \cdot \tau$.

The function $\tilde{u}(f)$ can be written as $C(f) + iS(f)$, where $C(f)$ and $S(f)$ are real numbers given by

$$C(f) = \sum_{k=0}^{N-1} u(t_k) \cos(2\pi f t_k) \quad S(f) = \sum_{k=0}^{N-1} u(t_k) \sin(2\pi f t_k).$$

The amplitude A and the phase ϕ of the harmonic oscillation in Eq. 4.7 (as demonstrated in Appendix A) can be reconstructed by

$$A(f) = \frac{2}{N} \sqrt{C(f)^2 + S(f)^2} \quad \phi(f) = -\arctan\left(\frac{S(f)}{C(f)}\right).$$

This analysis can be performed at any frequency f below f_N and the result is independent of the frequency for a large number of data points $N \gg 1$.

4.3.2 Sampling effects

The beam oscillations are only sampled at one location for a limited time interval. This has certain effects on the frequency resolution and precision of the analysis.

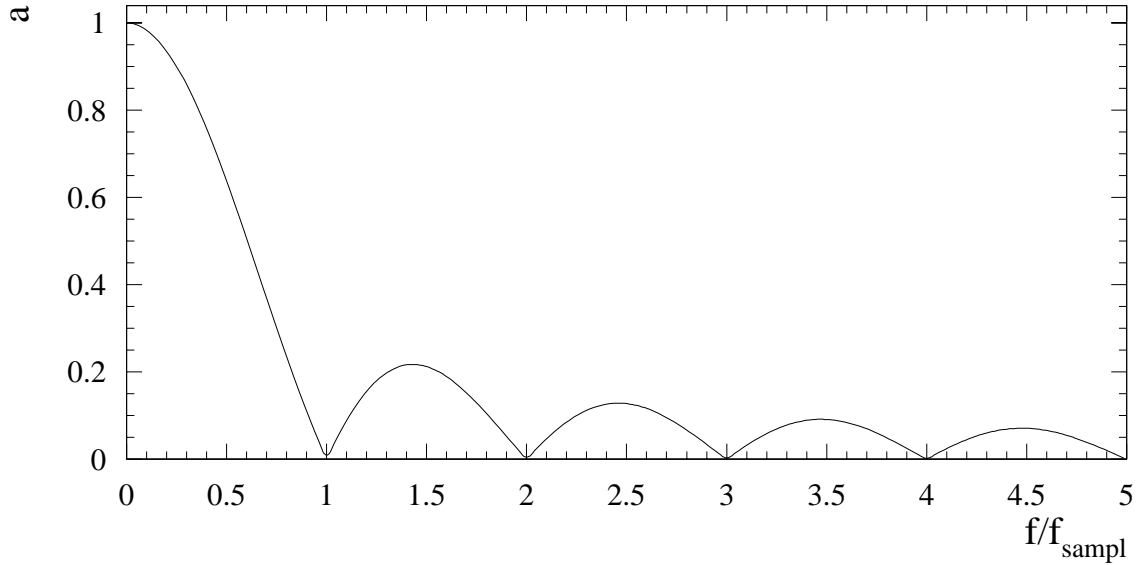


Figure 4.6: Attenuation factor a for the calculated amplitude of an harmonic oscillation as a function of the frequency.

The original signal of the beam oscillations is not bandwidth limited below the Nyquist frequency f_N . I.e., the betatron oscillations are seen with the fractional part q of the betatron tune Q . For the vertical plane with $q_y = 0.19$, this is a frequency of $f = q_y f_{\text{rev}} \simeq 2100$ Hz.

As a consequence, simple sampling would lead to aliasing (see Appendix A.2). Any higher frequency content of the signal would be spuriously moved into the interval $[0 \dots f_{\text{sampl}}/2]$ and perturb the measurement. All signals in the intervals $[m \dots m+1] \cdot f_{\text{sampl}}$, $m \in \mathbb{Z}$ are shifted to $[0 \dots f_{\text{sampl}}]$. Furthermore, signals in the range $[f_{\text{sampl}}/2 \dots f_{\text{sampl}}]$ are mirrored about $f_{\text{sampl}}/2$ into $[0 \dots f_{\text{sampl}}/2]$. So, the result of the DFT at frequency f in the interval $[0 \dots f_{\text{sampl}}/2]$ is a superposition of signals with frequencies $m \cdot f_{\text{sampl}} \pm f$.

Aliasing is avoided by a low pass filter for the signal before the harmonic analysis is performed. The averaging of the beam position for n_{av} successive bunch passages is a digital low-pass filter. Instead of taking one measurement every time interval τ , the mean of n_{av} measurements is used. For the harmonic analysis, the function $u(k\tau)$ is replaced by

$$\bar{u}(k\tau) = \frac{1}{n_{\text{av}}} \sum_{j=0}^{n_{\text{av}}-1} u \left(\left[k + \frac{j}{n_{\text{av}}} \right] \cdot \tau \right). \quad (4.9)$$

Appendix A.3 demonstrates that the calculated amplitude of an oscillation with a frequency f is attenuated by a factor a

$$a(\xi) = \left| \frac{\sin(\pi\xi)}{n_{\text{av}} \cdot \sin(\pi\xi/n_{\text{av}})} \right| \quad (4.10)$$

with $\xi = f/f_{\text{sampl}}$. Fig. 4.6 shows the effect. While this attenuation factor is between 1 and 0.64 in the interval between DC and the Nyquist frequency, it rapidly decreases for higher frequencies.

The sampling frequency is usually in the range between 50 and 250 Hz, so betatron oscillation signals are effectively suppressed. The highest frequency used for the offset determination is 15.6 Hz and the attenuation of the measured amplitude is very small.

4.3.3 Windowing

The use of the raw data (rectangular window) for the frequency analysis has a major disadvantage. A harmonic signal is not only detected at its frequency but also creates sidelobes in adjacent bins (spectral leakage) and distorts the measurement there. This is not tolerable since only a small frequency region is possible for the back leg winding modulation and several frequencies are to be used simultaneously.

The use of a windowing function for the raw data can significantly decrease the sidelobes and increase the frequency resolution. The value $v(i)$ of the data point i is multiplied by a weighting factor $w(i)$

$$v_w(i) = w(i) \cdot v(i). \quad (4.11)$$

A detailed comparison of the properties of several windowing functions is given in [Har78]. Two windows seemed particularly interesting and were selected for further analysis for this application: the *minimal 4-term Blackman-Harris* window and the *Hamming* window. The Blackman-Harris window has the strongest suppression of sidelobes while the Hamming window has a relative small peak width for a reasonable sidelobe suppression.

The weighting functions for these windows are

$$w_{\text{BH}}(i) = 0.35875 - 0.48829 \cdot \cos(2\pi i/N_{\text{data}}) + 0.14128 \cdot \cos(2 \cdot 2\pi i/N_{\text{data}}) - 0.01168 \cdot \cos(3 \cdot 2\pi i/N_{\text{data}}) \quad (4.12)$$

$$w_{\text{Ham}}(i) = 0.53856 - 0.46144 \cdot \cos(2\pi i/N_{\text{data}}) \quad (4.13)$$

and are shown in Fig. 4.7.

The windowing function decreases the calculated amplitude A of a harmonic signal. The reduction factor is 2.78746 for the minimum 4-term Blackman-Harris window and 1.85680 for the Hamming window. This is taken into account and compensated in the calculation of the amplitude.

The spectral leakage is significantly reduced for both windows. Fig 4.8 shows the comparison of the analysis of a harmonic signal after convolution with the 4-term Blackman-Harris window and Hamming window to the case without window. The sidelobes are significantly suppressed for both windows compared to the rectangular window at the expense of the broadening of the main-lobe. The suppression of sidelobes is better for the Blackman-Harris window while the Hamming window has a narrower peak width. The full width at half maximum of the main lobe are 1.20, 2.66 and $1.82 \cdot f_{\text{bin}}$ for the rectangular, Blackman-Harris and Hamming window, respectively. The width of the peak and the distance to the sidelobes scales with the bin width f_{bin} and is inversely proportional to the measurement time.

Without window, the calculated amplitude $3.5 \cdot f_{\text{bin}}$ away from the signal frequency is 9.2% of the signal amplitude, while it is only 0.2% with the 4-term Blackman Harris window and 0.6% with the Hamming window. At a distance of $2.5 \cdot f_{\text{bin}}$ from the signal frequency, the computed amplitude is 12.8% and 6.8% of the signal amplitude for rectangular and Blackman-Harris window, respectively. The Hamming window has a leakage

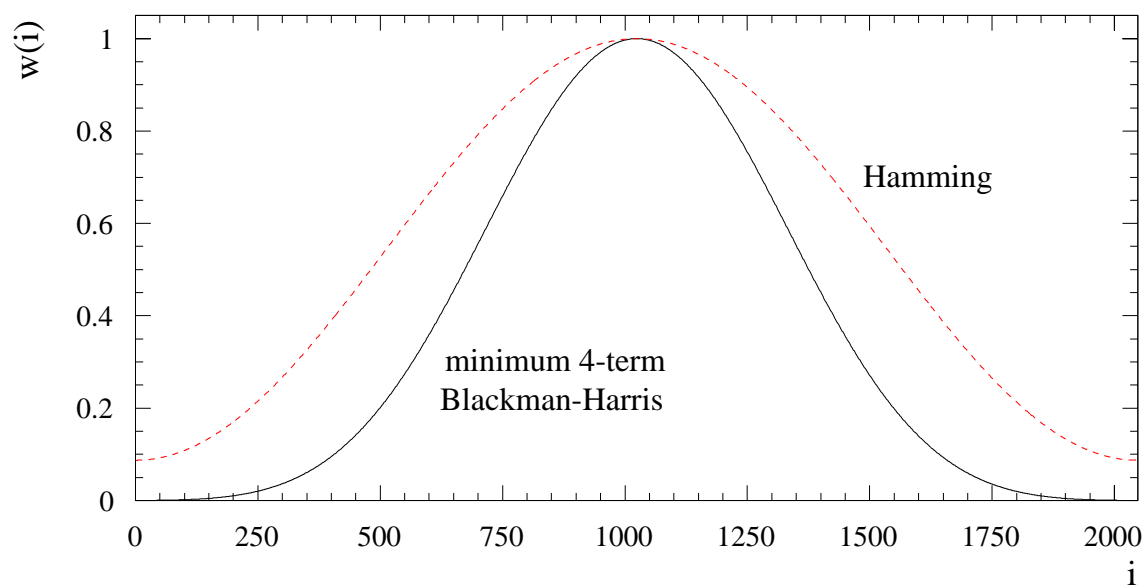


Figure 4.7: Windowing function $w(i)$ for the minimum 4-term Blackman-Harris window and the Hamming window for $N_{\text{data}} = 2048$ points.

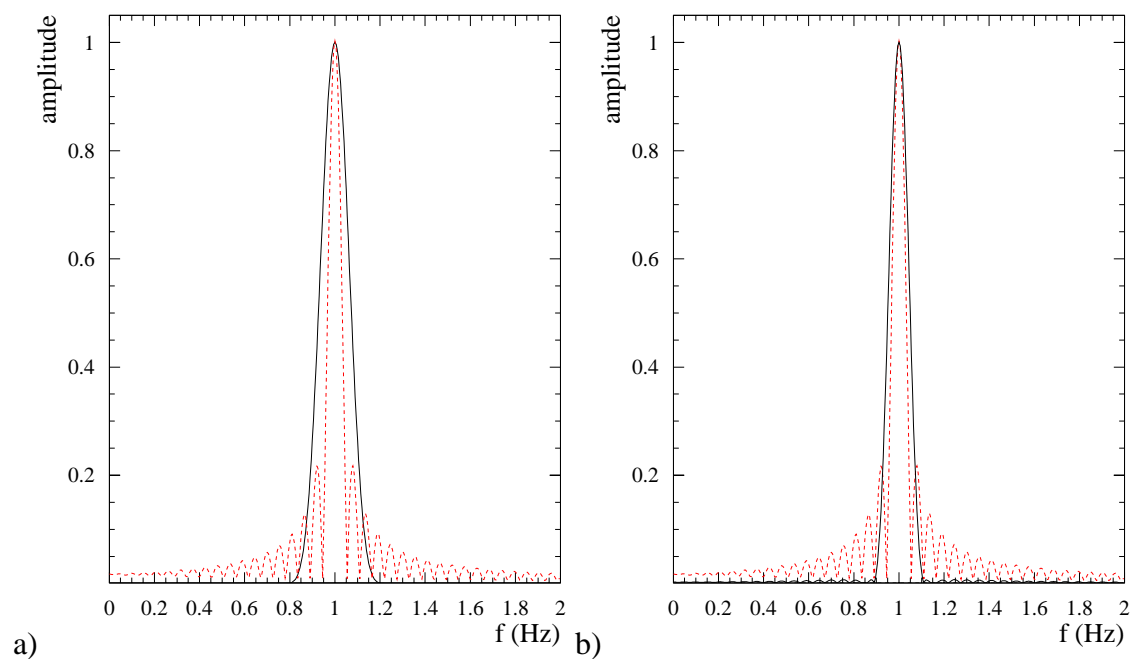


Figure 4.8: Harmonic analysis of a signal of $f = 1$ Hz with the 4-term Blackman-Harris window (a) and with the Hamming window (b) in comparison to the analysis with a rectangular window (dashed line). Sampling frequency is $f_{\text{sampl}} = 112.46$ Hz, $N_{\text{data}} = 2048$. This corresponds to a measurement time of $T = 18.2$ s.

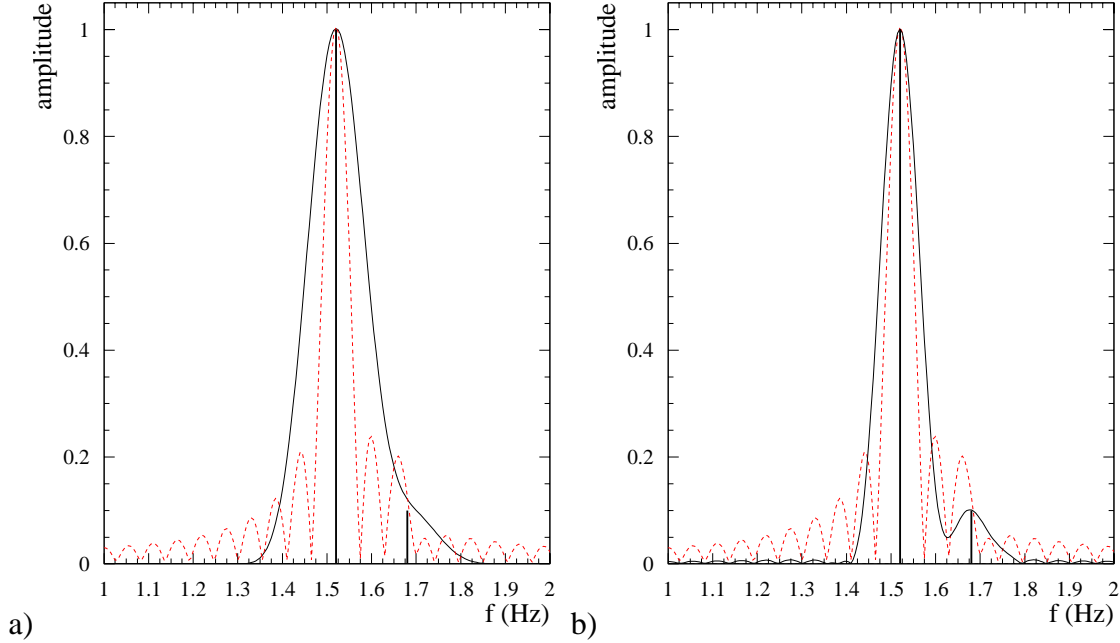


Figure 4.9: Harmonic analysis of two signals of $f_1 = 1.52$ Hz and $f_2 = 1.68$ Hz with amplitudes $A_1 = 1.0$ and $A_2 = 0.1$, respectively (indicated by solid lines). (a) shows the 4-term Blackman-Harris window and (b) the Hamming window in comparison to the analysis with a rectangular window (dashed line). Sampling frequency was $f_{\text{sampl}} = 112.46$ Hz, $N_{\text{data}} = 2048$. The separation between the two signals is impossible for the rectangular and the 4-term Blackman-Harris window while the small signal is clearly visible for the Hamming window.

there of only 0.2%. The Hamming window has the favourable combination of a narrow peak and a sidelobe level which stays below 0.7% of the signal.

The spectral leakage is particularly important for the offset determination when the beam is well centred in one quadrupole magnet under modulation (small signal) and badly centred in another magnet with a nearby modulation frequency (large signal). Since the sidelobe height is proportional to the main lobe, the small signal would get a significant error.

An example for this is shown in Fig. 4.9 for two harmonic signals of $f_1 = 1.52$ Hz and $f_2 = 1.68$ Hz with respective amplitudes of $A_1 = 1.0$ and $A_2 = 0.1$. The smaller signal is absolutely unobservable in the sidelobes of the stronger one for the case of the rectangular window. For the Blackman-Harris window the frequency spacing is also too small and the small signal is not to distinguish from the larger main lobe. For the Hamming window, the smaller signal is clearly visible and the calculated amplitude is $A_1^c = 0.1009$, with an error of less than 1%.

Spacing the excitation frequencies for the offset determination by more than Δf_{min} avoids the problem of crosstalk between simultaneous measurements at neighbouring frequencies. For the Blackman-Harris window, a value of $\Delta f_{\text{min}}^{\text{BH}} = 3.5 \cdot f_{\text{bin}}$ is necessary while for the Hamming window a value of $\Delta f_{\text{min}}^{\text{Ham}} = 2.5 \cdot f_{\text{bin}}$ is sufficient. The smaller frequency spacing possible for the Hamming window has the advantage of fitting more measurement frequencies in the range for the back leg windings where the oscillation should be below about 2 Hz. Table 4.2 gives some examples of the minimal frequency spacing for different parameter sets.

N_{data}	n_{av}	$f_{\text{sampl}}[\text{Hz}]$	$T[\text{s}]$	$f_{\text{bin}}[\text{Hz}]$	$\Delta f_{\text{min}}^{\text{BH}}[\text{Hz}]$	$\Delta f_{\text{min}}^{\text{Ham}}[\text{Hz}]$
4096	200	224.92	18.2	0.0549	0.192	0.137
2048	400	112.46	18.2	0.0549	0.192	0.137
2048	600	74.97	27.3	0.0366	0.128	0.092
2048	800	56.23	36.4	0.0275	0.096	0.069

Table 4.2: Sampling frequency f_{sampl} , measurement time T , bin frequency f_{bin} and minimal frequency spacing for the 4-term Blackman-Harris and Hamming windows for some parameter sets.

Since the orbit is only acquired once a minute, a measurement time around 30 s still gives 2 measurements for every orbit measurement. The frequency resolution is small enough for a dense spacing of the oscillation frequencies for the back leg winding excitation.

Sampling frequencies around 50 Hz have to be used with care since the 50 Hz noise signal can be mirrored into the observation range, perturbing the calculation of the oscillation amplitudes.

4.3.4 Cuts

The signals of the induced beam oscillations have to be detected in the presence of orbit oscillations from other sources, orbit drifts and corrections. The drifts and corrections are particularly annoying since the orbit measurement frequency is very low. So the orbit can change during the measurements and this change is seen with a delay in the orbit acquisition data.

Different cuts have been introduced and studied to improve the quality of the data.

Orbit drifts

A changing orbit during the measurements leads to data points which are off the V-shaped distribution. The orbit corresponds to the position before the orbit change and the amplitude corresponds to the new beam position after the change. These points enter the plot with a wrong abscissa.

These points are rejected by looking at the difference of consecutive orbit positions during the measurements. If this difference is larger than a certain threshold both the measurement before and after the change are discarded. A cut of 100 μm has proven to be effective without a large data reduction.

Especially in the case of orbit bumps for the offset determination, this cut is very important. Comparing the changes in the measured oscillation amplitude with the changes in the orbit revealed that the apparent time of the changes did not coincide. The transfer of the orbit data of the BOM system creates a delay. This effect is compensated in the analysis software by shifting the BOM readings with respect to the amplitude measurements by 1–2 data sets.

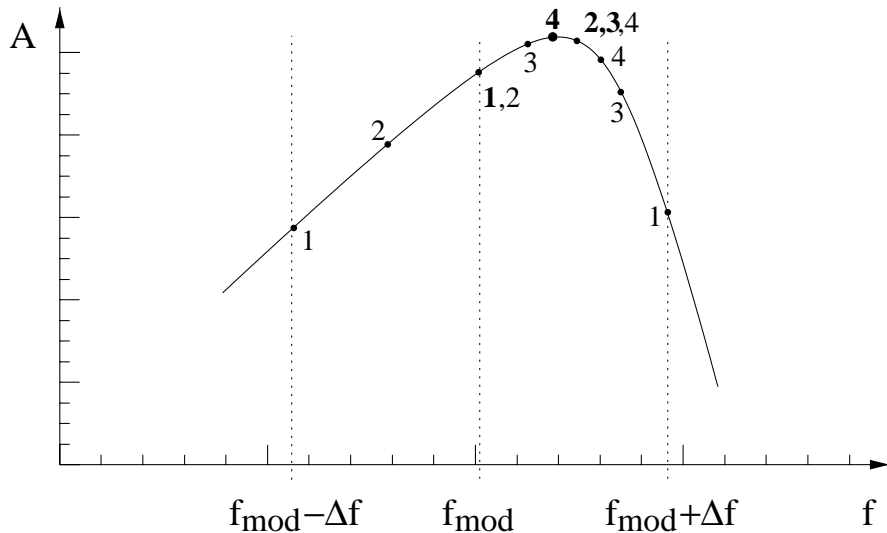


Figure 4.10: The amplitude is scanned around the modulation frequency f_{mod} to find the maximum. In each iteration, the maximum of three points (indicated by a bold number) is taken and the interval is halved, centred around the frequency of maximum amplitude. Four iterations are performed to narrow the frequency uncertainty.

Modulation frequency cut

The signals have to be analysed in the presence of a variety of beam oscillations from other sources with different frequencies. Particularly, when the beam is well centred in the quadrupole under modulation, the noise from other sources dominates the result of the harmonic analysis.

The modulation frequency is stable. The presence of other beam oscillations influences the position of the maximum oscillation amplitude near the modulation frequency. This frequency shift can be used as a criterion for the perturbation by other sources.

For this reason, the harmonic analysis is not only performed at the modulation frequency but a scan is carried out around the modulation frequency to detect the maximum amplitude. The principle is shown in Fig. 4.10. The harmonic analysis is executed in a first iteration at three frequencies: the modulation frequency f_{mod} and two frequencies below and above $f_{\text{mod}} \pm \Delta f$. The frequency where the maximum amplitude occurred is chosen as the centre frequency for the next iteration and the frequency spacing is halved. A number of n iterations defines the position of the maximum with a precision of $\Delta f / 2^{n-1}$.

The parameters chosen for this application were usually $\Delta f = 0.01$ Hz and $n = 4$ iterations. This limits the scanning interval to $f_{\text{mod}} \pm 0.01875$ Hz and the remaining uncertainty in the frequency of the maximum is 0.00125 Hz.

Fig. 4.11 shows an example of the maximum amplitude defined by this method versus the frequency where it was found. For a strong signal, the frequency of the maximum corresponds very well to the excitation frequency. If the amplitude of the induced beam oscillation is small, the peak is often detected at the edges of the interval indicating that this measured amplitude does not originate from the modulation of this quadrupole magnet.

This allows to perform a cut on the frequency interval where the maximum was detected to reduce the influence of beam oscillations from other sources. The cut range

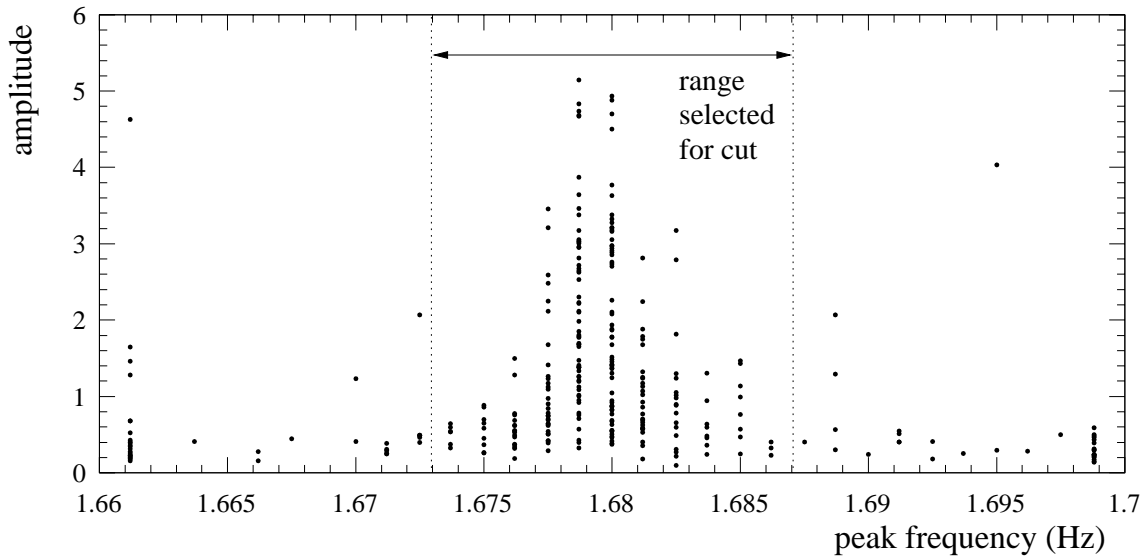


Figure 4.11: Measured amplitude of oscillation as a function of the frequency where the peak was detected. The excitation frequency was 1.68 Hz in this example. Selecting only points in the vicinity of the excitation frequency reduces the influence of parasitic signals.

can be adjusted in the individual case to allow a good compromise between statistics and noise rejection. Satisfying results were usually obtained by cutting out only points at the edges of the scan interval.

Low frequency cut

The closed orbit can change during the measurement time for one data set either due to an orbit drift or an orbit correction. This means that the position in the modulated magnet is not well defined for the measurement. Since most orbit corrections will not only have a local effect at the magnet under modulation, the orbit will change at the location of the couplers, too. This opens the possibility for a cut to sort out these data points.

An orbit correction results in a sudden change of the beam position. The Fourier spectrum of this step function contains predominantly low frequencies. The orbit drifts also happen at a very low frequency time scale. This fact was used to introduce a cut on the sum of the amplitudes in the first three bins above DC of the FFT.

This cut is important since the Fourier spectrum of the step function extends with a significant frequency contribution into the range above $f = 0.72$ Hz used for the modulation by back leg windings. The step caused by the orbit correction can be much bigger than the modulation-induced beam oscillation.

The worst case is evaluated by analysing a signal with the minimum modulation frequency $f = 0.72$ Hz superimposed by a step function. The harmonic analysis using rectangular and Hamming window for a step of 10 for typical data acquisition parameters is shown in Fig. 4.12. The calculated amplitude at the modulation frequency is significantly perturbed. The step gives an additive contribution to the detected signal height, but is also phase dependent. The calculated amplitude for the signal phase where the perturbation was strongest is 1.46, 1.68 and 1.48 for rectangular, Blackman-Harris and Hamming window, respectively.

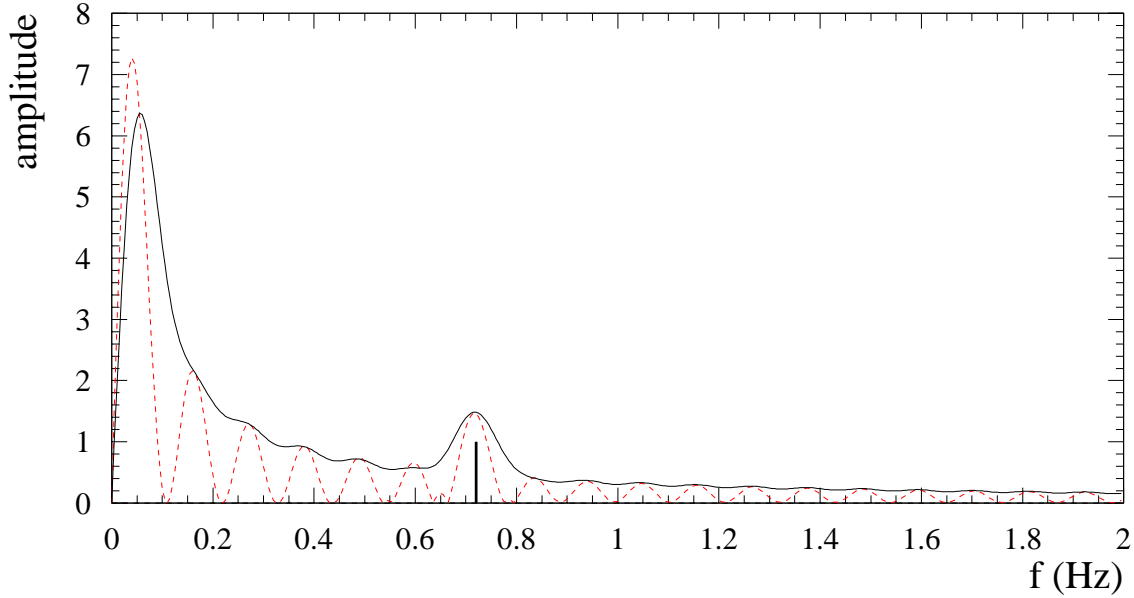


Figure 4.12: Harmonic Analysis of an oscillation of $f = 0.72$ Hz of amplitude $A = 1$ (indicated by solid line) superimposed with a step of 10 in the middle of the data. The phase of the signal was chosen to give the strongest perturbation of the calculated amplitude. The dashed line is the result for a rectangular window, the solid line for a Hamming window ($f_{\text{samp1}} = 112.46$ Hz, $N_{\text{data}} = 2048$).

The sum of the first three bins of the FFT results in 12 in this example. The maximum perturbation of the oscillation signal is inferior to 5% of this sum. A value of 5 for the cut parameter limits the maximum possible absolute error on the calculated amplitude to below 0.25 even for the lowest excitation frequencies.

4.4 Determination of the orbit monitor offsets

The amplitude of the induced orbit oscillation has to be measured for different beam positions inside the quadrupole magnet to determine the offset of a particular beam position monitor. Two different ways can be employed to do so: one can rely on the orbit drifts or apply local closed orbit bumps at the location of the quadrupole to assure different orbit positions.

In both cases, a fit allows the precise determination of the position of the minimum amplitude. The function fitted to the data is

$$A(y) = a \cdot |y - y_0| + A_0 \quad (4.14)$$

where y_0 is the offset of the beam position monitor. The parameter a is the slope depending on the sensitivity function (see Eq. 4.3) and the adjustment of the electronics. In addition to the ideal case of Fig. 4.1, an amplitude offset A_0 is included in the fit to take into account the effect of noise from other sources which on average raises the whole curve.

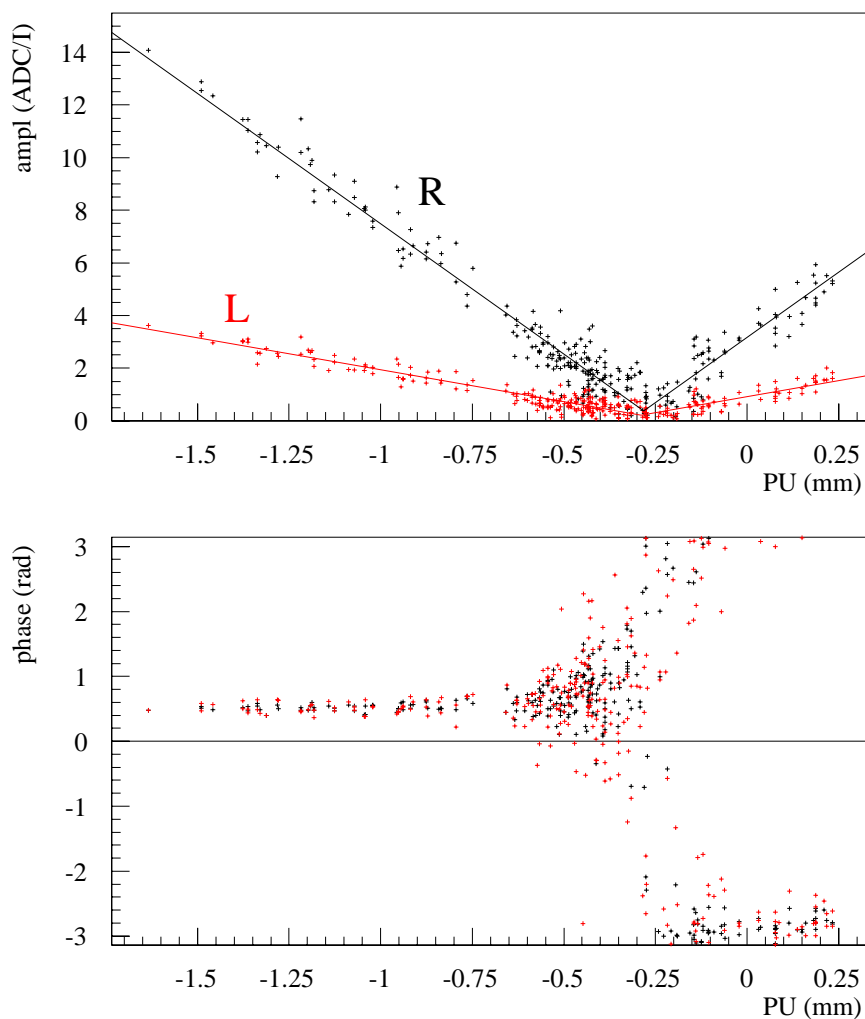


Figure 4.13: Offset determination by natural orbit drifts for the QS0.L2 using electrons. The upper plot shows the measured amplitude, the lower the calculated phase of the oscillation. The measurements of both couplers are shown. The offset in this example was found to be $-282 \pm 5 \mu\text{m}$ (BPCO.QF31.R1), $-289 \pm 7 \mu\text{m}$ (BPCO.QF31.L1). A cut on orbit drifts larger than $50 \mu\text{m}$ was applied.

Nearly all measurements were performed in the vertical plane where the offsets are more important for the orbit quality and particularly polarization. The method is equally applicable for horizontal BPM offsets.

Most of the initial measurements were relying on the strong orbit drifts in the vertical plane. These drifts are very annoying for the operation of LEP but opened the possibility of the offset determination without any additional intervention during physics data taking. The problem and cure of the orbit drifts is dealt with in Chapter 5. Furthermore, it is not possible to apply large closed orbit bumps across the IPs without affecting the luminosity. So the offset determination for the closest magnets to the IP (QS0, QS1) relies on the drifts if no particular operation time is to be used for this.

An example of an offset measurement by natural closed orbit drifts is shown in Fig. 4.13. The plot shows the data taken by the two couplers. The measured oscillation amplitudes for the two couplers are not identical due to their different sensitivity to an

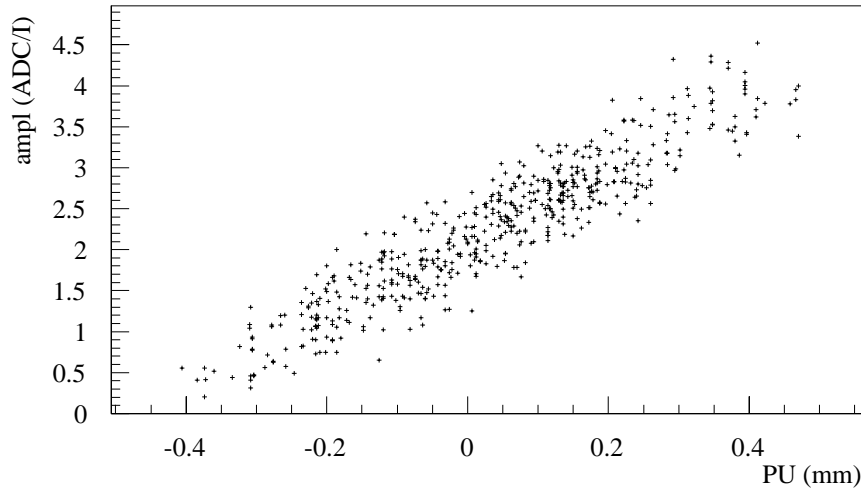


Figure 4.14: Oscillation amplitude for a modulation of QS0.L2 using electrons measured by BPCO.QF31.R1. The range of the orbit drifts did not make the orbit pass the centre of the magnet. A precise determination of the offset is not possible. A less accurate offset value can still be deduced from the measurement. In this example, the offset is smaller than $-300 \mu\text{m}$.

orbit kick at the location of the excited quadrupole (see Eq. 4.3 and Fig. 4.3) and different attenuation of the coupler signals.

The measured oscillation amplitude shows the expected linear dependence on the beam position inside the magnet. The scatter is due to the presence of beam oscillations from other sources which randomly add to the induced oscillation. A second source of scatter is fact that the orbit is only measured once per minute. So the orbit can have moved when the amplitude of the beam oscillation is measured. This effect is reduced by the cut on orbit drifts but a residual error smaller than the cut parameter can remain.

It is impossible to give a precise value of the error of the individual data points. The additional noise is assumed to be statistical and independent of the position inside the magnet. So an error independent of the amplitude is assigned to the points and is scaled to get a value of $\chi^2 = 1$ per degree of freedom in the fit. The long measurement during the physics data taking time results usually in a fit with a high precision. A statistical error below $10 \mu\text{m}$ can be reached.

The lower graph of Fig. 4.13 shows the calculated phase of the oscillation. It can serve as a cross-check of the measurement. The absolute value is not important. It is clearly visible that the phase changes by π when the beam position changes the side of the magnet. The phase is not very well determined close to the centre of the magnet since it is dominated by random signals which do not have a fixed phase relation to the measurement. Hence it cannot give a very precise location of the offset. But it can be helpful for the offset determination by orbit bumps to see whether one has already passed the magnet centre.

The offset determination by the natural orbit drifts has a major disadvantage. It does not guarantee that the change of beam position inside the quadrupole is large enough to cover both sides of the magnet. If the orbit is not well centred it is likely that the orbit remains on one side of the magnet. So the minimum is not reached and a precise determination is impossible. Fig. 4.14 gives an example of this case. The measurement

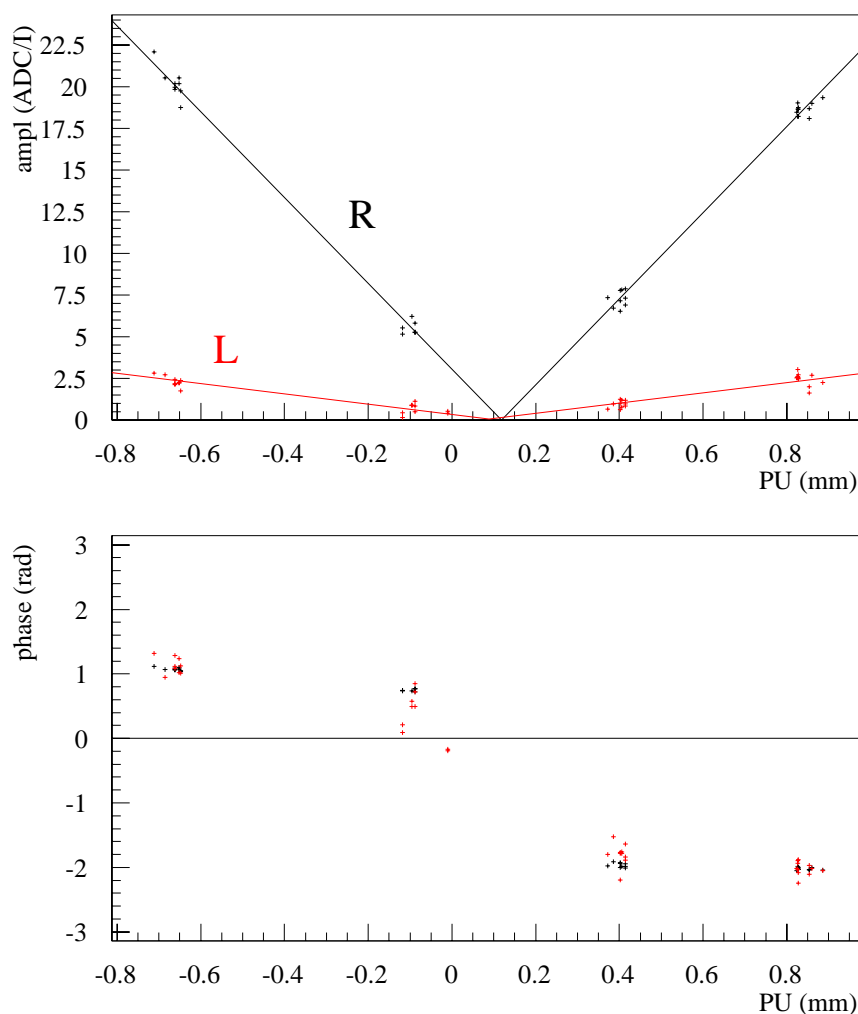


Figure 4.15: Offset determination for QD44.L8 by applying local closed orbit bumps. The offset in this example was measured to be $118 \pm 3 \mu\text{m}$ (BPCO.QF31.R1), $88 \pm 17 \mu\text{m}$ (BPCO.QF31.L1). The larger statistical error for the left coupler is due to its smaller sensitivity. Cuts applied were orbit drifts larger than $50 \mu\text{m}$ and the sum of the low frequency FFT bins smaller than 30.

can still give an indication of the offset when the measured amplitude is larger at a zero BPM reading than at a different position.

The offset determination by drifts fails for a stable orbit when the movements are small like for the horizontal orbit of LEP. Local closed bumps can be applied at the location of the quadrupole under modulation in that case. The bump ensures that the measurement covers both sides of the magnet for a precise offset determination. This strategy also speeds up the measurement significantly. While a measurement using drifts took usually several hours, the bump method can determine the offset in about 15–20 minutes. It allows to perform series measurements in a controlled way. The majority of the offset measurements at LEP were made using local orbit bumps.

The range of the orbit variation inside the magnet can be increased and the larger signal is also visible in the case of larger noise. The orbit bumps are created using four correction coils to obtain a bump with zero angle in the centre of the quadrupole. Fig. 4.15 shows an example of the offset determination using a local closed orbit bump.

While the closed orbit bumps across the interaction point are problematic, bumps in the arcs were used during physics data taking for the offset determination without significantly affecting the luminosity. Only when several bumps of amplitudes of about 1 mm were used simultaneously, a slight reduction in luminosity due to the dispersion generated by the bump was observed.

4.4.1 The superconducting low-beta insertion quadrupoles

The quadrupole magnets closest to the interaction points (QS0) are superconducting magnets, necessary to reach the high gradient to squeeze the beam size at the collision point. The magnetic coils are in a cryostat and cooled down to liquid Helium temperature. The position of the coils with respect to outside fiducial marks is only measured at room temperature. A contraction of the support of the coils can lead to a displacement of the coils when the magnet is cooled down.

The superconducting quadrupoles installed until 1993 (MQC) were subsequently replaced by a stronger type (MQCC) to fulfil the requirements for the energy upgrade for LEP II. The exchange took place during shut down 1993/94 at IP 2 and IP 8, 1994/95 at IP 6, and finally 1995/96 at IP 4.

The beam position monitor is attached to the superconducting magnets, 45 cm away from the end of the magnet. It is equipped with a wide band BOM electronics. The gain usually changes during the physics data taking from a 0 dB to 10 dB setting when the bunch currents fall below a certain limit. The offsets measured for the two gain settings were different in some cases by more than $200 \mu\text{m}$. The calibration procedure of the BPM electronics is responsible for the different offsets for the different gain settings. For a given gain, no current dependence of the offset is obvious since the data points for a varying bunch current lie on the same curve.

The offsets for the two particle types showed usually also differences of the same magnitude. The first part of the processing electronics for electron and positron signals is not identical and can cause this effect.

The distribution of the BPM offsets for the old (MQC) and new (MQCC) quadrupole type is shown in Fig. 4.16. The results for different particle types and gain settings are treated as individual offsets. For the measurements in 1993 [Beu93, Sch93], this was not possible since the gain dependence was not known at that time and no differentiation for the gain setting was made.

It is clearly visible that the new generation of superconducting quadrupoles (MQCC) for LEP II has smaller offsets than the previous type. The offsets for the MQCC type are all smaller than -1 mm while some of the offsets for the older MQC type were nearly -2 mm . The mean and rms of the distributions are $(-1.18 \pm 0.66) \text{ mm}$ for the MQC and $(-0.58 \pm 0.31) \text{ mm}$ for the MQCC type. This difference indicates that the large offsets are mainly of mechanical nature since the BPM electronics is not different for the two types. The reason for the large offsets is probably the above mentioned contraction of some part of the magnet when it is cooled down. Both types show systematic negative offsets, i.e. the magnet axis is lower than the pickup centre.

The long-term reproducibility of the measured offsets for the superconducting magnets was already studied in [Rei94] and was found to be of $75 \mu\text{m}$. This includes effects from the statistical error, beam angle in the quadrupole and re-calibration of the BPM electronics.

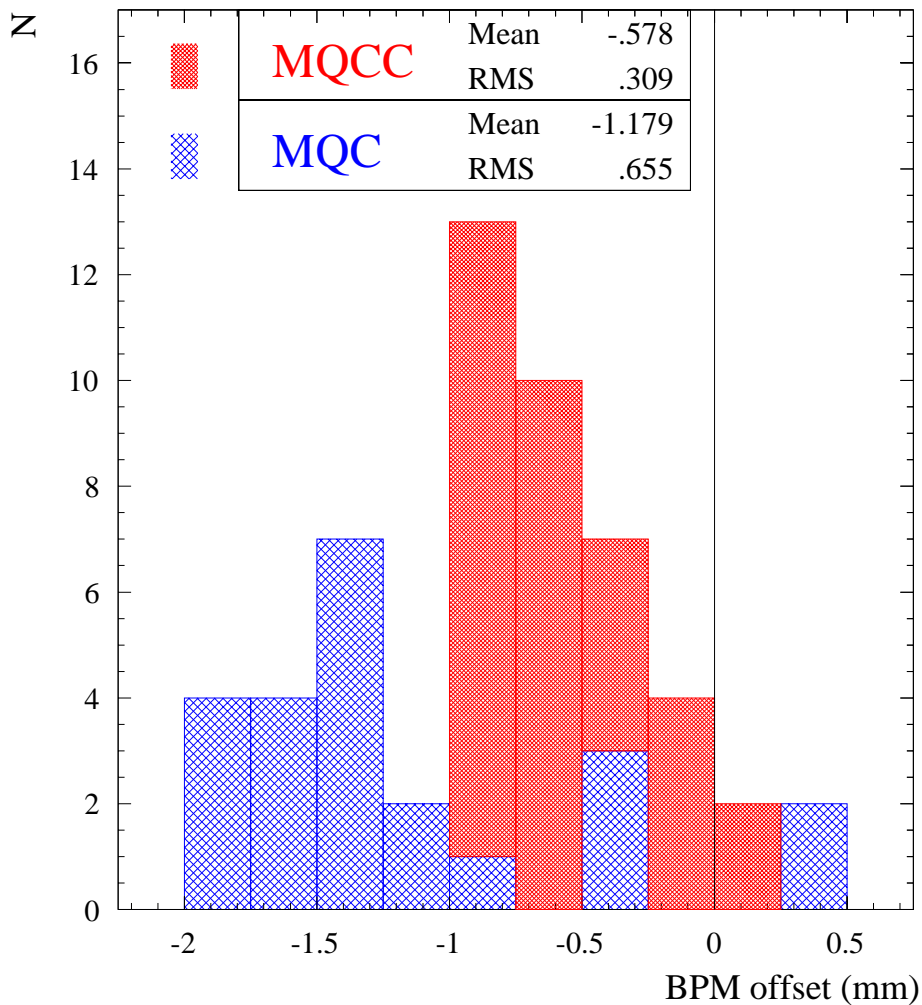


Figure 4.16: Distribution of the BPM offsets for the superconducting quadrupole magnets. The offsets for different gain settings and particle type are treated independently. The offsets for the first generation of the superconducting quadrupole magnets for LEP (MQC type) show large offsets of up to -2 mm. Their replacements for LEP II (MQCC type) have offsets only up to -1 mm.

4.4.2 Normal conducting magnets with Wide Band BOM

The measurements of wide band BPM offsets were mainly performed at the QS1 magnets. Orbit movements in the other magnets were often too small and bumps across the interaction point were not used during physics data taking. Some other offsets were measured in the non-experimental straight sections or during dedicated machine time.

The QS1 is a doublet of two 2 m long magnets (MQA type) spaced by 50 cm. The BPM is on one exterior side of the magnets at a distance of 17 cm. All other normal conducting magnets are single magnets with the BPM at the same distance. The bigger length of the QS1 doublet could lead to a larger error caused by the beam passing through the magnet with a non-zero angle.

Fig. 4.17 shows the distribution of the measured offsets for magnets where the BPM has a wide band electronics. The difference between the offsets for the QS1 doublet and other magnets is small. The width of the distributions are nearly identical with 354 and

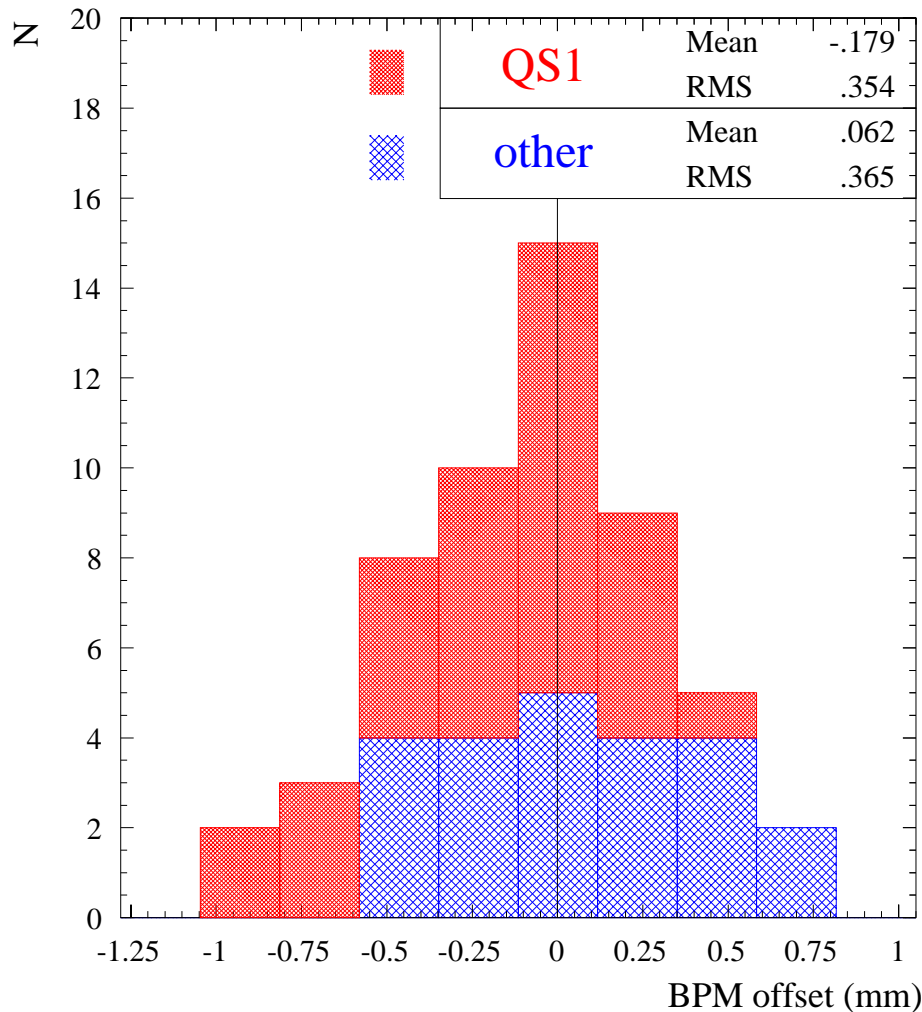


Figure 4.17: Distribution of the offsets in the vertical plane for BPMs with wide band electronics at normal conducting quadrupole magnets. The offsets for the QS1 doublets are shown separately. The distribution for the QS1 does not differ significantly from the one for other magnets with a wide band type BPM.

$365 \mu\text{m}$. The mean values of $-179 \mu\text{m}$ and $62 \mu\text{m}$ do not differ significantly from zero compared to the width. Combining both distributions results in a width of $378 \mu\text{m}$ with a mean of $-76 \mu\text{m}$.

The offsets for the normal conducting magnets are significantly smaller than for the QS0 magnets with the same BPM electronics, where the mean value is $-578 \mu\text{m}$ for the presently installed magnets. The offsets for the superconducting magnets must be predominantly of mechanical origin.

4.4.3 Magnets with Narrow Band BOM

Most of the beam position monitors are equipped with narrow band electronics. Until end of 1996, 448 of the 504 pickups and from 1997 412 out of 500 were of this type. In particular, all the BPMs in the arcs and dispersion suppressors, where the vertical orbit is of big importance for the polarization, have narrow band electronics.

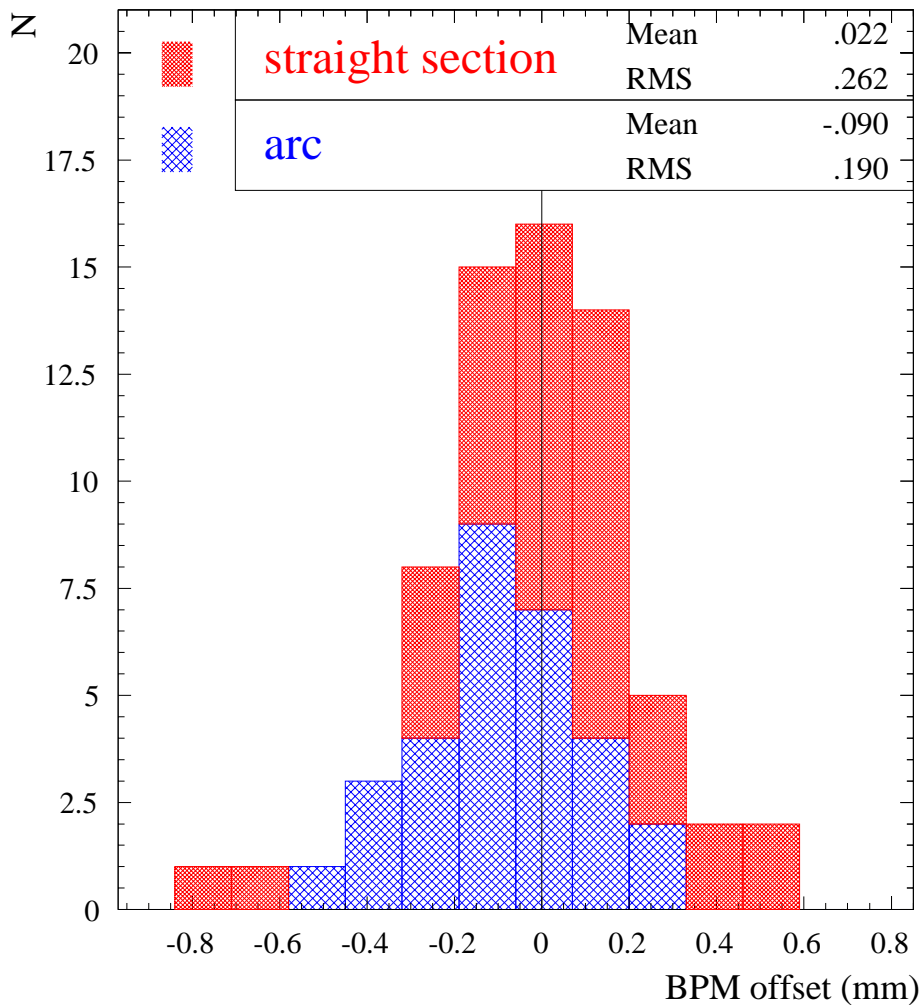


Figure 4.18: Distribution of the BPM offsets in the vertical plane in the straight sections and the arc around IP 8 measured until the end of 1996. The offsets measured for different particle types are treated as separate measurements.

First measurements were performed in the straight sections. The quadrupole magnets in the arc and dispersion suppressor around IP 8 were equipped with back leg windings in 1995 and measurements were done there mainly using local closed orbit bumps. The results of these offset determinations are shown in Fig. 4.18.

The offsets are in general smaller than for the wide band type BPM electronics. The differences between the offsets for the different particle types were also significantly smaller and typically below $50 \mu\text{m}$. The width of the distribution for BPMs in the arc of $190 \mu\text{m}$ is about half as big as for the wide band type. The distribution of the offsets for BPMs in the straight section is slightly larger with $262 \mu\text{m}$. The mean value of the distributions do not differ significantly from zero. The distribution of all measured narrow band BPM offsets combined has a mean of $-28 \mu\text{m}$ with a width of $240 \mu\text{m}$ rms.

The small difference between the measured offsets in the arc and the straight sections could originate from the limited statistics. A contribution to the larger width for BPMs in the straight section could come from an error due to a beam passing the quadrupole with an angle.

elements	displacement x and y	tilt around \vec{e}_s	relative field error
bending dipole	140 μm	240 μrad	7.0 $\cdot 10^{-4}$ (B2DF) 6.0 $\cdot 10^{-4}$ (BIDF) 2.2 $\cdot 10^{-4}$ (B2WDF)
quadrupole	150 μm	240 μrad	3.0 $\cdot 10^{-4}$ (MQDF) 1.0 $\cdot 10^{-4}$ (MQADF) 2.0 $\cdot 10^{-4}$ (MQCDF)
sextupole	-	-	0.5 $\cdot 10^{-4}$

Table 4.3: The rms values of the misalignments and field errors used to simulate an imperfect LEP machine.

The length of the FODO cell in the arcs is 79 m and this is also the distance between two BPMs there. Typical beam angles in the arc are of the order of 10 μrad . The distance from the BPM to the centre of the arc quadrupoles (MQ type) is 0.97 m. So the error that can be caused by a beam passing with an angle through the magnet is of the order of 10 μm .

The distance between BPMs in the straight sections is of the order of 25 m. For most of the straight section quadrupoles (MQA) the distance to the BPM is 1.17 m. Assuming identical rms orbit excursions, typical angles are about 30 μrad and an offset error up to about 30 μm could result from this.

The measured BPM offsets were introduced in the BPM orbit acquisition software. Whenever a set of orbit data is acquired, the BPM readings are corrected for the offsets. The resulting orbit data has the centres of the quadrupole magnets as a reference.

The large BPM offsets for the superconducting quadrupoles are important for LEP operation. An empirically found[†] *Golden Orbit* passes well centred through the QS0 magnets [Rei94]. The smaller offsets for the narrow band BPM type, which presents the majority of the LEP ring, is of less importance for the luminosity operation where the vertical orbit excursions are typically about 500 μm . They are, though, of special interest for polarization studies and energy calibration where the orbit is carefully corrected to excursions of about 250 μm .

4.4.4 Impacts of BPM offsets on transverse spin polarization

It was pointed out in Section 2.4 and 3.3 that the increase of the polarization level by Harmonic Spin Matching depends critically on the precision of the orbit measurements and the alignment. The study shown in this section demonstrates in particular the dependence on the BPM offsets.

The polarization calculations were performed by MAD [Gro90] for a LEP machine with realistic misalignments and magnet imperfections. Gaussian distributions of randomly distributed errors cut off at 2.5σ were assigned to the different groups of elements (quadrupoles, bending magnets, etc.). The imperfections used are given in Table 4.3. The

[†] before the measured BPM offsets were introduced

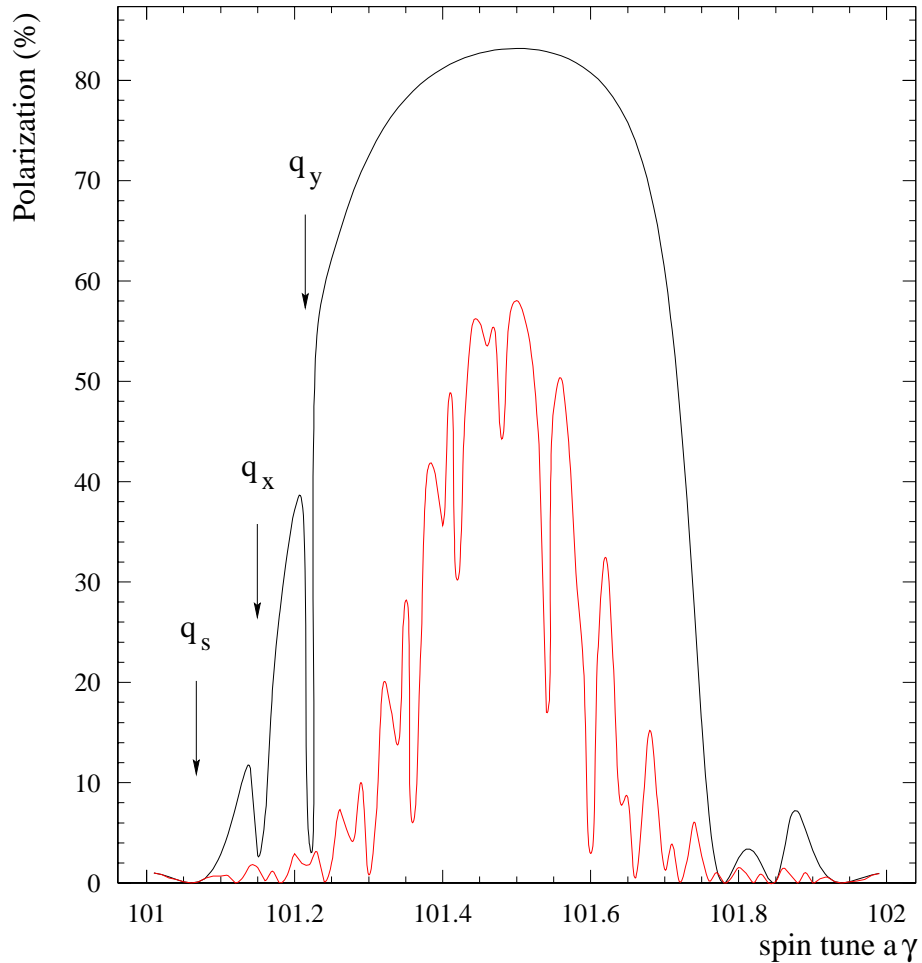


Figure 4.19: Polarization level as a function of the spin tune at an energy near 44.7 GeV. The solid line is the result of the linear calculation by SITF for one random set of misalignments. The linear resonances of the orbital tunes are clearly visible. The settings in this example were $q_x = 0.1534$, $q_y = 0.2207$ and $q_s = 0.0605$. In higher order calculation (dashed curve), the degree of polarization is also reduced by higher order resonances for spin tunes which meet the resonance condition of Eq. 2.38.

beam position monitors were misaligned relative to the centre of the quadrupole magnets with different rms values.

The polarization level is calculated with the SITF module implemented in MAD. SITF is a part of the simulation code SITROS [Kew83, Bög94] and based on the theory by Chao [Cha81, Cha82]. The closed spin solution $\vec{n}_0(s)$ and the spin-orbit coupling $\vec{d}(s)$ are calculated from the closed orbit using a matrix formalism. The polarization level is computed from Eq. 2.39. The SITF calculation takes into account the linear resonances only. An example is shown in Fig. 4.19. The prediction of the polarization level is in general too optimistic since higher order resonances are important already at LEP I and become even stronger for higher energies. Nevertheless, the strength of the higher order sideband resonances scales with the strength of the linear ones. In the scope of this analysis, it is only intended to give a qualitative view of the effects of the BPM offsets and not to predict the absolute polarization level at a given energy.

A precise prediction for the actual LEP is also difficult since the harmonic contents of the vertical orbit can be significantly different for identical rms values [Ass93]. This results in a large spread in the degree of polarization. A set of ten different random seeds was used in the simulations to generate different patterns of imperfections for each rms BPM misalignment for otherwise identical machine parameters (tunes, spin tune, rms misalignment, rms orbit, etc.). The degree of polarization was averaged in the spin tune interval $[k+0.45 \dots k+0.55]$. The mean value of the ten random seeds and the spread were computed for each set. This average polarization is not meant to predict the actual level at LEP for a given energy but represents well the dependence on the BPM misalignment.

The computation of the spin precession Fourier components c_k of the closed orbit for the real LEP machine is limited by the sampling. The orbit is known only at the locations of the beam position monitors. Only the BPMs in the bending regions contribute to the Fourier coefficients. There are 112 BPMs in the dispersion suppressor of LEP and 240 in the arcs resulting in a total of 352 sampling points. In addition to the limited sampling, it is also irregular. In the arcs, 6 bending magnets are between two BPMs, while there are 2-4 in the dispersion suppressor. This irregular sampling introduces an error in the calculation of the Fourier components.

In the MAD simulation, the Fourier components can be calculated more precisely. The orbit is sampled at every bending magnet, so 1696 points are used for the Fourier analysis. The sampling in the spin precession frame is regular except for the 32 weak bending magnets which have only one tenth of the bending of the regular dipoles and contribute only 0.2% to the overall bending. Their influence can thus be neglected.

This Fourier component computation with the more precise sampling is used as a reference for the calculation using the BPM data. It can be assumed that the polarization level after correction of the Fourier components by deterministic Harmonic Spin Matching corresponds to the highest achievable level for the simulated machine with that set of misalignment and tunes. Thus this optimum case of deterministic HSM has the same result as the best Fourier compensation by empirical Harmonic Spin Matching.

The effect of the sampling became first obvious when the Fourier components of the HSM compensation bumps were analysed with the different samplings. Two different sets of HSM bumps are existing for the compensation of the Fourier components close to a spin tune of $\nu = 101.5$. While one set is in the dispersion suppressor, the other set is in the arc. Both bump sets were analysed in an ideal LEP without any misalignments by the precise Fourier analysis with sampling at every bending magnet and normalised to an Fourier amplitude of $10 \mu\text{m}$. The analysis taking the BPM readings (see Table 4.4) gave results different from $10 \mu\text{m}$ and dependent on the set of bumps. This shows that the result of the BPM data analysis depends on the different sampling in the arc and the dispersion suppressor. The result also depends on the individual harmonic.

Since the Fourier analysis in the case of the real LEP can only be performed by the BPM data, a scaling factor was introduced to approximate the results of the more detailed analysis. According to the above result the factor depends on the location of the orbit bump and is different for arc and dispersion suppressor. The dispersion suppressor contains only 12% of the total bending of LEP. So the arc has the main contribution to the Fourier sum. For this reason, the factor found for the arc is used as a general factor for the analysis.

The factor was computed for different closed orbit bumps over four adjacent orbit correction coils in the arcs. Only values with Fourier amplitude of the BPM analysis

HSM bump set	a_{101} [10 μm]	b_{101} [10 μm]	a_{102} [10 μm]	b_{102} [10 μm]
arc	1.73	1.73	1.76	1.75
disp. suppressor	1.29	1.30	1.39	1.21

HSM bump set	a_{125} [10 μm]	b_{125} [10 μm]	a_{126} [10 μm]	b_{126} [10 μm]
disp. suppressor	1.36	1.36	1.43	1.29

Table 4.4: Analysis of the Fourier components of HSM compensation bumps with sampling at the BPMs. The bumps were scaled to result in a normalised amplitude of 10 μm in the precise Fourier analysis with sampling at every bending magnet.

larger than 5 μm were considered for the calculation of the factor. The factor at a spin tune of 125 and 126 which is relevant for the analysis at 55 GeV had values between 1.9 and 2.3 for the different bumps. The value of 2.1 was used in the further simulations.

For each different random set, the simulation was performed in the following steps:

- assign the misalignments and field errors to the elements
- switch off the sextupoles
- correct the orbit in both planes once to $x_{\text{rms}} = 0.4 \text{ mm}$ and $y_{\text{rms}} = \text{min.}$ using MICADO
- switch on the sextupoles
- correct the orbit in both planes to $x_{\text{rms}} = 0.4 \text{ mm}$ and $y_{\text{rms}} = \text{min.}$ using MICADO
- match the values k_{QD} and k_{QF} to obtain the desired values of the tunes Q_x and Q_y
- adjust the RF cavity voltage to obtain the desired synchrotron tune Q_s
- calculate the polarization level by SITF
- calculate Fourier harmonics from both BPM data and more precise sampling
- scale the BPM Fourier amplitudes from BPM data
- apply HSM compensation bumps
- recalculate the polarization level by SITF
- recalculate Fourier harmonics from both BPM data and more precise sampling

The orbit correction without sextupoles is performed to avoid problems in the correction algorithm due to large orbit amplitudes in the sextupoles which lead to strong orbit distortions.

The size of the BPM offsets has an immediate influence on the quality of the orbit correction. The dependence of the remaining vertical rms orbit excursion after correction is shown in Fig. 4.20. The quality of the orbit correction deteriorates with larger BPM offsets. The effect is less strong for smaller offsets since the orbit correction quality is limited in that case mainly by the misalignment and the number of orbit correctors.

The spread in the polarization level for the individual random sets of misalignment with identical rms value is large. For this reason, the same random seeds for the misalignment were used for the simulations with different size of the BPM misalignment relative to the quadrupole magnets. The different seeds then show the same functional behaviour in dependence of the BPM misalignment.

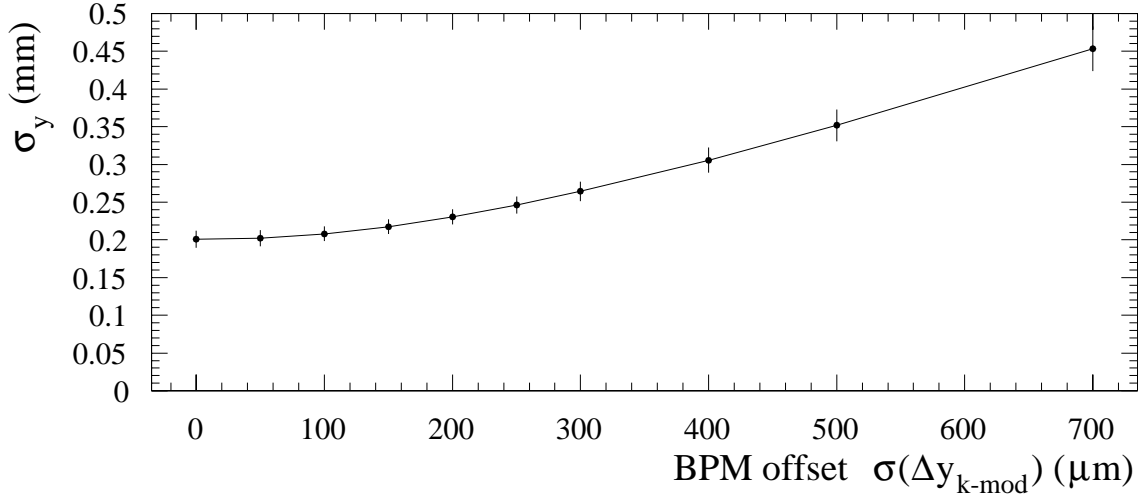


Figure 4.20: Residual vertical orbit excursion σ_y after correction as a function of the BPM offsets. Each point corresponds to the mean value and spread of ten different random seeds for the misalignments.

The result for the simulations with the $90/60^\circ$ phase advance optics for a spin tune near $\nu = 125.5$, 55 GeV, are shown in Fig. 4.21. Each point represents the mean value of ten different random seeds. The values are normalised to the mean value of the polarization level obtained by HSM using the precise Fourier analysis. This value is a polarization level of 64% in the linear SITF calculations.

The mean polarization value before the application of Harmonic Spin Matching depends only very slightly on the BPM offsets. A level of 20% of the optimum polarization level is reached for small offsets. The decrease with increasing offset can be explained by the slightly worse orbit correction resulting in a higher σ_y . So the average orbit and spin kicks are higher and lead to a stronger depolarization.

The polarization level after application of the Harmonic Spin Matching shows a much stronger dependence on the offsets. For offsets smaller than $150 \mu\text{m}$, polarization values above 50% of the optimum level are reached. The HSM more than doubles the polarization. For larger BPM offset this gain becomes smaller, and for values of $\sigma_y > 400 \mu\text{m}$ the HSM even decreases the degree of polarization. This implies that the error introduced in the Fourier analysis by the BPM offsets are larger than the relevant Fourier amplitudes before HSM.

The saturation of the polarization level at about 50% of the optimum value for offsets smaller than $\sigma(\Delta y_{k\text{-mod}}) = 150 \mu\text{m}$ can be explained by the misalignment of the quadrupole magnets themselves. As explained in Section 2.4, the error of the Fourier amplitudes of the closed orbit depends on the measurement error with respect to an ideal plane. Hence, both the offset of the BPM relative to the quadrupole and the misalignment of the magnet contribute equally to this error. The alignment error of $\sigma(\Delta y_{\text{quad}}) = 150 \mu\text{m}$ is the predominant source when the BPM offsets are smaller than this.

The results of the measurements of the BPM offsets in the arc around IP 8 (see Section 4.4.3) showed an rms value of $\sigma(\Delta y_{k\text{-mod}}) = 190 \mu\text{m}$. The corresponding polarization level for this offsets is slightly above 40% of the optimum value. A decrease of the offsets by k-modulation measurements could bring down the value of $\sigma(\Delta y_{k\text{-mod}})$ to

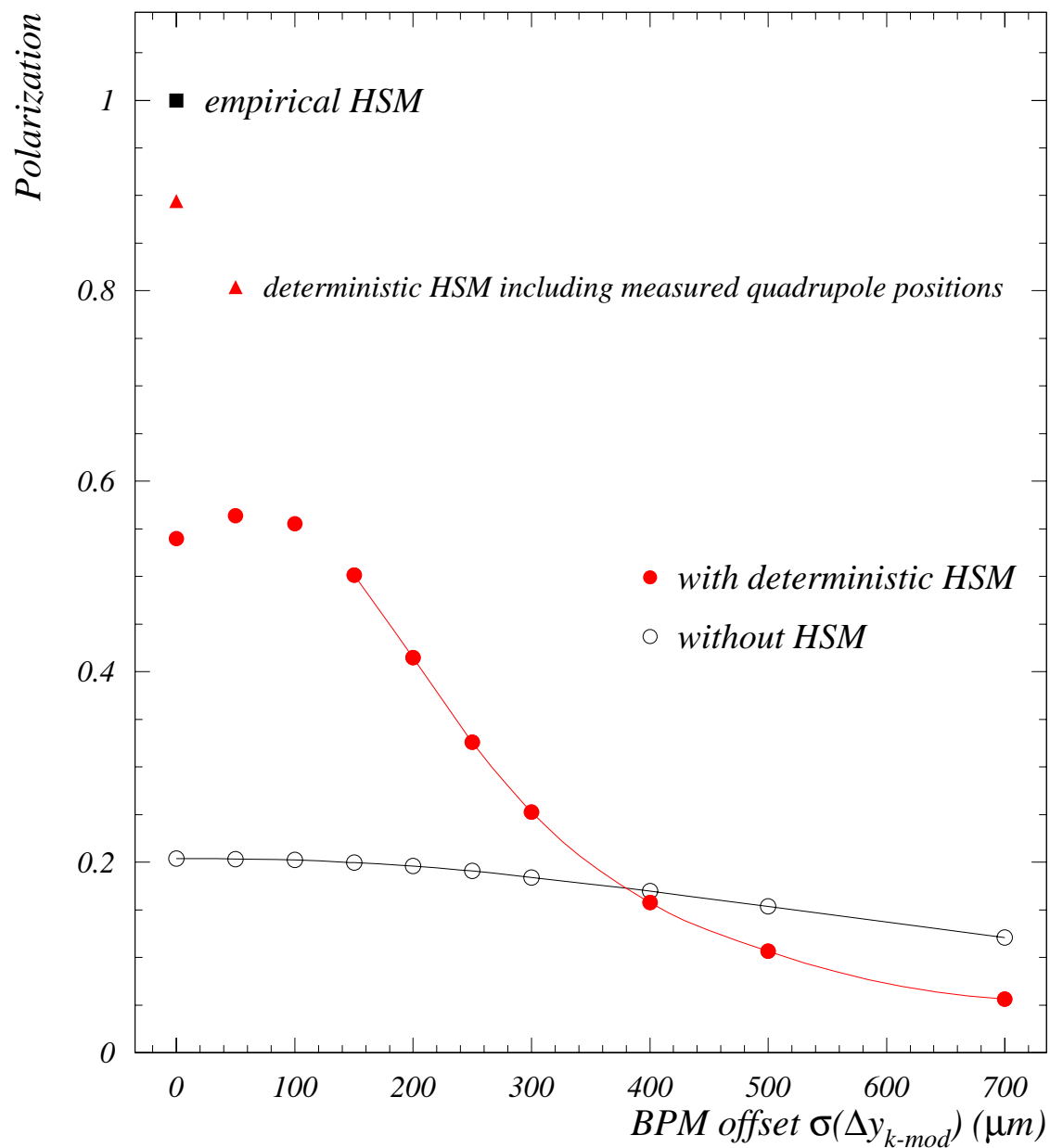


Figure 4.21: Relative polarization in dependence of the BPM offsets relative to the quadrupole magnets. The values are normalised to the optimum polarization level for empirical HSM (which corresponds to the level obtained by deterministic HSM using the precise Fourier analysis sampled at every bending magnet).

below $50 \mu\text{m}$. This would improve the quality of the deterministic HSM and increase the degree of polarization to about 56% of the optimum value.

An further gain in the polarization level can be obtained through the knowledge of the quadrupole misalignment. The residual vertical quadrupole misalignment at LEP is about $\sigma(\Delta y_{\text{quad}}) = 150 \mu\text{m}$. But the precision of the measurement between adjacent quadrupole magnets is of the order of $40 \mu\text{m}$. It would take too much time to realign the magnets to this precision so only the magnets with the largest misalignment from the reference polynomial are realigned. But the position of the magnets is known with a better precision than the actual remaining misalignment. This additional information can be used to improve the knowledge of the BPM positions.

In the MAD/SITF calculations this was simulated by misaligning the magnets as before since this real misalignment remains unchanged. Different from the previous simulations the BPMs were aligned relative to the ideal plane with a given rms value of $\sigma(\Delta y_{\text{BPM}})$ with the assumption of $\sigma^2(\Delta y_{\text{BPM}}) = \sigma^2(\Delta y_{\text{quad}}) + \sigma^2(\Delta y_{\text{k-mod}})$. The orbit was corrected relative to these BPM positions. The results for an uncertainty of the misalignment of $\sigma(\Delta y_{\text{quad}}) = 50 \mu\text{m}$ for $\sigma(\Delta y_{\text{k-mod}}) = 0 \mu\text{m}$ and $50 \mu\text{m}$ are also plotted in Fig. 4.21. The degree of polarization does not show the saturation for small BPM offsets any more. Values of 90 and 80% of the optimum level were reached, respectively.

The study shows that the measurements of the BPM offsets helps to increase the level of polarization which can be reached by deterministic Harmonic Spin Matching. The Fourier analysis becomes more precise and allows a better compensation of the depolarizing Fourier harmonics of the closed orbit. This is mainly important for the energy calibration by resonant depolarization at higher energies where the polarization level is low. Better deterministic HSM increases the probability to obtain a measurable degree of polarization for further empirical optimisation. In addition, it allows to restrict the scanning range of the four-dimensional parameter space for the empirical HSM to smaller volume since the uncertainty of the calculated Fourier harmonics of the orbit is smaller.

After these results the decision was taken to equip during the shutdown 1996/97 all the remaining quadrupole magnets with a BPM attached with a back leg winding. An automatic procedure was developed for the measurements using local closed orbit bumps. During the LEP running period 1997, most of the BPM offsets in the arcs and dispersion suppressors were measured. The rms value of the offsets measured of $\sigma(\Delta y_{\text{k-mod}}) = 270 \mu\text{m}$ was bigger than expected from the results in the arc around IP 8. The impact on the polarization for different beam optics used in 1997 and the measurements are described in detail in a separate work [Son98].

4.5 Beta-function measurement

In addition to the offset determination and improvements of closed orbit and polarization level, one can profit from the installed hardware for the k-modulation to gain additional knowledge about the beta function in the quadrupole magnets.

It was pointed out in Section 2.2 that the average beta function β_Q in a quadrupole magnet can be measured when the quadrupole strength is changed by a known amount Δk . Rearranging Eq. 2.24 leads to

$$\beta_Q \simeq -\frac{4\pi}{\Delta k L} \Delta Q \quad (4.15)$$

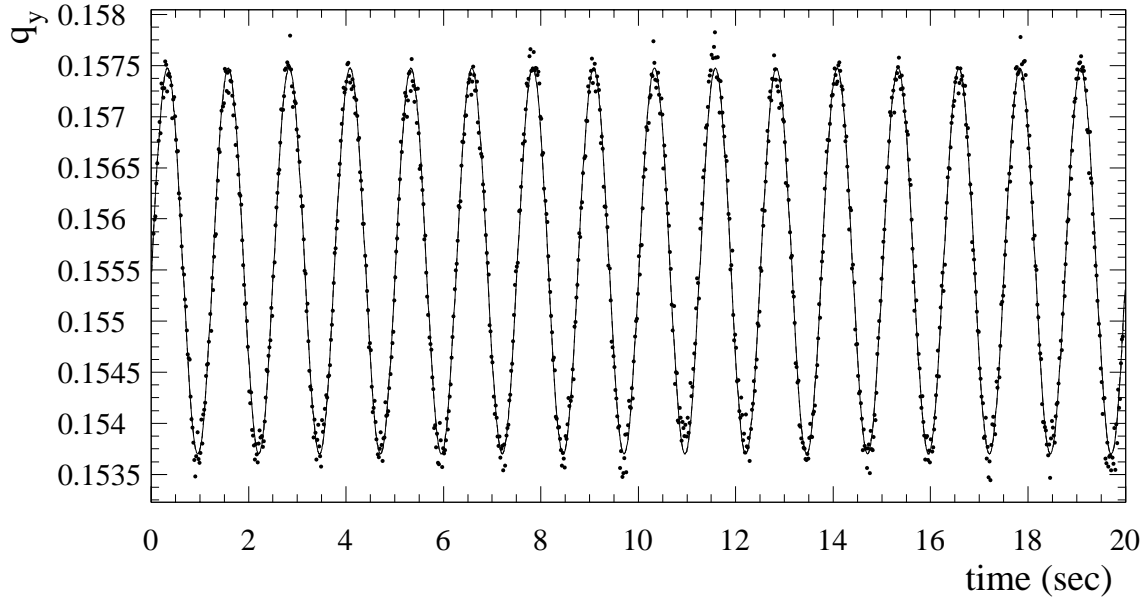


Figure 4.22: Tune variation due to excitation of the back leg winding of QS12.L8 at maximum amplitude ($I_{p-p} = 11.9$ A). The harmonic tune variation is clearly visible and the amplitude can be obtained from a fit.

where ΔQ is the measured betatron tune change. The error on β_Q depends both on the precision with which Δk is known and ΔQ can be measured. It was studied if this method can be used with a sufficient precision with the k-modulation hardware at LEP.

The tune measurement at LEP is performed by the Q-meter which is described f.i. in [Buu92]. The PLL-mode (Phase-Locked Loop) is used for a continuous measurement. The tune changes by the modulation of the quadrupole strength are of the order of a few 10^{-3} . The noise level of the Q-meter was analysed without back leg excitation and found to be of the order of about $1.3 \cdot 10^{-4}$.

The tune modulation by the excitation of the back leg winding is clearly visible in the Q-meter measurement. Fig. 4.22 shows an example of the tune changes due to a harmonic excitation with a frequency $f = 0.8$ Hz of the magnet QL12.L8 with a current of $I_{p-p} = 11.9$ A during a LEP fill at 86 GeV for the $108/90^\circ$ phase advance optics. The quadrupole strength is $k = -0.02347 \text{ m}^{-2}$ for this magnet and the current in the main winding was 180.8 A. The function of the form

$$Q = Q_0 + \Delta Q \sin(\omega t + \phi_0) \quad (4.16)$$

is fitted to the tune values. A single error of $1.3 \cdot 10^{-4}$ is attributed to the measured points. The fit results in a value of $\Delta Q = (1.887 \pm 0.006) \cdot 10^{-3}$ with a relative error of 0.3% and a $\chi^2/\text{dof} = 1.04$. For magnets where the beta function and hence the tune modulation are smaller, the relative error of the tune change will remain below a few percent. The tune measurement provides the required accuracy.

The problem remains in the determination of the exact quadrupole strength change Δk . For the offset determination this is not important since it is a minimum measurement. The hysteresis of the magnets makes it impossible to deduce the Δk directly with high precision from the applied current change ΔI . When a small loop at a certain point of

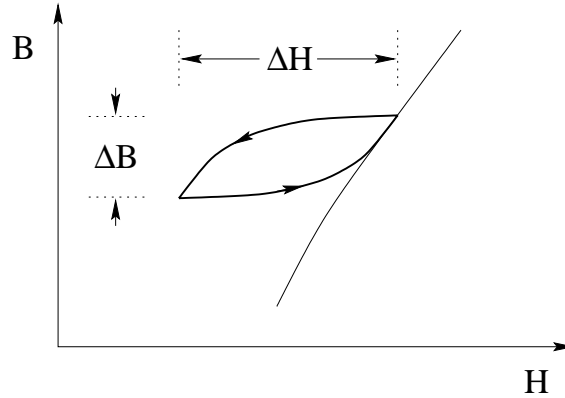


Figure 4.23: Field change due to a small variation of the excitation current.

	QS12.L8	QS12.R8	theor.
β_{Q_x} [m]	58	45	41.0
β_{Q_y} [m]	114	91	102.5

Table 4.5: Comparison of measured beta function (neglecting effect of minor hysteresis loop) with the theoretical average value.

the hysteresis cycle of the magnet is performed (see Fig. 4.23), the relative permeability $\Delta B/\Delta H$ depends on the position on the hysteresis cycle and the amplitude of ΔH .

This effect has to be measured if one wants to exploit this method with high precision. The measurement can easily be performed by a gradient coil which only measures the quadrupole moment of the magnet. With the gradient coil fixed statically inside the magnet the current is set to a constant level and the harmonic excitation by the back leg winding is put on. The constant bias field does not induce any voltage in the gradient coil and the measurement gives directly the change of the quadrupole field due to the back leg excitation. Measurements at different bias fields lead to a calibration table for the relative permeability.

Neglecting this effect, the measurement can provide less precise information about the beta function or relative comparison of it at different locations in the accelerator. Assuming the relative permeability equal to the permeability, the beta value can be calculated from the ratio of the current in main and back leg windings. An example of measurements (see Table 4.5) shows that the measured values are not far from the theoretically expected. So the relative permeability does not seem to be very different from the permeability. But it is not possible to give the precision of the measurement until the relative permeability is measured.

Chapter 5

Low- β insertion quadrupole movements

Although the quadrupoles are carefully aligned with a residual vertical misalignment of $150 \mu\text{m}$ rms before the running period starts, they can still drift and change their position during operation, causing the orbit to change.

Since the beginning of the LEP running, large drifts of the closed orbit in the vertical plane have occurred during the normal operation. Frequent orbit corrections by the operation crew were required to avoid a loss in luminosity. On average, more than 20 corrections were made during the lifetime of a coast. The orbit in the horizontal plane is much more stable and only very few corrections are required during a coast.

The superconducting low-beta insertion quadrupoles (QS0) were suspected to be the source of the drifts. Their strength and the large value of the vertical beta function at this location make the closed orbit very sensitive to any vertical mechanical movements of these magnets. The horizontal beta function is more than 25 times smaller than the vertical so that possible horizontal movements have a smaller influence on the orbit.

The way these magnets are supported makes it likely that they can move. They have to be close to the interaction point in order to create the small beam sizes there. Hence, they are mounted in a cantilever support structure which is fixed on the tunnel ground and extends into the experimental detector. The cantilever arm is about 5 m long and is not supported inside the detector (see Fig. 5.1).

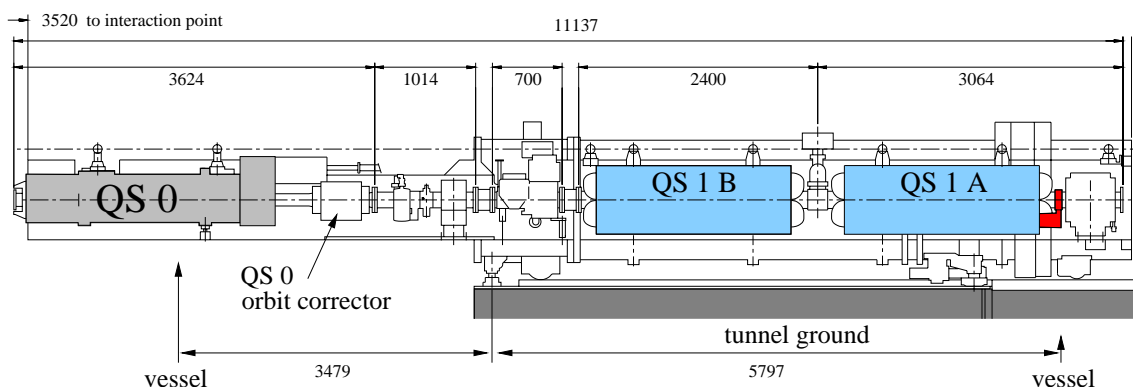


Figure 5.1: Support structure of a superconducting low-beta insertion quadrupole magnet (QS0) at the right side of IP8. The positions of the vessels for the differential pressure system described in Section 5.2.2 are indicated.

The layout of the interaction region at IP 2 is different from the other IPs. In addition to the cantilever structure for the QS0, the magnets nearest to the experimental detector (QS0, QS1A and QS1B) are supported together with the inner parts of the detector in a 32 m long support tube. The tube is sustained at both ends by motorised jacks to enable automatic positioning of the tube by a control system [Mar89b]. This tube can be an additional source of movements.

The vertical orbit correction was the most frequent operation during physics fills. In 1994, a total of 13 222 vertical corrections were done while preparing for, or during physics data taking [Col95]. The frequency of the orbit corrector magnets used for the corrections showed that the correctors near QS12 and QS8 in the experimental straight sections were by far the most popular correctors.

These correctors have a betatron phase advance of $n\pi$ ($n = \text{integer}$) to the low-beta insertion quadrupole magnets (QS0). It was believed that the drifts originate from the QS0 magnets and the MICADO correction algorithm favoured these correctors since the correctors near the QS0 were disabled to avoid local orbit bumps at the IP [Bur95, Col95]. The orbit correction strategy was changed during the 1995 operation period. Afterwards, the majority of orbit corrections were made with the correctors close to the QS0 magnets [Wen96]. This gave strong evidence for the QS0 magnets being the source of the drifts and initiated this analysis.

Orbit movements caused by low-beta insertion quadrupoles have also been reported from other accelerators [End95, Moo95].

5.1 Implications from the beam optics

The superconducting low-beta quadrupoles are vertically focusing and are operated at a quadrupole strength ($k = -0.16 \text{ m}^{-2}$) 10 times larger than other magnets in LEP in order to obtain small beam sizes at the interaction points. In addition, the vertical beta function has its maximum at the location of the QS0s. It is close to 400 m for the optics for colliding beams with a squeezed $\beta_y^* = 5 \text{ cm}$ at the IP.

A misplacement of a single magnet by $\Delta y_Q = 10 \mu\text{m}$ creates an angular orbit kick of about $3.2 \mu\text{rad}$. This leads to an orbit oscillation with rms pickup readings of more than $\sigma_y = 400 \mu\text{m}$ for the squeezed optics with $\beta_y^* = 5 \text{ cm}$ (see Fig. 5.2). For the injection optics with $\beta_y^* = 10 \text{ cm}$ the same misalignment results in $\sigma_y \sim 280 \mu\text{m}$. A $10 \mu\text{m}$ vertical misalignment of a vertically focusing or defocusing quadrupole magnet of the regular FODO structure in the arc only results in an orbit change σ_y of 23 and $15 \mu\text{m}$, respectively.

If the orbit is not corrected, the QS0 misalignment of $10 \mu\text{m}$ leads to a vertical dispersion of 2.7 cm rms. Vertical dispersion can increase the vertical beam size and results in a decrease of luminosity.

The beta function is symmetric around the interaction points, and the vertical phase advance between the two magnets of each low-beta quadrupole pair is nearly π . This causes that the effect on the closed orbit nearly cancels if both magnets move by the same amount in the same direction, as it can be seen from Eq. 2.23. An orbit kick on one side is corrected by a kick of the same size on the other side. A common movement of $\Delta y_Q = 10 \mu\text{m}$ for both QS0s results in a rms orbit change of only $\sigma_{\Delta y} = 8 \mu\text{m}$ (see Fig. 5.3). This implies that coherent movements of both magnets are difficult to detect in the closed orbit measurements in the presence of small measurement errors.

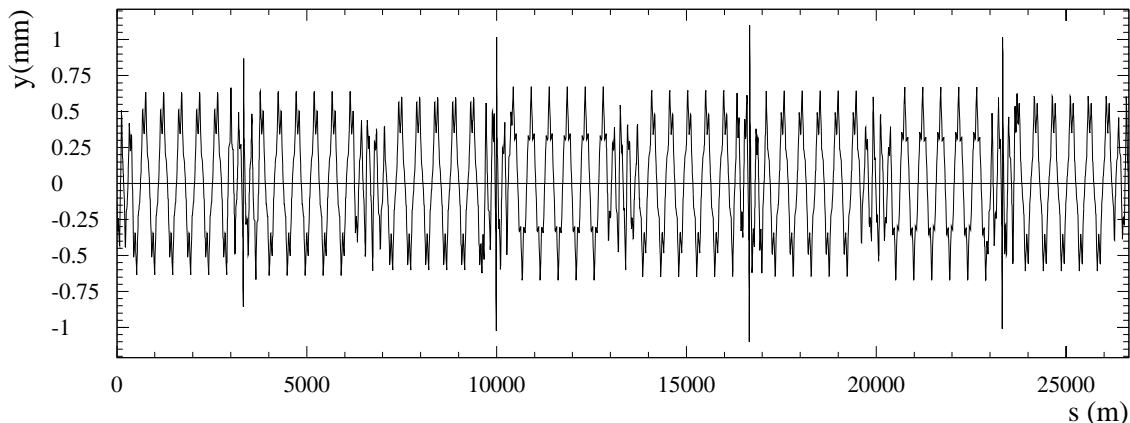


Figure 5.2: Vertical closed orbit due to $10\ \mu\text{m}$ misalignment of one low-beta quadrupole (QS0.R2) for the squeezed optics (m05p80_v2) with $\beta_y^* = 5\ \text{cm}$ and a phase advance μ_x/μ_y of $90/60^\circ$ per FODO cell. The rms of the pickup readings is $\sigma_y = 0.424\ \text{mm}$.

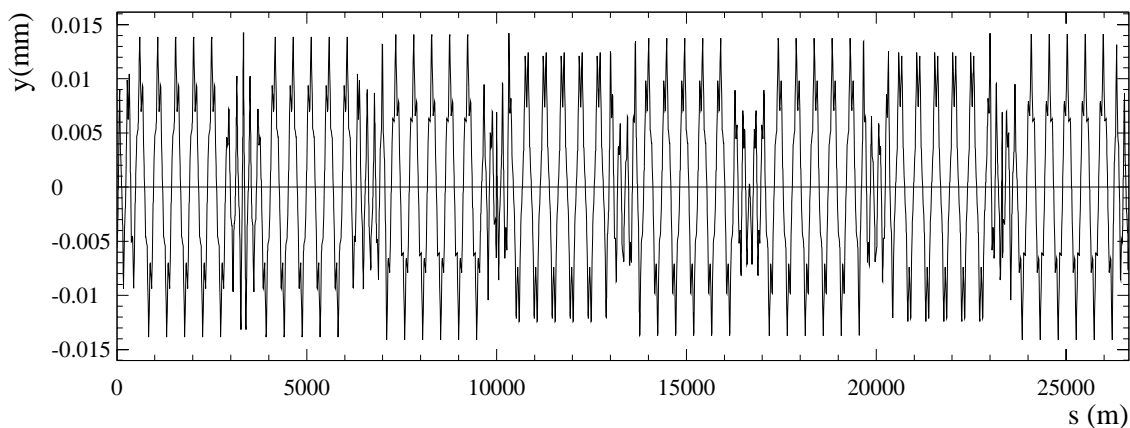


Figure 5.3: Vertical closed orbit due to $10\ \mu\text{m}$ common misalignment of a low-beta quadrupole pair (QS0.L2 and QS0.R2) for the squeezed optics with $90/60^\circ$ phase advance and $\beta_y^* = 5\ \text{cm}$ (note the different scale compared to Fig. 5.2). The rms of the pickup readings is only $0.008\ \text{mm}$, more than 50 times smaller than in the case of a single misaligned QS0.

The reason for the large difference between a movement of a single QS0 and a pair can also be understood in a slightly simplified more figurative picture. When one QS0 quadrupole moves, one additional orbit kick is created (see Fig. 5.4). The kick is in a region where the beta function is large and transforms into a large orbit excursion (see Eq. 2.23).

When both magnets of a QS0 pair move in common, the kicks in the orbit nearly cancel (see Fig. 5.5). The effect on the beam is a parallel displacement. An orbit excursion transforms to other locations in the accelerator scaled by the square root of the beta function. Since the beta function has its maximum at the location of the QS0 magnets, the effect is smaller in the rest of the machine.

The actual effect on the closed orbit is a bump at the interaction point between the low-beta quadrupole pair which is not completely closed. This is shown for the case of IP 2 in Fig. 5.6.

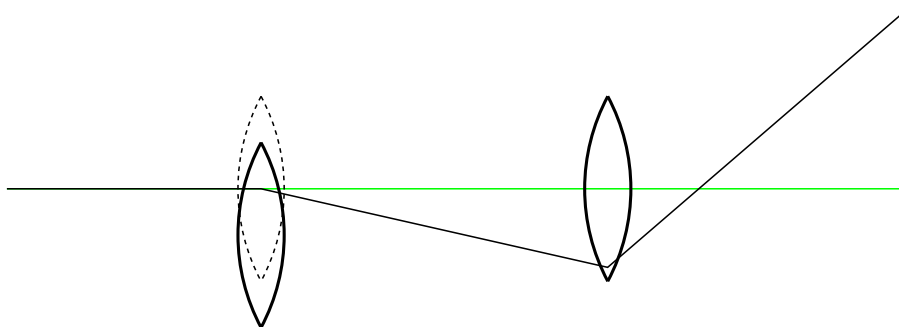


Figure 5.4: A displacement of a single QS0 quadrupole magnet results in a kick in the closed orbit. The beta function at this location is large. Therefore, the kick creates a large orbit distortion.

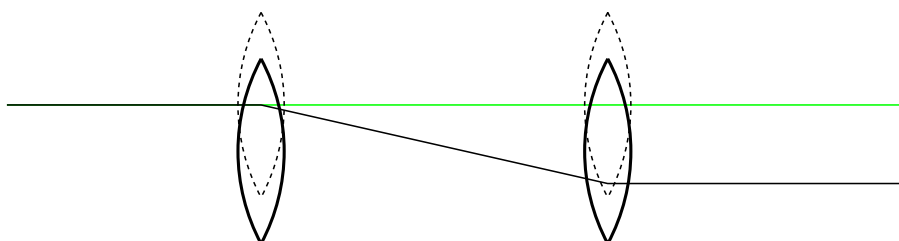


Figure 5.5: A common displacement of a QS0 quadrupole pair leads to a cancellation of the closed orbit kicks. Only a displacement of the beam remains which has a smaller influence on the closed orbit.

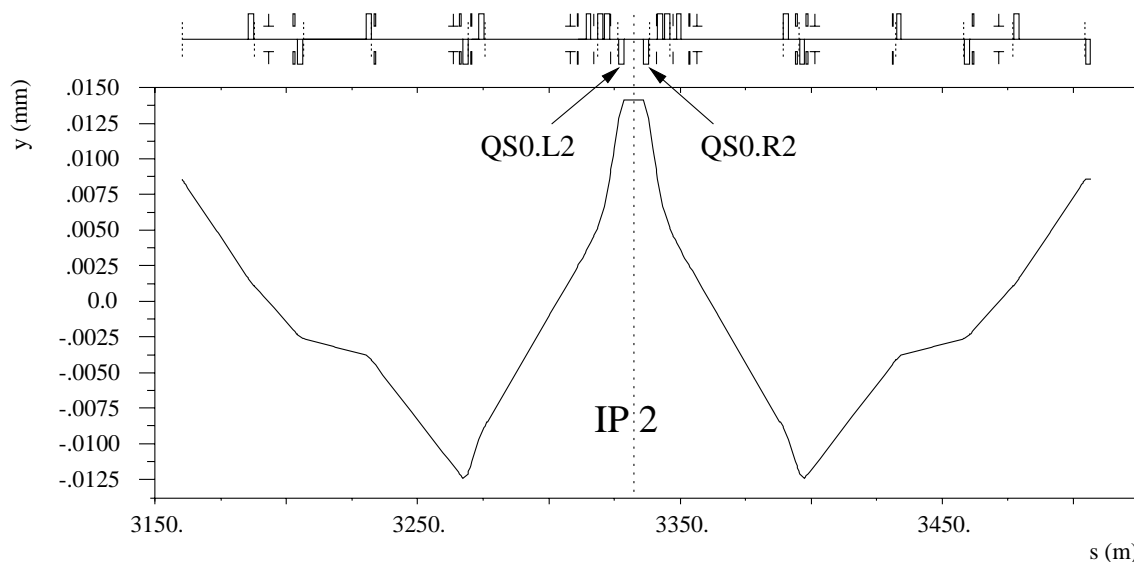


Figure 5.6: Vertical closed orbit around IP 2 due to $10 \mu\text{m}$ common misalignment of the low-beta quadrupole pair QS0.L2 and QS0.R2 for the squeezed optics with 90/60 degrees phase advance and $\beta_y^* = 5 \text{ cm}$.

magnet corrector	QS0.R2 CVB.QS1B.R2	QS0.R4 CVC.QS0.R4	QS0.R6 CVC.QS0.R6	QS0.R8 CVC.QS0.R8
optic	$\Delta y'$ [μrad]	$\Delta y'$ [μrad]	$\Delta y'$ [μrad]	$\Delta y'$ [μrad]
m05p80_v2	3.940	3.443	3.453	3.445
m10p80_v2	3.942	3.430	3.454	3.443
n0520p97_v2	3.898	3.427	3.419	3.427
n1020p97_v2	3.899	3.467	3.430	3.467
y0525f92_v1	3.857	3.584	3.374	3.584
y1025f92_v1	3.870	3.596	3.386	3.596

Table 5.1: Orbit correction kick for $-10 \mu\text{m}$ misalignment of a QS0 magnet for different optics.

The movements of a single QS0 can be easily detected in the closed orbit. The misalignment and orbit correction were simulated with MAD [Gro90]. A $10 \mu\text{m}$ misalignment of a QS0 which causes about $400 \mu\text{m}$ rms orbit change can be corrected with only one corrector magnet to 2 to $5 \mu\text{m}$ rms. Table 5.1 shows the strength of the correction kick for different optics. The correction kicks for the squeezed physics optics ($\beta_y^* = 5 \text{ cm}$, optics name like x05...) and injection optics ($\beta_y^* = 10 \text{ cm}$, optics name like x10...) differ by only up to 1%. The difference between the $90/60^\circ$ phase advance optics (n..., m...) and the $108/90^\circ$ phase advance optics (y...) is only 4%.

In the presence of small measurement errors it is impossible to distinguish which magnet of a QS0 pair moved. A magnet on one side moving downwards or the one on the other side moving upwards nearly have the same effect. So the orbit correction based on the BPM readings has some ambiguity. A correction on the wrong side creates a nearly closed symmetrical ' π -bump' at the IP, very similar to a common movement of the magnet pair. Fig. 5.7 shows the local orbit around the IP.

Both common displacement of a low-beta magnet pair and individual movement with correction on the wrong side lead to a change of the orbit position at the IP. A $10 \mu\text{m}$ movement causes a transverse displacement of the IP of about $14 \mu\text{m}$. This cannot be seen in the orbit measurement since no orbit monitors are between the two QS0s, and the perturbations outside this region are too small to be seen in the noise of the orbit measurement.

Large movements are problematic since the knowledge of the transverse position of the interaction region inside the experimental detector is important for the event analysis. It is useful to identify b (bottom) quarks taking advantage of their relatively long lifetime ($\sim 1.5 \text{ ps}$). The distance between the primary vertex at the IP and the secondary vertex where the b quark decays is longer than for lighter quarks. Knowledge of the primary vertex improves the performance of the selection of the b quarks (*b-tagging*).

The secondary vertex can be reconstructed from tracks in vertex and tracking chambers. For LEP I with a high rate of events from Z decays, the primary vertex could be reconstructed from the distribution of extrapolated tracks with a precision of typically $\sigma_x \sim 20 \mu\text{m}$ and $\sigma_y \sim 10 \mu\text{m}$ every few minutes.

At LEP II, the cross section decreases and the statistics is not high enough to reach the desired precision for the primary vertex reconstruction. Alternative methods of determining the beam position become important. The position at the IP can be extrapolated from orbit measurements. But common movement of a QS0 quadrupole pair which can not be

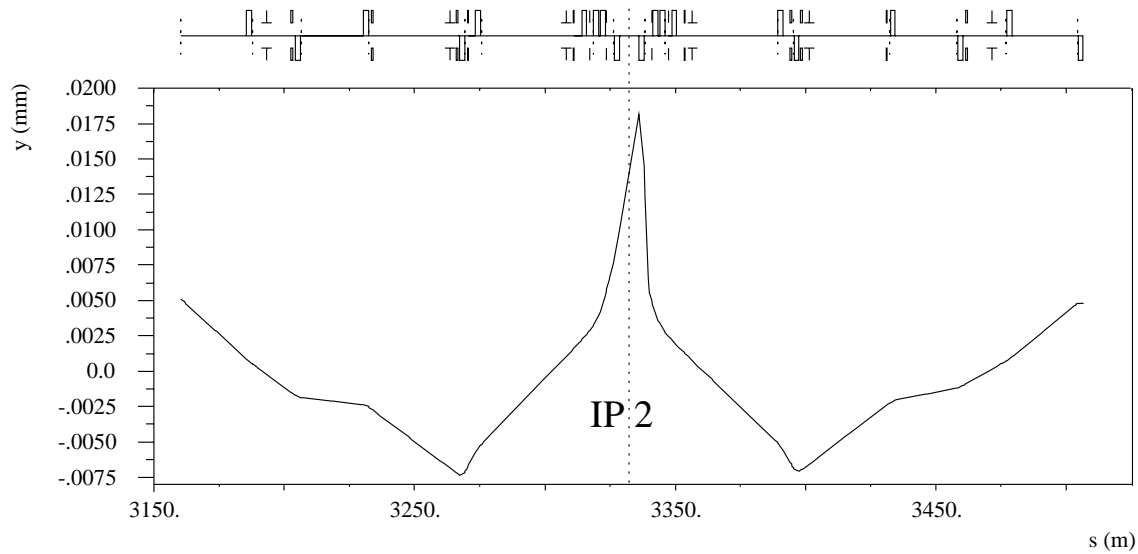


Figure 5.7: Vertical closed orbit around IP 2 due to $10\ \mu\text{m}$ misalignment of the low-beta quadrupole QS0.L2 and orbit correction using the corrector near QS0.R2 for the squeezed optics with $90/60$ degrees phase advance and $\beta_y^* = 5\ \text{cm}$. The orbit is very similar to the orbit for a common displacement of the low-beta quadrupole pair in Fig. 5.6.

detected in the orbit leads to a change in the beam spot position. Hence the QS0 positions have to be monitored and taken into account in the extrapolation. A more detailed report on this topic can be found in [Hol96].

The movement of the low-beta quadrupole magnets is also important for the polarization. The level of polarization strongly depends on the vertical closed orbit. Already small movements of the QS0 magnets lead to significant orbit changes and can increase the strength of the depolarizing Fourier components. Fig. 5.8 shows the change in the Fourier components for the orbit change caused by a QS0 movement of $10\ \mu\text{m}$ for an optic which was commonly used for polarization studies. Some of the Fourier amplitudes are very strong where the particular strength originates in the symmetry of LEP [Kou88]. This would lead to a drastic reduction of the polarization level (see Fig. 2.8) when the spin tune of the machine is close to one of these strong integer resonances. It is clear that any orbit movements during polarization measurements have to be avoided. A LEP optic with the low-beta quadrupole magnets off was specially designed for polarization [Uyt97].

5.2 Hardware for position monitoring

Different systems have been implemented to measure the variations of the positions of the low-beta quadrupole magnets. There are

- Hydrostatic Levelling Systems (HLS)
- a differential pressure system
- potentiometer based systems.

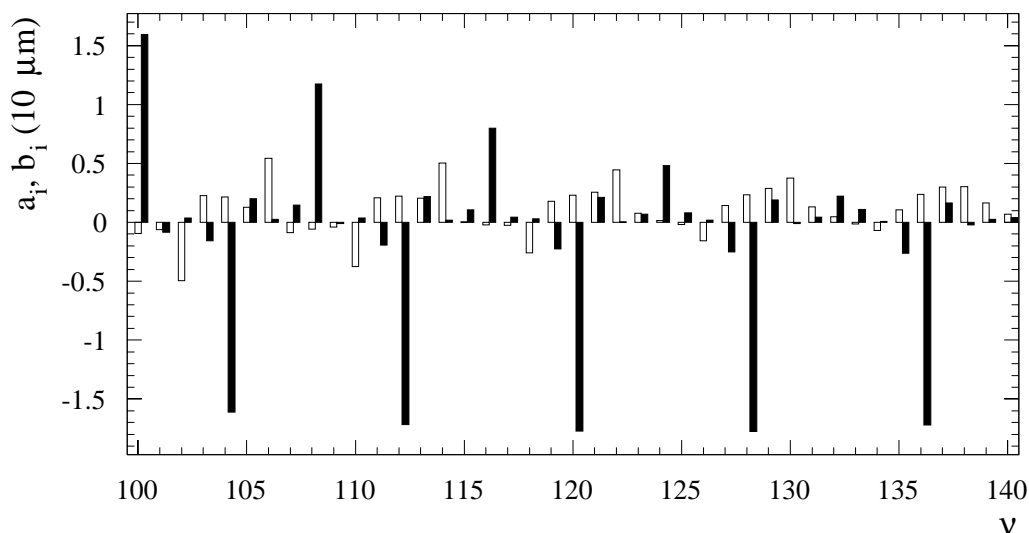


Figure 5.8: Strength of the depolarizing Fourier components of the vertical orbit for an uncorrected movement of $10\ \mu\text{m}$ of a low-beta quadrupole (QS0.R8). The results are for a 90/60 degrees phase advance optics with $\beta_y^* = 10\ \text{cm}$. a_i are empty, b_i are filled bars.

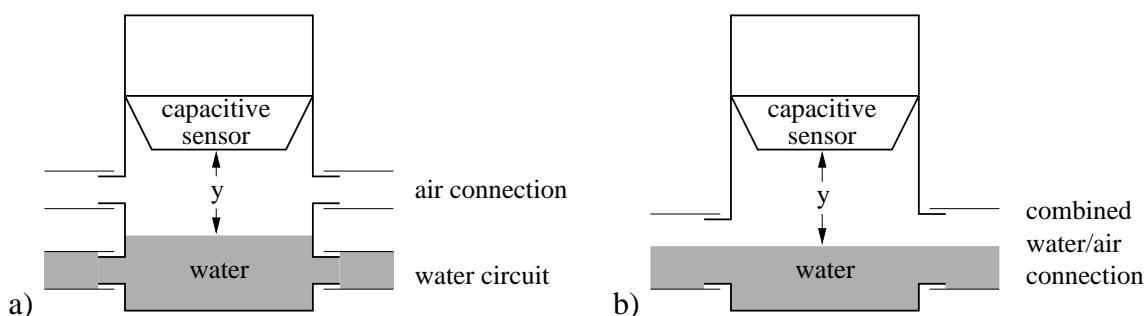


Figure 5.9: a) HLS vessel with separate connecting tubes for water and air. b) HLS vessel with a connecting tube partially filled with water. A capacitive sensor measures the distance from the top to the water level in both types.

5.2.1 Hydrostatic Levelling Systems

The hydrostatic levelling system used at LEP is a commercially available system [Fog]. It consists of vessels with capacitance-based hydrostatic sensors and temperature sensors connected by communicating tubes. Two different types of vessels are used (see Fig. 5.9): One type has connections for separate water and air circuits where the water tubes are completely filled with water. The other type has a connection for one tube which is only partially filled with water. A fungicidal additive is added to the water in the circuit. The vessels are placed at different locations on the magnets, support girder and the tunnel ground. Hence relative changes in the height of the vessels can be detected.

The capacitive sensor in the top of the vessel detects the changes in the capacity with different water level in the container. The individual vessels with their electronics are carefully calibrated. They are equipped with PT100 temperature sensors to compensate for variations in the specific mass of the water with temperature. Polynomials of third or

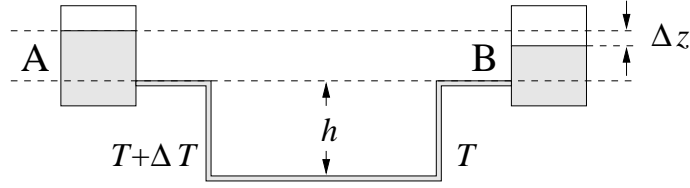


Figure 5.10: Measurement error caused by temperature difference

fourth order are applied to correct for nonlinearities of the electronics. The measurements of the water level in the vessels reach a resolution of the order of $0.2 \mu\text{m}$ over their range of 5 mm.

The precision of the hydrostatic levelling system is limited by effects of thermally caused density differences of the water. The changing density alters the hydrostatic pressure. The temperature is only measured at some points of the circuit between the vessels. So all non-horizontal parts of the tubes introduce a measurement uncertainty Δz due to the unknown temperature difference ΔT (see Fig. 5.10). A vertical tube of height h with a temperature difference ΔT creates a pressure difference Δp between points in the vessels A and B which are at the same height as

$$\Delta p = gh\Delta\rho = gh \left(\frac{\partial\rho}{\partial T} \right)_T \Delta T \quad (5.1)$$

with $g = 9.81 \text{ m/s}^2$. $\partial\rho/\partial T = -206 \mu\text{g}/(\text{cm}^3 \text{ K})$ at $T = 20^\circ\text{C}$, $-257 \mu\text{g}/(\text{cm}^3 \text{ K})$ at $T = 25^\circ\text{C}$ and $-300 \mu\text{g}/(\text{cm}^3 \text{ K})$ at $T = 30^\circ\text{C}$. This implies that a height difference $h = 1 \text{ cm}$ at $T = 20^\circ\text{C}$ causes $\Delta z = 2 \mu\text{m}/\text{K}$. It is obvious that the height variations in the connecting tubes and the temperature differences have to be kept very small.

For this reason it is very appealing to use horizontal tubes which are partially filled with water. The water level adjusts itself horizontally and no height differences are present.

An alternative solution for the operation can be used in the case of unavoidable height differences in the tubes. Valves in the connecting tubes close to the measurement vessels can separate these from the connecting tube network. First, water from a large reservoir is circulated in the tubes until the water temperature is fairly homogeneous. After the water circulation is stopped, the valves are opened again. After a short waiting time, oscillations in the tubes are damped and measurements can be taken until the temperature differences become too important again. Hence this type of system can not be used for continuous measurements.

The first HLS system was installed in the shutdown 1994/95 at one of the experimental interaction points (IP 8). It consisted of 8 vessels connected by non-horizontal tubes with a possibility to circulate the water. The vessels were placed on positions on the supports for the QS1 and the tunnel ground (see Appendix B.2). No sensor was installed on the QS0. A separate system measured the position of the QS0 relative to the end of the support structure at IP 8 (see Section 5.2.2).

The layout of the HLS was changed in order to minimise temperature effects and to measure in particular the position of the QS0 (see Fig. 5.11). This scheme was implemented at IP 2, 4 and 6 for the 1996 running period, and at IP 8 for 1997. On each side of the interaction point, there is a system with four measurement vessels on the

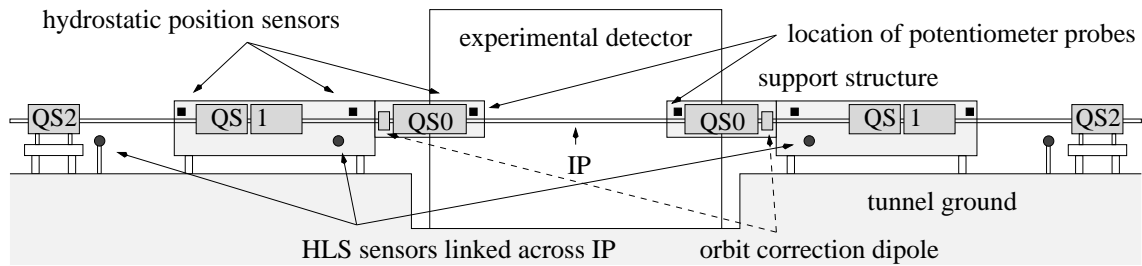


Figure 5.11: Schematic view of the low-beta insertion around an experimental detector. The layout of IP 2 is slightly more complicated since the inner magnets (QS0, QS1) and the inner parts of the detector are mounted in a support tube (not shown).

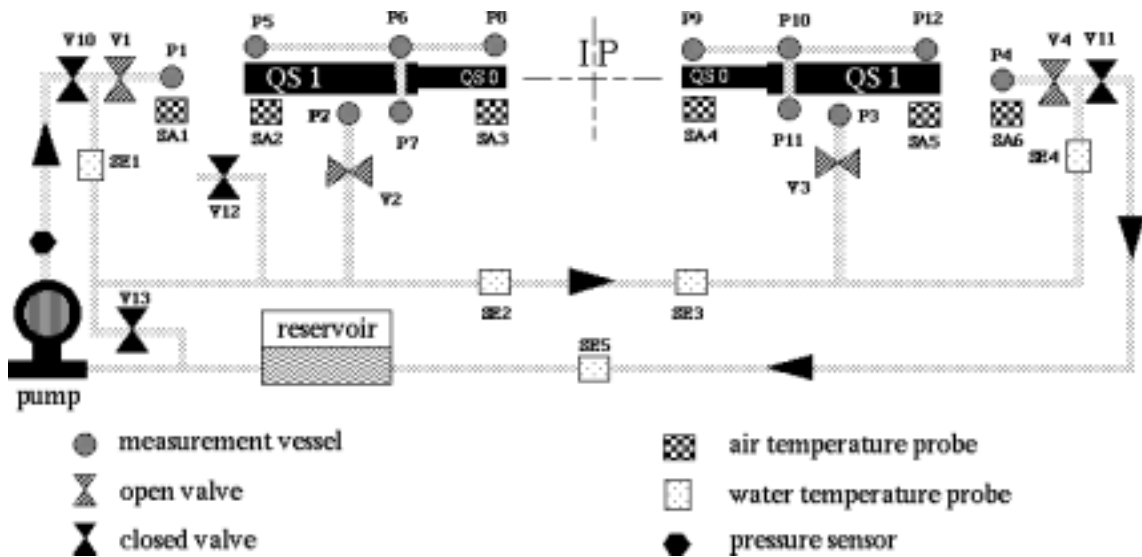


Figure 5.12: Schematic view of the hydrostatic levelling system installation at IP 2, 4 and 6. The layout of IP 8 was modified like this for the 1997 running period. The locations of vessels P8 and P9 are slightly different for the various interaction points (see Appendix B.2).

support for the QS0 and the next closest magnets (QS1A and QS1B). It has *horizontal* connecting tubes partially filled with water. Since the water level is horizontal, local temperature differences do not introduce any significant measurement error. It is not needed to circulate the water in these systems.

A different system of communicating vessels is connecting the supports and the ground on both sides of a detector. It was not possible to install the tubes in a horizontal plane and the precision is limited by temperature effects. Valves can disconnect the vessels from the communicating tubes, and the water can be circulated to homogenise the temperature. A sketch of the locations and numbering of the different probes can be seen in Fig. 5.12. Due to space restrictions, the location of the individual vessels slightly differ for the different IPs. The detailed layouts are given in Appendix B.2.

The HLS systems with this new layout became fully operational at IP 4 and 6 in the beginning of 1996 LEP operation, IP 2 after the October technical stop for the 86 GeV period and IP 8 in 1997. The measured position and temperature values are logged in the LEP measurement database. A description of the tables can be found in Appendix B.1.

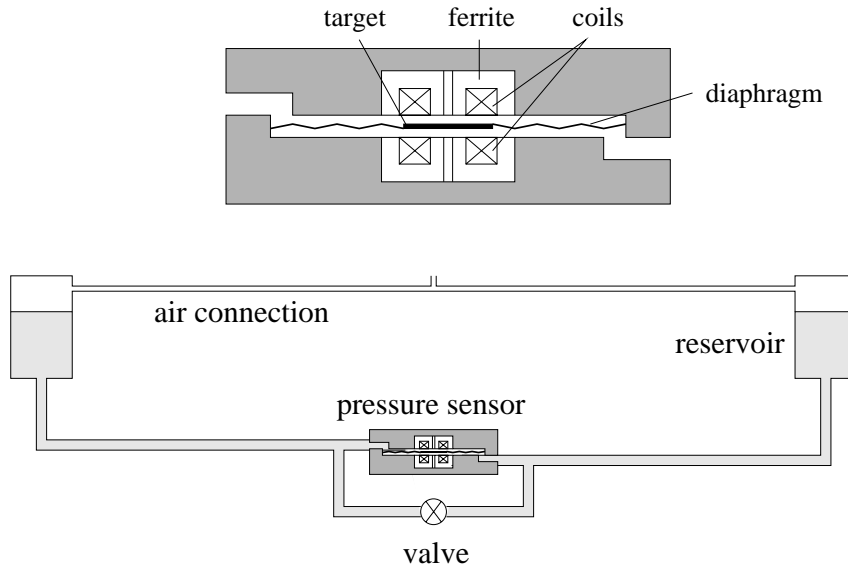


Figure 5.13: Differential pressure sensor and layout of the installation.

5.2.2 Differential pressure system

A differential pressure system was the first device that measured the position of the QS0 quadrupole magnets at IP 8. The system monitors the height variations between the QS0 magnet and the external end of the support structure (see Fig. 5.1). The system, as shown in Fig. 5.13, is based on a differential pressure sensor detecting pressure differences at the two sides of a diaphragm between AC operated coils. Eddy current losses in the target between the coils make the apparent inductance of each coil change when the diaphragm moves. Two reservoirs are connected to the pressure sensor with a bypass valve in parallel to equilibrate the system. The reservoirs are connected by an air tube to assure the same pressure at the water surface. The system is similar to a system used for the L3 experiment support tube described in more detail in [Mar89a].

The bypass valve is closed during operation and the height variations between the reservoirs result in a change of the hydrostatic pressure. This moves the diaphragm and allows to calculate the magnitude of the height variation. Temperature differences in the vertical parts of the water circuit limit the precision of the system like for the hydrostatic levelling system. The tubes connecting the reservoirs to the sensor have some vertical parts with height differences of about 40 cm.

5.2.3 Potentiometer based system

Potentiometer based position sensors monitor the position of the QS0 magnets at IP 4 and IP 8 [Sch95, Cam95]. They had been installed by the experiments to extrapolate the collision vertex position from closed orbit measurements for b-tagging. At IP 8, they measure the position of the DELPHI luminosity calorimeter attached at the QS0 magnets relative to the main detector. The similar system at IP 4 monitors movements between the QS0 supports and reference surfaces on the ALEPH main detector. These pin potentiometer systems have an intrinsic resolution of a few micron.

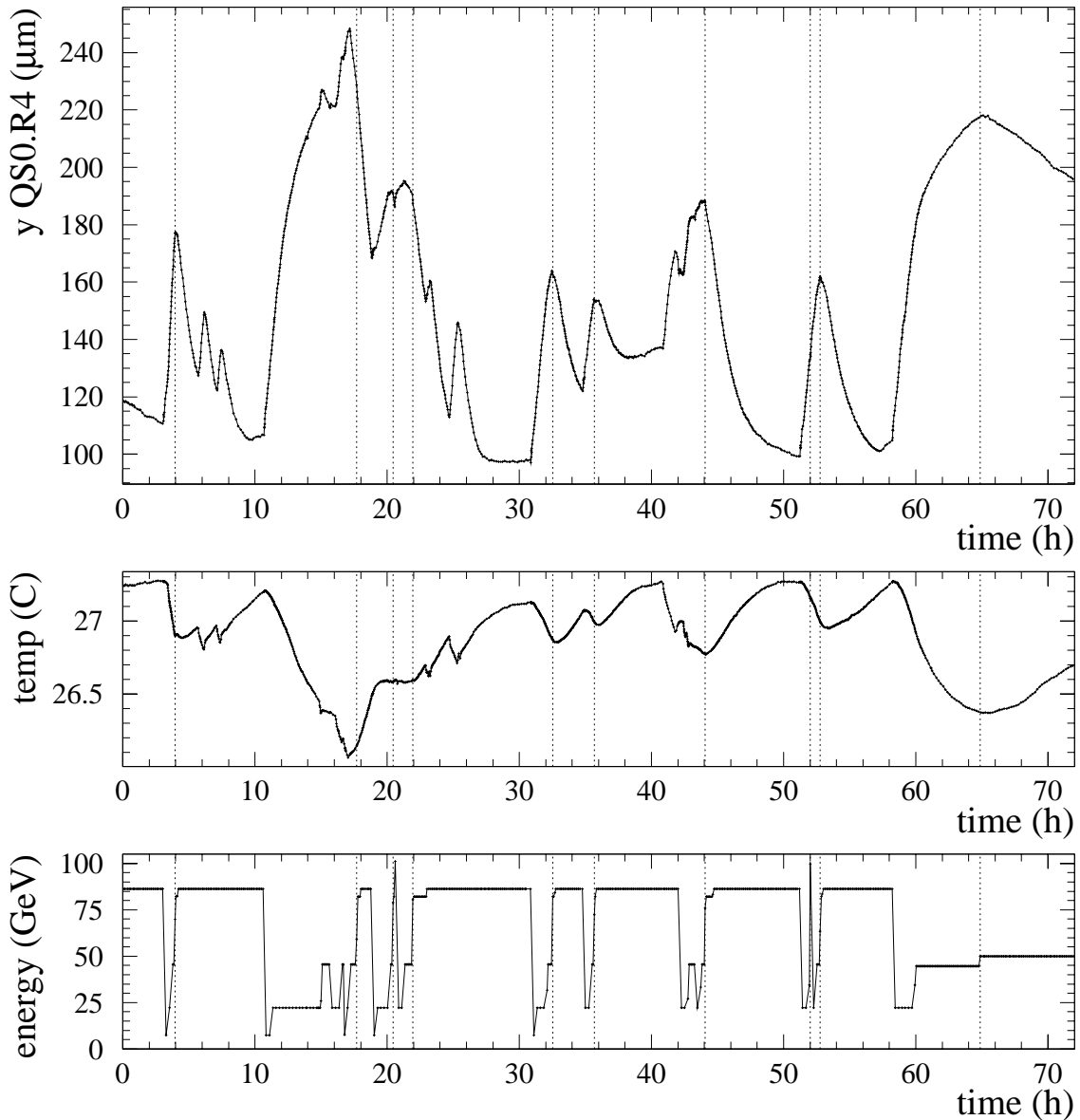


Figure 5.14: Movement of one low-beta quadrupole magnet (QS0.R4, difference between vessel P9 and P11) (top), the temperature measured at the support of this magnet (middle) and LEP beam energy (bottom) during a period of three days starting on Nov 1st 1996, 0:00. The vertical dashed lines indicate the end of the ramp to collision energy.

5.3 Observed movements

The movements were first monitored with the potentiometer based systems and the differential pressure system at IP 8. During the 1995 LEP operation period, these measurements were taken systematically for the first time. The results of this initial analysis of the observed movements and their correlation to orbit drifts can be found in [Tec96].

The movements show a very characteristic pattern in time. In general, this pattern is nearly identical for all QS0 magnets. An example measured by the hydrostatic levelling system is shown in Fig. 5.14. The relative movements between different parts of the

IP	QS0.L [μm]	QS0.R [μm]	diff. [μm]
2	60	100	50
4	100	130	70
6	80	80	20
8	70	60	40

Table 5.2: Typical amplitude of the vertical QS0 movements in the last period of the 1996 running. The last column shows the amplitude of the differential movement of a quadrupole pair.

support structure which are on the tunnel ground are small compared to the movement of the cantilever part with the QS0 magnet.

The movements are clearly driven by local temperature variations. Fig. 5.14 also shows the temperature measured at the HLS vessel P10 on the support. The movement is well correlated with the temperature changes. When the temperature rises, the magnet starts moving downwards. After a few hours, the magnet reaches an equilibrium position. The amplitude of the movement is up to 140 μm for this magnet. Though the movements show the same pattern, the amplitude is slightly different, as seen in Table 5.2. The amplitude of the differential movement of a QS0 magnet pair, which is causing strong orbit drifts, is in general smaller since the temperature changes are similar on both sides.

The temperature changes are mainly caused by the operation cycle of LEP which is shown in the lower plot in Fig. 5.14. The temperature starts rising after LEP has been ramped to higher energy and decreases again when the current in the magnets is set back to injection level or switched off. The temperature at the end of the cantilever support inside the experimental detector changes usually by less than 0.2°C due to the good cooling there. At other parts of the support, the variations are of the order of 1°C.

The temperature rise can be understood by the higher current heating up the current feed-throughs which traverse the support. The time constant of the thermally driven movements is of the order of a few hours. It is obvious from Fig. 5.14 that a short refilling time keeps the amplitude of the movements smaller. The largest drifts occur between long periods of injection and collision energy.

5.4 Correlation of orbit drifts and quadrupole movements

After the movements of the low-beta insertion quadrupole magnets had been observed, it remained to be studied which contribution to the vertical orbit drifts comes from these magnets.

5.4.1 Orbit analysis

The data from orbit measurements during physics fills was analysed off-line to examine the correlation between the orbit drifts and the mechanical movements. The analysis only uses orbit measurements during stable conditions for data taking by the experimental detectors. This minimises the effects from any changes of the machine settings other than

orbit corrections. The first orbit measurement after the physics experiments start taking data is taken as a reference for each fill.

The orbits of electrons and positrons are separated at some locations to avoid unwanted collisions outside the experimental detectors. This causes orbit excursions large compared to places where the particles are not separated. To prevent any possible effect from these locally large values on the global analysis, the average orbit of electrons and positrons was used for all studies.

Some BPM readings from the orbit acquisition can show unphysically large values. A cut is used to sort out these data. The orbit data y_i are normalised by $\sqrt{\beta}$, the rms value $\sigma_{y/\sqrt{\beta}}$ is computed, and normalised BPMs readings $y_i/\sqrt{\beta}$ larger than $3 \cdot \sigma_{y/\sqrt{\beta}}$ are rejected.

The orbit movements during a fill originate from two sources:

- orbit drifts from magnet movements
- orbit corrections and changes by the operator.

The manual changes have to be eliminated in the analysis in order to study the drifts. For this reason, the ‘bare’ orbit* of the orbit is calculated from the measured orbit y_{meas} by

$$y_{bare} = y_{meas} - \frac{\sqrt{\beta_{bpm}}}{2 \sin \pi Q} \cdot \sum_{corr} \sqrt{\beta_{corr}} \cdot \cos \left(|\mu_{corr} - \mu_{bpm}| - \pi Q \right) \cdot \theta_{corr} \quad (5.2)$$

where the sum is taken over all vertical correctors. θ_{corr} is the angular kick of the corrector, β_{corr} and μ_{corr} are beta function and phase at the corrector, β_{bpm} and μ_{bpm} at the beam position monitors, respectively. This procedure removes the effects of corrector magnets used for orbit corrections. The difference of two bare orbits shows the orbit changes from other sources than corrector magnets. Hence, this represents the orbit drifts that would have occurred without any orbit corrections being done.

The bare orbit is calculated for all subsequent orbits, and the difference Δy_i to the reference bare orbit is evaluated. In some cases, individual difference values are very large compared to the rms due to problems in the orbit acquisition. They are excluded by applying another rejection cut where the normalised difference $\Delta y_i/\sqrt{\beta}$ is larger than $3 \cdot \sigma_{\Delta y/\sqrt{\beta}}$. The rms difference of the bare orbits $\sigma_{\Delta y}$ is then computed in the regular FODO structure in the arcs.

An example of the movements during a fill is given in Fig. 5.15. Orbit drifts up to more than 3 millimetre (compared to a typical residual vertical rms of about 500 μm) would appear during a fill of several hours without orbit correction. The strongest drifts usually happen at the beginning of the fill and reach a stable position later, analogous to the movements of the low-beta magnets. Occasionally, large drifts occur at a later time during the fill.

The maximum of the rms orbit change $\sigma_{\Delta y}$ during each fill was analysed as a function of the fill length for the 1996 running period. Fig. 5.16 shows that the amplitude of the orbit drift is increasing until a fill length of about 6 hours and does not increase significantly further for longer fills. The typical amplitude of the orbit change was about 1.5 mm rms for fills longer than 4 hours.

*The closed orbit if all correction magnets were switched off.

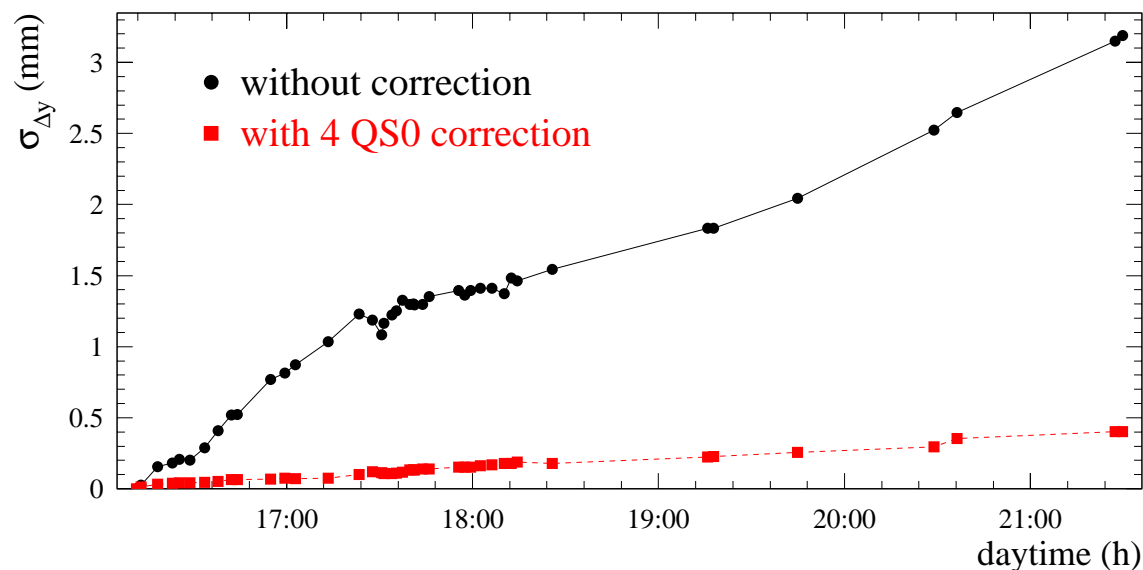


Figure 5.15: Rms difference of bare orbits during a physics fill (# 3677) relative to the first physics orbit. The orbit drifts would add up to more than 3 mm without correction. A typical vertical orbit has a residual rms of about $500 \mu\text{m}$. The orbit change can be corrected with only 4 QS0 corrector magnets to below 0.4 mm.

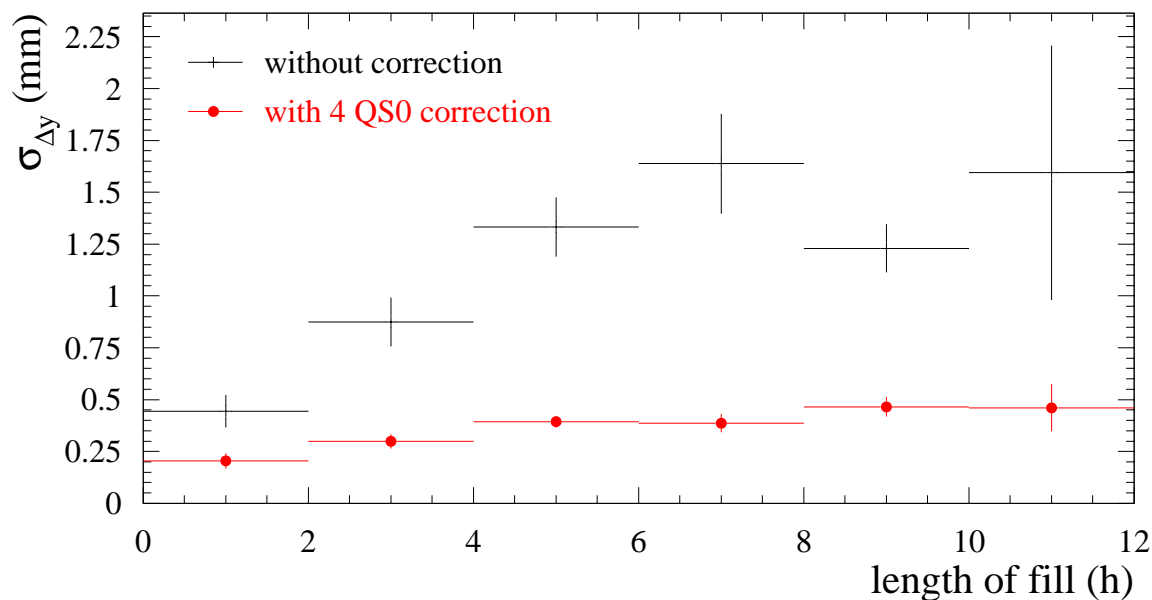


Figure 5.16: Maximum of the rms orbit change $\sigma_{\Delta y}$ during a fill as a function of the fill length.

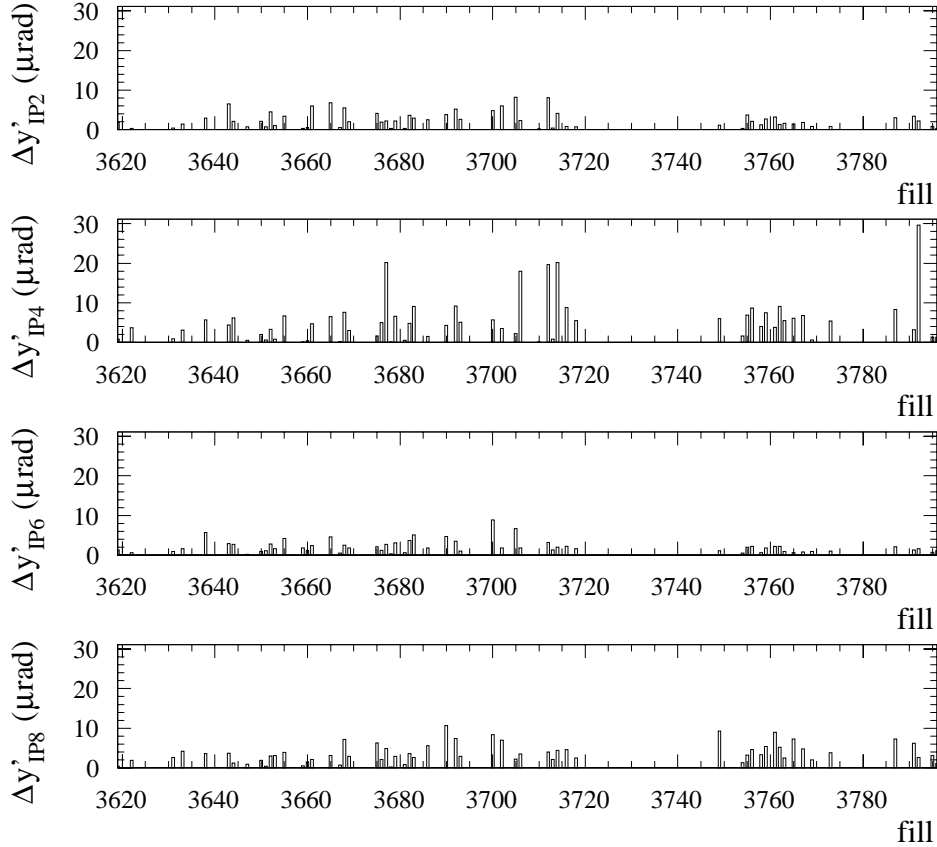


Figure 5.17: Size of the calculated orbit correction kicks $\Delta y'$ at the four IPs for a period in Oct./Nov. 1996. The mean kick amplitude was IP 2: $2.5 \mu\text{rad}$, IP 4: $5.5 \mu\text{rad}$, IP 6: $2.1 \mu\text{rad}$ and IP 8: $3.6 \mu\text{rad}$.

If the QS0 magnets are the source of the drifts then it should be possible to correct most of the effect with only one orbit corrector magnet per IP. The difference orbit is corrected with the COCU package [Bra90] using the MICADO algorithm [Aut73]. Only one of the two corrector magnets close to a QS0 at each experimental interaction point was enabled for the orbit correction (CVC.QS1B.R2, CVC.QS0.R4, CVC.QS0.R6, CVC.QS0.R8). The results showed that this correction is very effective, taking away about 70–90% of the orbit movements (Fig. 5.15, 5.16). This proves that the main contribution to the orbit drifts originates in the movements of the low-beta magnets. The residual orbit change, which can not be corrected by the 4 QS0 correctors, stays below 0.5 mm. This can come from the common movements of the QS0 quadrupoles and from other sources.

The evolution of the calculated correction kicks $\Delta y'$ for the 4 interaction points from the orbit correction was analysed and compared to the differential movements of the QS0 magnets. The correction kicks $\Delta y'$ should be proportional to the differential movement Δy . This was examined for the different interaction points.

Fig. 5.17 shows the size of the calculated orbit correction kicks at the four interaction points during Oct./Nov. 1996. The largest corrections are needed at IP 4 which is also the interaction point with the largest differential QS0 movements (see Table 5.2). The smallest movements and kicks are at IP 6.

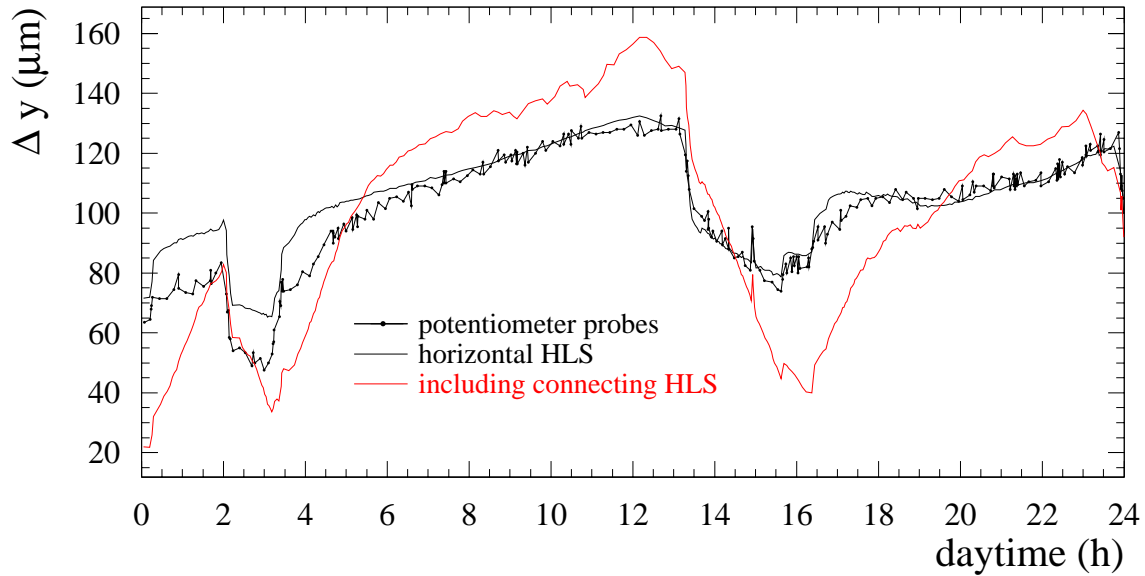


Figure 5.18: Differential movements of the QS0 quadrupole magnet pair at IP 4 during one day.

There is no direct measurement of the differential movements of a QS0 pair by the hydrostatic levelling system. All HLS measurements are relative and have no absolute reference point. The measurement vessels on the QS0 magnets (P8 and P9) are not directly connected to each other. So the two local HLS systems on both sides of the IP and the connecting HLS have to be combined. The best representation of the differential movement of a QS0 pair had to be found empirically.

It was tried to calculate the differential movement including the measured height variations between vessels P2 and P3 which link the two sides of the IP. This was compared at IP 4 with the potentiometer data measuring the QS0 movements relative to the experimental detector as a reference. An example for the movements during a day is shown in Fig. 5.18. The measurements by the position sensitive potentiometers show a bigger noise than the HLS data. The correlation between potentiometer and HLS data was not very good when the difference $y_{P2} - y_{P3}$ was included. This indicates that the connecting HLS system with vertical parts is strongly influenced by temperature variations.

Assuming that the support structures on the tunnel ground do not move relative to each other, the difference $y_{P2} - y_{P3}$ can be neglected. In that case, only HLS vessels with horizontal connecting tubes are used which are not sensitive to the temperature variations. This results in a much better correlation. A comparison with the necessary orbit correction kick at this point confirmed this result.

It can be concluded that the movements between the supports on both sides of the IP which are on the tunnel ground at IP 4, 6 and 8 are relatively small on the timescale of a few days. The precision of the HLS system connecting the supports on both sides of the IP is limited below $\mathcal{O}(10) \mu\text{m}$ and does not improve the correlation. Circulating the water would not allow continuous measurements, so this HLS was not used in further analysis.

At IP 2, 4 and 6, the differential movements of the vessels P8 and P9 were examined relative to various reference points among the vessels P5 to P7 and P10 to P12, respectively. This movement was compared to the calculated correction kick $\Delta y'$. Fig. 5.19

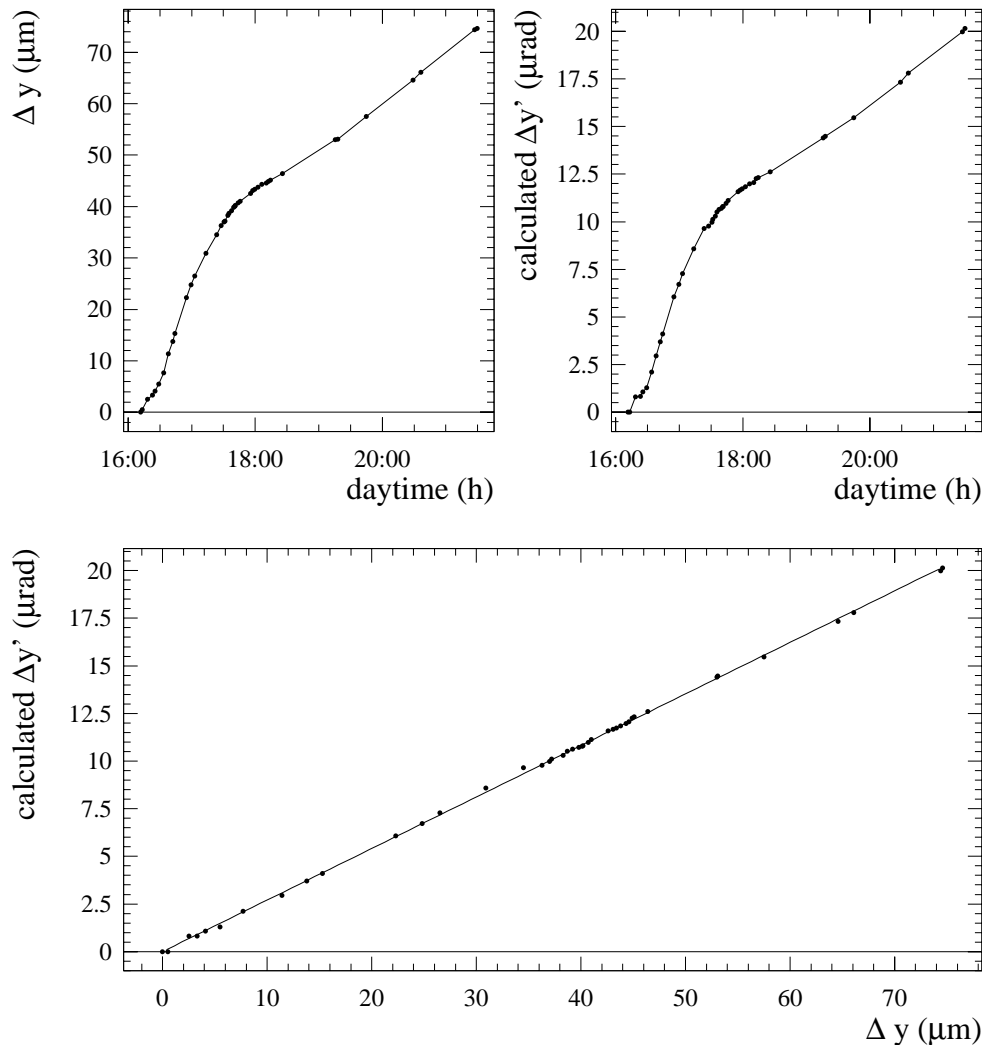


Figure 5.19: Example of the differential mechanical movement of a QS0 pair (top left), the calculated orbit correction kick (top right) and their correlation (bottom) at IP 4 during a fill (#3677) with large quadrupole movements.

shows an example. Usually, the correlation is very good with linear correlation coefficients $\rho > 0.9$ when a large differential movement of more than a few μm occurred. When the movement was smaller, the correlation was worse. This can be understood since both the precision of the HLS is limited and the correction kick from the orbit analysis has a certain error. Consequently, fills with large movements were selected for a detailed study of correlation. The error of the HLS system with horizontal connection tubes was estimated from the scatter to be about $\mathcal{O}(1) \mu\text{m}$.

The best correlation at IP 6 was obtained for the difference $(y_{P8} - y_{P7}) - (y_{P9} - y_{P11})$. The reference points for the installation on both sides are not exactly symmetrical and introducing a scaling factor between the measured movements on both sides was also studied. For IP 4, $0.95 \cdot (y_{P8} - y_{P7}) - (y_{P9} - y_{P11})$ gave better results than the difference between these vessels without scaling factor. The best results at IP 4 were obtained with the difference $(y_{P8} - y_{P6}) - (y_{P9} - y_{P11})$.

At both IP 4 and IP 6, the difference between the vessels on the same side of the support (see Appendix B.2) gave the best correlation. This indicates that there could also be a small tilt movement due to the temperature effects.

At IP 8, the differential pressure system was compared to the potentiometer based system. (The HLS system in the configuration until beginning of 1997 did not measure the position of the QS0 magnets.) The differential pressure system has height differences of about 40 cm in the connecting tubes. So the necessary temperature correction is of the order of $80 \mu\text{m}/^\circ\text{C}$. Since the temperature is not measured at all points of the tubes, the precision of the temperature correction is not sufficient. The correlation of the differential movement to the orbit correction kick is still surprisingly good since the movement is also based on the temperature changes. Even though the temperature correction of the differential pressure system was studied in comparison to the potentiometers, the best correlation between kicks and differential movement was still obtained by the potentiometer system. Averaging the two vertical potentiometer probes on each side of the IP gave the best correlation with $1.3 \cdot (y_{L1} + y_{L2})/2 - (y_{R1} + y_{R2})/2$.

After the modification of the HLS at IP 8 for the 1997 operation period, the HLS data was used. The best correlation was obtained using the difference $(y_{P8} - y_{P7}) - (y_{P9} - y_{P11})$.

The analysis at IP 2 could be started after the October technical stop in 1996. The movements are more complex, since both the support tube and the girders for the QS0 magnets can move. Analogous to the other IPs, the difference $(y_{P8} - y_{P6}) - (y_{P9} - y_{P10})$ was usually well correlated to the calculated orbit correction kick. Nevertheless, the correlation was in some cases worse compared to other interaction points. This is attributed to movements of the support tube.

The proportionality factors between the observed movements and calculated orbit correction kicks were computed for most of the fills with physics data taking. Fig. 5.20 shows an example of the factors calculated for IP 4. The factors for all different IPs are shown in Appendix B.3. No differentiation for the different optics is made since the calculated correction kicks for a given misalignment differ by only a few percent (see Table 5.1). The error bars are obtained from the error of the HLS system only. No uncertainty of the calculated correction kick was included.

Only fills with large integrated correction kicks were used for the analysis. This threshold was set to $\Delta y' = 8 \mu\text{rad}$ for IP 4, $\Delta y' = 5 \mu\text{rad}$ for IP 2 and IP 8 and $\Delta y' = 2.5 \mu\text{rad}$ for IP 6 where the movements were usually smallest.

The weighted mean was computed by a constant value fit. For IP 4, 6 and 8, the mean values are all $(\Delta y'/\Delta y)_{\text{IP } 4,6,8} = 0.29 \mu\text{rad}/\mu\text{m}$ with χ^2/dof of about 2–3. The value of χ^2 is not surprising since the error of the calculated kick was not taken into account. The actual error on the calculated slope is slightly larger than the one used for the fit. An error on the correction kick can be caused by orbit drifts from other sources which are partially corrected by the QS0 correctors.

The obtained proportionality factors are in good agreement with the theoretical value of $(\Delta y'/\Delta y)_{\text{th}} = 0.34 \mu\text{rad}/\mu\text{m}$ taking into account the geometry of the HLS installation. The vessels are fixed at the end of the cantilever structure. Their movements are larger than the movements of the centre of the QS0 magnets, leading to a smaller factor.

The spread of the calculated factor is larger for IP 2 compared to the other IPs. The mean value is $(\Delta y'/\Delta y)_{\text{IP } 2} = 0.23 \mu\text{rad}/\mu\text{m}$, smaller than expected. It should have been about 10 % larger than $(\Delta y'/\Delta y)_{\text{IP } 4,6,8}$ (compare Table 5.1). The support tube at this IP

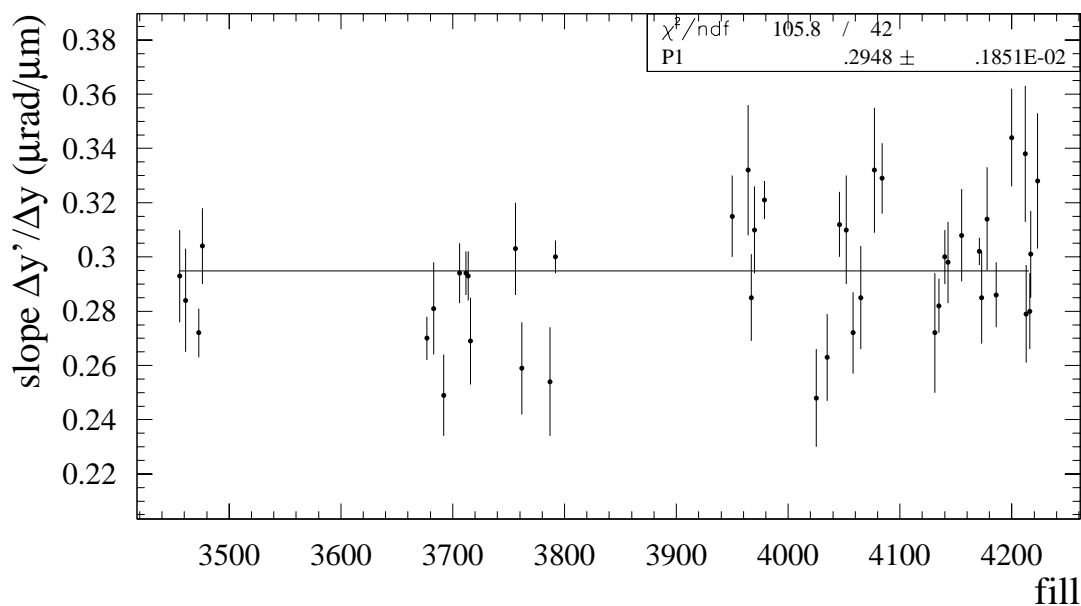


Figure 5.20: Proportionality factors between the observed movements and calculated orbit correction kicks at IP 4. The factors are shown as a function of the fill for the 1996 and 1997 running periods. Only fills where the calculated kick exceeded $\Delta y' = 8 \mu\text{rad}$ are shown.

can move and cause unobserved movements between the reference points. This results in a worse correlation and a larger spread for the calculated factors.

5.5 Orbit correction system

The mechanical measurements of Δy can be used to correct the orbit and keep the drifts small. The necessary orbit correction kick $\Delta y'$ can be calculated from the proportionality factors ($\Delta y' / \Delta y$) and the QS0 movements Δy .

The hydrostatic levelling systems with horizontal connecting tubes on the supports are used for the measurements at IP 2, 4 and 6. At IP 8, the potentiometer system was used until end of 1996 because of the better correlation. From 1997 on, the HLS was used at all interaction points.

A software system was developed which reads the actual QS0 positions measured by the HLS or potentiometer system from the LEP measurement database. The differential position of a QS0 pair is calculated according to the procedure which gave the best correlation in the previous section. The instantaneous difference is taken as the reference when the program is started. The system calculates the difference every minute and determines the differential movements. The necessary orbit correction kicks are computed with the proportionality factor for each QS0 pair. A correction kick is sent to the orbit correction coil whenever it exceeds a certain threshold. This threshold was set to $0.3 \mu\text{rad}$ which corresponds to a differential movement of about $1 \mu\text{m}$ or a orbit drift of about $40 \mu\text{m}$ rms.

Some features were included for the security of the system. When the rms spread of the HLS reading is too large, the data is ignored and no correction sent. A threshold

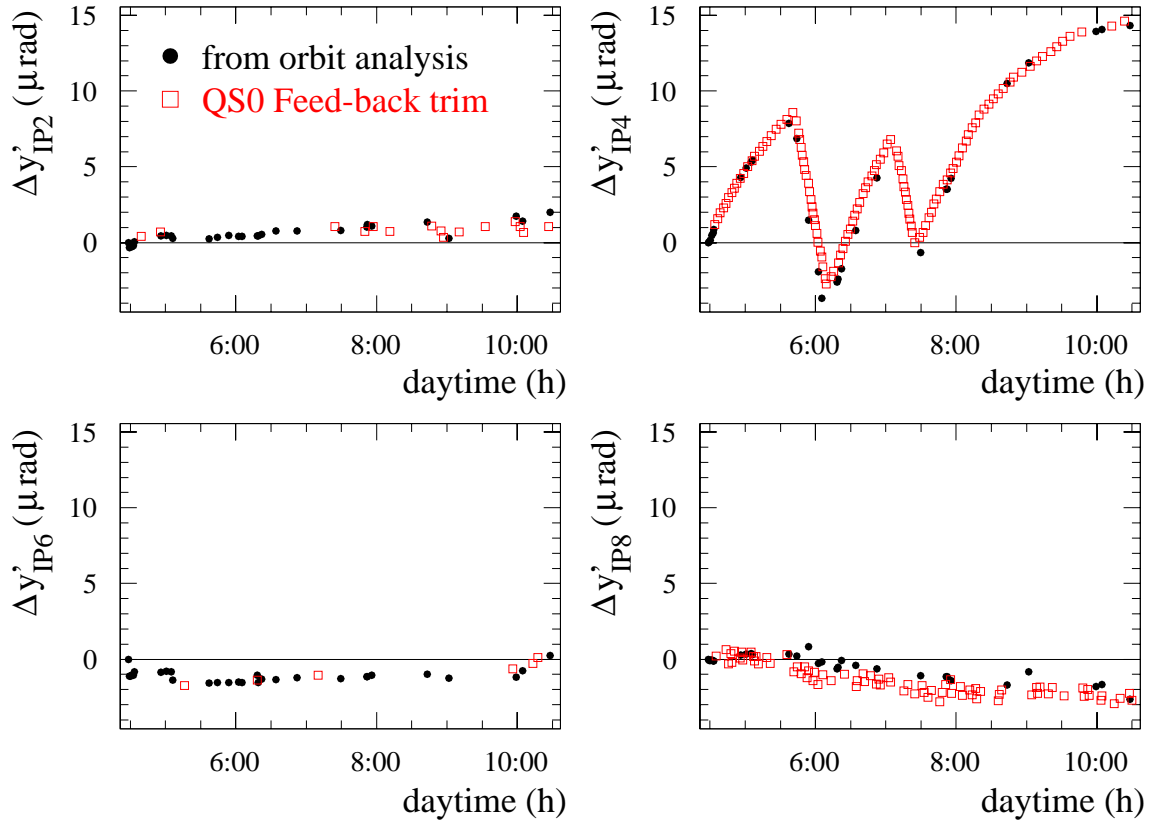


Figure 5.21: Example of the feedback during a fill (#3706) with untypical movements. The correction kicks sent by the feedback are compared to the corrections calculated from the off-line orbit analysis. Every dot corresponds to an orbit acquired by the operator.

for a maximum possible correction kick is set to prevent beam loss by an eventual false position reading.

The system is used during data taking by the experiments to keep the orbit stable. It was not used during the accumulation of particles in LEP since it is not necessary to have a very good orbit quality. During the acceleration and the squeezing process, it cannot be used since the orbit correctors do not take any commands except the preprogrammed ramp.

The system has been running very successfully from the end of the 1996 running period of LEP. An example of the correction trims during a fill is given in Fig. 5.21. The correction trims sent during the fill by the system correspond very well to the necessary kicks calculated by the off-line orbit analysis. The potentiometer system at IP 8 used at that time shows a bigger noise which causes more trims to be sent. But it is capable of tracking the long term movements well.

Fig. 5.22 shows the evolution of the rms of the vertical orbit readings during this fill. The vertical orbit rms remains small for periods where no orbits were acquired by the operator and no orbit corrections other than from the QS0 system were made. The vertical orbit without correction would have drifted by 2 mm rms in this fill.

The system is compensating well for the movements of the orbit. Up to 70 – 90 % of the drifts are corrected. Only very few additional orbit corrections are needed. So the number of orbit corrections that had to be made by the operator is significantly reduced.

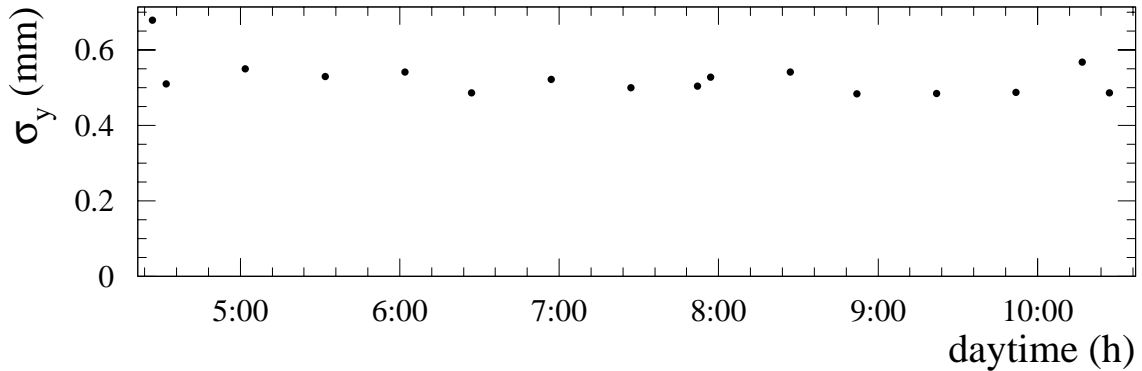


Figure 5.22: Rms value of the vertical orbit readings during a fill (#3706).

5.6 Corrector Reload

The information of the QS0 position has another application. Best reproducible luminosity performance at LEP is obtained using orbits as a reference which gave high luminosity and low background (“Golden Orbit”). This is best and fastest achieved by reloading previously stored set of corrector excitations. Experience showed, however, that there is some risk of beam loss due to the corrector reload.

As the previous analysis has shown, the effect of the changing position of the QS0 magnets can result in rms orbit differences up to $\sigma_{\Delta y} = 3$ to 4 mm. The QS0 positions can be very different for the storage and reload time of the corrector excitations. The set of corrector excitations contains implicitly the correction for the QS0 positions. Reloading the corrector settings for different QS0 positions can thus result in an orbit with excursions of several millimetres. This can cause the beam loss.

The measurements of the QS0 positions can be used to decrease this risk significantly. Whenever a set of corrector excitations is reloaded, the position of the QS0 magnets at storage and reload time are compared and the difference computed. Using the correlations from Section 5.4.1, the necessary correction kick can be calculated and incorporated in the corrector reload.

An experiment was performed at the end of a fill (Fill #3792). Previously stored corrector setting of the preceding days were restored including the calculated correction kick from the QS0 position differences. All orbits after reload showed a reasonably small vertical excursions. The results are summarised in Table 5.3. Figure 5.23 shows an example of the vertical closed orbit readings after reload.

The orbit that would have resulted from the reload without the QS0 correction was calculated. An example is given in Fig. 5.24. In all cases, the orbit excursion was significantly larger with a maximum of 3.7 mm rms.

The incorporation of the difference of the QS0 positions in the vertical corrector reload results in a significantly better closed orbit and hence a smaller risk of beam loss.

The hydrostatic levelling system works well on the timescale of days. It still remains to be tested if the reproducibility stays as good on the timescale of weeks or months. Slower ground motion could change the relative position of the two support structures which is not taken into account for the correction. But the reload with the QS0 correction should be still better than without because it corrects for part of the total movements.

fill #	time	$\sigma_{y,cor}$ [mm]	$\Delta y'_{IP2}$ [μ rad]	$\Delta y'_{IP4}$ [μ rad]	$\Delta y'_{IP6}$ [μ rad]	$\Delta y'_{IP8}$ [μ rad]	$\sigma_{y,sim}$ [mm]
3761	19:40:37	0.665	2.5	-26.7	2.5	-6.7	3.656
3762	09:56:59	0.584	3.6	-27.4	1.2	2.4	3.582
3762	11:26:03	0.611	2.8	-26.0	1.3	3.0	2.162
3787	09:23:50	0.764	-0.1	-14.0	2.4	-4.2	2.335

Table 5.3: Orbit corrector reload experiment. Fill # is of the fill where the set of corrector excitation was stored, $\sigma_{y,cor}$ the vertical rms orbit after reload including the calculated correction kick $\Delta y'$ from the QS0 position differences. $\sigma_{y,sim}$ is the vertical rms orbit that would have resulted from a orbit reload without the QS0 correction.

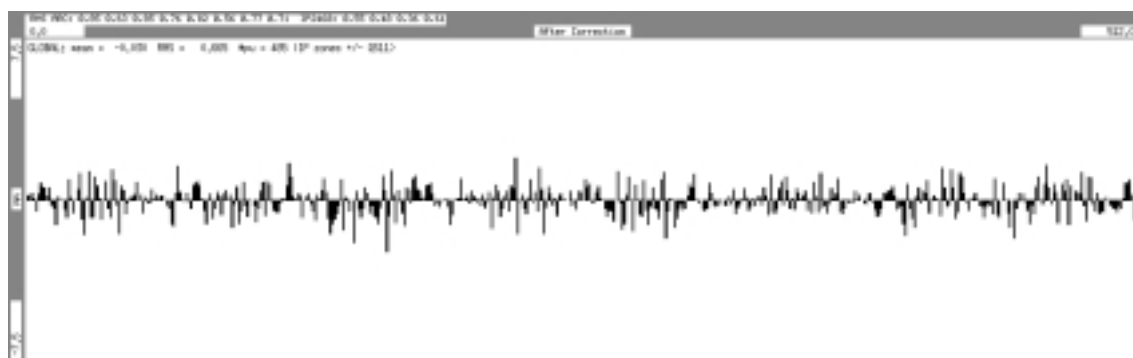


Figure 5.23: BPM readings of the vertical closed orbit after reload of a set of corrector excitations including QS0 correction. The rms is 0.67 mm.

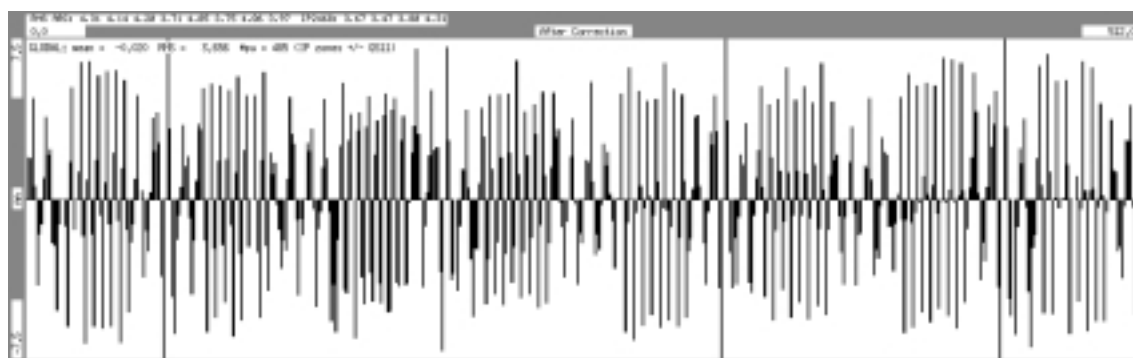


Figure 5.24: Simulated BPM readings of the vertical closed orbit after reload of a set of corrector excitations as in Fig. 5.23 but without QS0 correction. The rms would be 3.66 mm.

Chapter 6

Conclusions

Two new methods have been developed and implemented at LEP to improve the orbit determination and stability:

- A beam based alignment method which measures the offsets between beam position monitors and quadrupole magnets.
- An orbit feedback system based on measurements of the mechanical positions of particular quadrupoles.

The beam based alignment relies on the focusing properties of the quadrupole magnets. The field strength of individual quadrupoles is modulated at low frequencies. This induces orbit oscillations when the beam is not centred in the magnet. The amplitude is proportional to the distance from the magnetic axis. The orbit oscillations are measured for different beam positions in the quadrupole. The offset of the adjacent beam position monitor is deduced from the minimum oscillation amplitude. Simultaneous measurements with different frequencies are performed.

Quadrupole magnets that are connected in series were equipped with additional (back leg) windings for individual modulation. The coupling to the main winding limits the useful excitation frequency range to below 2–3 Hz. The small excitation amplitudes of $\Delta k/k < 10^{-3}$ allow measurements during operation with colliding beams without affecting the LEP performance. The excitation and measurements are synchronised, therefore the calculated phase provides additional information.

A harmonic analysis of the induced orbit oscillation is performed. It makes the calculation of its amplitude independent of the frequency and more precise when compared to an FFT. The convolution of the beam position data with a windowing function significantly reduces the spectral leakage. This avoids cross-talk between nearby measurement frequencies. The choice of the Hamming window permits a frequency spacing of 0.1 Hz. The dense frequency spacing allows the modulation of up to 16 quadrupole magnets by back leg windings simultaneously, being limited only by the number of power converters.

The method is feasible in the presence of orbit drifts and oscillations from other sources. Cuts on orbit position changes and the amplitude of the lowest frequency components reduce the effects from orbit drifts and corrections. The difference between the known excitation frequency and the detected one allows the rejection of measurements perturbed by parasitic oscillations.

Offset determinations were initially relying on orbit drifts. Local closed orbit bumps at the location of the quadrupole under modulation have been used to ensure a successful measurement when the orbit variations were not sufficient.

The offsets measured at LEP depend on the BPM read-out electronics and the magnet type. The superconducting low-beta insertion quadrupoles have the largest offsets. For the LEP I superconducting magnets, the offsets were up to -2 mm with a mean value of -1.18 mm. The new superconducting magnets for LEP II show offsets up to -1 mm with a mean of -0.58 mm. The BPM electronics also contribute to these offsets which vary for different particle types and gain settings. The offsets for normal conducting magnets with the same wide band BPM electronics are notably smaller. The distribution of these offsets has a mean of -0.08 mm with an rms spread of 0.38 mm.

The offsets for normal conducting quadrupoles with narrow band BPM electronics, as for most of the BPMs, are smaller than for the wide band type. The mean offset is -0.03 mm with a spread of 0.24 mm. These offsets are not very large when compared to the typical vertical orbit excursion of 0.5 mm rms for luminosity operation. However, they are extremely important for polarization studies where the orbit is corrected to below 0.25 mm rms.

The impact of the BPM offsets on the achievable polarization level has been studied in simulations. It has been shown that the offsets are particularly important for the correction of depolarizing orbit resonances by Harmonic Spin Matching.

A precise energy measurement at LEP is based on the spin polarization. A level of $4-5\%$ is required for the energy calibration. The strength of the depolarizing resonances grows with the energy. The polarization level is not sufficient for a direct determination of the beam energy for operation above the W-threshold. Measurements at lower energies have to be extrapolated. The BPM offset calibration increases the probability of obtaining polarization at higher energies. The error on the W mass can thus be reduced by shortening the lever arm for the extrapolation.

The offset determination method can be used for the LHC*. Nearly all quadrupoles will be superconducting without direct optical reference to the magnetic centre. Beam based calibration of the BPMs is the only method of verifying the desired alignment. The method described in this work is particularly interesting because of its minor distortion of the beam. A proposal for the excitation of the LHC quadrupoles and first tests are described in [Der96].

The orbit of LEP is slowly drifting in the vertical plane. Without frequent orbit corrections, the drifts would add up to several millimetres during a filling cycle. The vertical orbit motion has been clearly attributed to movements of the low-beta insertion quadrupoles (QS0). They are installed on cantilever support structures. Thermal effects related to the operation cycle of LEP make their position change. The height variations are continuously monitored by different Hydrostatic Levelling Systems. The precision of the HLS is limited by thermal effects changing the density of the water. Measurements by HLS installations with height differences in the connecting tubes have shown an error of at least $\mathcal{O}(10)$ μm and are not used for this application. The other type of HLS systems with horizontal tubes, partially filled with water, has a much better precision of $\mathcal{O}(1)$ μm .

Closed orbits of LEP have been analysed to study the correlation between mechanical and orbit motion in detail. The analysis has shown that the drifts can be sufficiently

*Large Hadron Collider [LHC95]

corrected with four orbit corrector magnets close to the low-beta insertion quadrupoles. The necessary correction kicks are proportional to the differential movements of the quadrupole pair at the respective interaction points. The proportionality factors have been computed from the orbit studies and correspond to results from simulations.

A feedback system based on the HLS measurements has been developed to stabilise the vertical orbit. The orbit correction system calculates the four orbit correction kicks and sends them whenever they exceed a certain threshold. The threshold corresponds to $1\ \mu\text{m}$ differential quadrupole movement or an rms orbit change of $40\ \mu\text{m}$. Since the end of 1996, the system has been successfully used during operation for data taking by the experimental detectors. The system reduces the orbit drifts due to the QS0 movements by about an order of magnitude. This new orbit feedback has significantly improved the orbit stability of LEP and has diminished the number of manual orbit corrections.

Data sets of corrector excitations are stored and reloaded in LEP operation to reproduce orbits which gave a good performance. The reload led occasionally to a loss of the beam. The position differences of the low-beta quadrupole pairs are probably the cause of the losses. The measured QS0 movements have been taken into account for the reload. This has resulted in significantly smaller vertical orbit excursions after reload and a lower risk of beam loss.

Appendix A

Frequency Analysis

A.1 Discrete Harmonic Analysis

The harmonic analysis (see Section 4.3.1) of the transverse beam position $u(t)$ provides the best estimate of the amplitude A and the phase ϕ of a sinusoidal oscillation

$$u(t) = A \cdot \cos(2\pi f_0 t + \phi). \quad (\text{A.1})$$

The function $u(t)$ is sampled at equidistant time intervals $\tau = 1/f_{\text{sampl}}$. The calculation is carried out by computing the real (cosine) and the complex (sine) part of the discrete Fourier Transform (Eq. 4.8)

$$C(f) = \sum_{k=0}^{N-1} u(k\tau) \cdot \cos(2\pi f k\tau) \quad (\text{A.2})$$

$$S(f) = \sum_{k=0}^{N-1} u(k\tau) \cdot \sin(2\pi f k\tau) . \quad (\text{A.3})$$

Replacing $u(k\tau)$ by Eq. 4.7 for a harmonic oscillation, the expression for $C(f)$ taken at the oscillation frequency $f \equiv f_0$ becomes

$$\begin{aligned} C(f) &= \sum_{k=0}^{N-1} A \cdot \cos(2\pi f_0 k\tau + \phi) \cdot \cos(2\pi f k\tau) \quad (\text{A.4}) \\ &= A \sum_{k=0}^{N-1} \frac{\underbrace{\cos(2\pi f k\tau + \phi)}_{\cos(2\pi f k\tau) \cos \phi - \sin(2\pi f k\tau) \sin \phi} \cos(2\pi f k\tau)}{\cos(2\pi f k\tau) \cos \phi - \sin(2\pi f k\tau) \sin \phi} \\ &= A \sum_{k=0}^{N-1} \left[\frac{\underbrace{\cos^2(2\pi f k\tau)}_{\frac{1}{2} + \frac{1}{2} \cos(4\pi f k\tau)}}{\frac{1}{2} + \frac{1}{2} \cos(4\pi f k\tau)} \cos \phi - \frac{\underbrace{\sin(2\pi f k\tau) \cos(2\pi f k\tau)}_{\frac{1}{2} \sin(4\pi f k\tau)}}{\frac{1}{2} \sin(4\pi f k\tau)} \sin \phi \right] \\ &= A \left[\frac{N}{2} \cos \phi + \frac{1}{2} \sum_{k=0}^{N-1} [\cos(4\pi f k\tau) \cos \phi - \sin(4\pi f k\tau) \sin \phi] \right] \\ &= \frac{AN}{2} \left[\cos \phi + \frac{1}{N} \sum_{k=0}^{N-1} \cos(4\pi f k\tau + \phi) \right] \end{aligned}$$

$$\simeq \frac{AN \cos \phi}{2},$$

since the second sum of cosine terms vanishes for a large $N \gg 1$.

Similarly, one get for $S(f)$

$$\begin{aligned} S(f) &= \frac{AN}{2} \left[-\sin \phi + \frac{1}{N} \sum_{k=0}^{N-1} \sin(4\pi f k\tau + \phi) \right] \\ &\simeq -\frac{AN \sin \phi}{2}. \end{aligned}$$

Neglecting terms which vanish for large $N \gg 1$, the amplitude and phase of a signal of frequency f can be calculated by

$$A(f) = \frac{2}{N} \cdot \sqrt{C(f)^2 + S(f)^2} \quad (\text{A.5})$$

$$\phi(f) = -\arctan\left(\frac{S(f)}{C(f)}\right). \quad (\text{A.6})$$

where the quadrant of the phase ϕ can be found by the signs of $S(f)$ and $C(f)$

sign(S)	sign(C)	quadrant of ϕ
-	-	$-\pi < \phi < -\pi/2$
-	+	$-\pi/2 < \phi < 0$
+	+	$0 < \phi < \pi/2$
+	-	$\pi/2 < \phi < \pi$

A.2 Aliasing

For a sampling interval τ exists a critical frequency, $f_N = \frac{1}{2\tau} = \frac{1}{2}f_{\text{sample}}$, known as the Nyquist frequency. If the data under observation is band-limited to a frequency less than the Nyquist frequency that function can be sampled and represented, digitally, in a representation similar to the continuous limit.

When the signal has significant frequency content higher than the Nyquist frequency, aliasing occurs when we perform a discrete Fourier transform. The excess high frequency information is spuriously moved into the valid region between DC and the Nyquist frequency.

The effect of aliasing is that any signal with a frequency $f_s = 2mf_N \pm f$ with $m \in \mathbb{Z}$ is moved to frequency f in the interval $[0..f_N]$. It can be seen from Fig. A.1 that the amplitudes of harmonic signals with the frequency f and $2mf_N \pm f$ are identical at the sampling points.

It can be easily that the amplitudes for signals with frequencies f and $f + 2mf_N$ with $m \in \mathbb{Z}$ are identical. Since $f_N = \frac{1}{2\tau}$, the argument of the trigonometric functions becomes

$$\begin{aligned} 2\pi(f + 2mf_N)k\tau &= 2\pi\left(f + \frac{m}{\tau}\right)k\tau \\ &= 2\pi fk\tau + 2\pi mk \end{aligned}$$

and the result does not change.

The calculated amplitude A for the frequency $-f_0$ is identical to the one for f_0 . With $\cos(-x) = \cos(x)$ and $\sin(-x) = -\sin(x)$ follows from Eq. A.2 in analogy to Eq. A.4

$$\begin{aligned}
 C(f) &= \sum_{k=0}^{N-1} A \cdot \cos(-2\pi f_0 k\tau + \phi) \cdot \cos(2\pi f k\tau) \\
 &= A \sum_{k=0}^{N-1} \underbrace{\cos(-2\pi f k\tau + \phi)}_{\cos(-2\pi f k\tau) \cos \phi - \sin(-2\pi f k\tau) \sin \phi} \cos(2\pi f k\tau) \\
 &= A \sum_{k=0}^{N-1} [\cos^2(2\pi f k\tau) \cos \phi + \sin(2\pi f k\tau) \cos(2\pi f k\tau) \sin \phi] \\
 &\approx \frac{A N \cos \phi}{2},
 \end{aligned}$$

since again the second term vanishes for large $N \gg 1$.

Analogously, $S(f)$ becomes

$$\begin{aligned}
 S(f) &= \sum_{k=0}^{N-1} A \cdot \cos(-2\pi f_0 k\tau + \phi) \cdot \sin(2\pi f k\tau) \\
 &\approx + \frac{A N \sin \phi}{2}.
 \end{aligned}$$

So the result of Eq. A.5 does not change. Only the calculated phase ϕ changes sign.

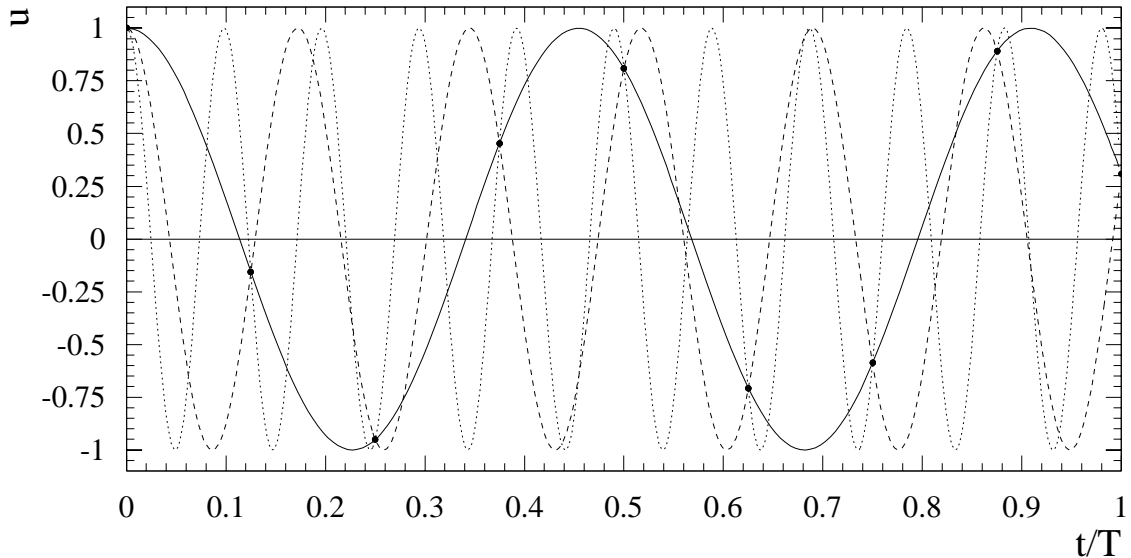


Figure A.1: Illustration of aliasing. The signals shown have the frequencies f , $2f$ and $2f_N + f$. The amplitudes of the different signals are identical at the sampling points.

A.3 Time averaging

A signal with frequency content higher than the Nyquist frequency has to pass a low pass filter to avoid aliasing of frequencies $f > f_N$. A digital low pass filter is a time averager. Instead of transforming the original data, these are averaged for n samples in time intervals of τ/n before the transformation is done.

So the transform is taken of the function

$$\bar{u}(k\tau) = \frac{1}{n} \sum_{j=0}^{n-1} u\left(\left[k + \frac{j}{n}\right] \cdot \tau\right) . \quad (\text{A.7})$$

Substituting the function $u(t)$ by $\bar{u}(t)$ in Eq. 4.8, one obtains for a harmonic signal $u(t) = A \cdot e^{i\omega_s t}$ with $\omega_s = 2\pi f$

$$\begin{aligned} \tilde{\bar{u}}(\omega) &= \sum_{k=0}^{N-1} \frac{1}{n} \sum_{j=0}^{n-1} A e^{i\omega_s(k+\frac{j}{n})\tau} \cdot e^{-i\omega k\tau} \\ &= A \cdot \underbrace{\sum_{k=0}^{N-1} e^{i(\omega_s-\omega)k\tau}}_{\tilde{u}} \cdot \frac{1}{n} \sum_{j=0}^{n-1} e^{i\omega_s \frac{j}{n}\tau} \\ &= \tilde{u} \cdot \frac{1}{n} \sum_{j=0}^{n-1} e^{i\omega_s \frac{j}{n}\tau} \\ &= \tilde{u} \cdot \frac{1}{n} \cdot \frac{1 - e^{in\omega_s \frac{1}{n}\tau}}{1 - e^{i\omega_s \frac{1}{n}\tau}} \\ &= \tilde{u} \cdot e^{i\omega_s \frac{1}{2}(1-\frac{1}{n})\tau} \cdot \frac{\sin\left(\frac{\omega_s \tau}{2}\right)}{n \cdot \sin\left(\frac{\omega_s \tau}{2n}\right)} \\ &\simeq \tilde{u} \cdot e^{i\left(1-\frac{1}{n}\right)\frac{\omega_s \tau}{2}} \cdot \frac{\sin\left(\frac{\omega_s \tau}{2}\right)}{\frac{\omega_s \tau}{2}} \quad \text{for } \frac{\omega_s \tau}{2n} \ll 1. \end{aligned}$$

The resulting amplitude \bar{A} of this transform of an averaged sinusoidal signal is attenuated by a factor $a(f/f_{\text{sampl}})$

$$\bar{A}(f) = a(f/f_{\text{sampl}}) \cdot A(f) \quad a(f/f_{\text{sampl}}) = \left| \frac{\sin(\pi f/f_{\text{sampl}})}{n \sin(\pi/n \cdot f/f_{\text{sampl}})} \right| \quad (\text{A.8})$$

Fig A.2 shows an example of Eq. A.8. The factor a has the periodicity of n and is symmetric around $n/2$.

In the limit of $\frac{\omega_s \tau}{2n} \ll 1$ which is well fulfilled for the modulation frequencies used for the offset determination the amplitude is attenuated according to

$$\bar{A}(f) = A(f) \cdot \left| \frac{\sin(\pi f \tau)}{\pi f \tau} \right| \quad (\text{A.9})$$

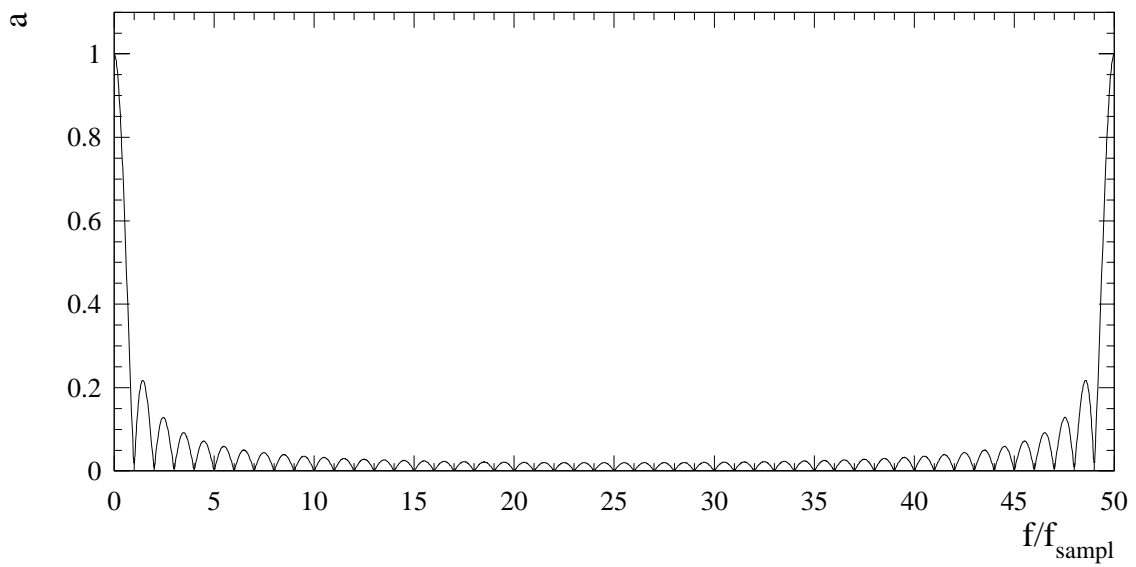


Figure A.2: Averaging effect as a function of f/f_{sampl} for $n=50$.

Appendix B

Hydrostatic Levelling System

B.1 Database tables

The information of the hydrostatic levelling systems is logged in the LEP measurement database. There is a table with the actual values (M_HLS) and a history table (M_HLS_HIST). The values logged in the database table are given in Table B.1.

A database trigger puts the values into the history table every 10 minutes or when the values have changed more than a certain threshold. The status value is 0 if the measurement was valid. In case of problems it is set to -1000 .

The system at IP 8 is still slightly different from the other interaction points. Only

IP	NUMBER(4)	– interaction point number
TIMESTAMP	DATE	
P1	NUMBER(8,4)	– position values for the different HLS probes
⋮		
P12	NUMBER(8,4)	
RMS1	NUMBER(7,4)	– rms of position values for the different probes
⋮		
RMS12	NUMBER(7,4)	
T1	NUMBER(6,2)	– temperatures of the probes
⋮		
T12	NUMBER(6,2)	
SE1	NUMBER(6,2)	– temperature of connecting tubes (see drawing)
⋮		
SE5	NUMBER(6,2)	
SA1	NUMBER(6,2)	– air temperature (see drawing)
⋮		
SA6	NUMBER(6,2)	
SP	NUMBER(7,3)	– water pressure
STAT	NUMBER(5)	– status of the valves

Table B.1: Database table for the hydrostatic levelling system data.

the values P5 .. P12 and the corresponding temperature values of the vessels are logged on-line in the database.

A description of the hydrostatic levelling system can be found in [WWW96].

B.2 HLS layout

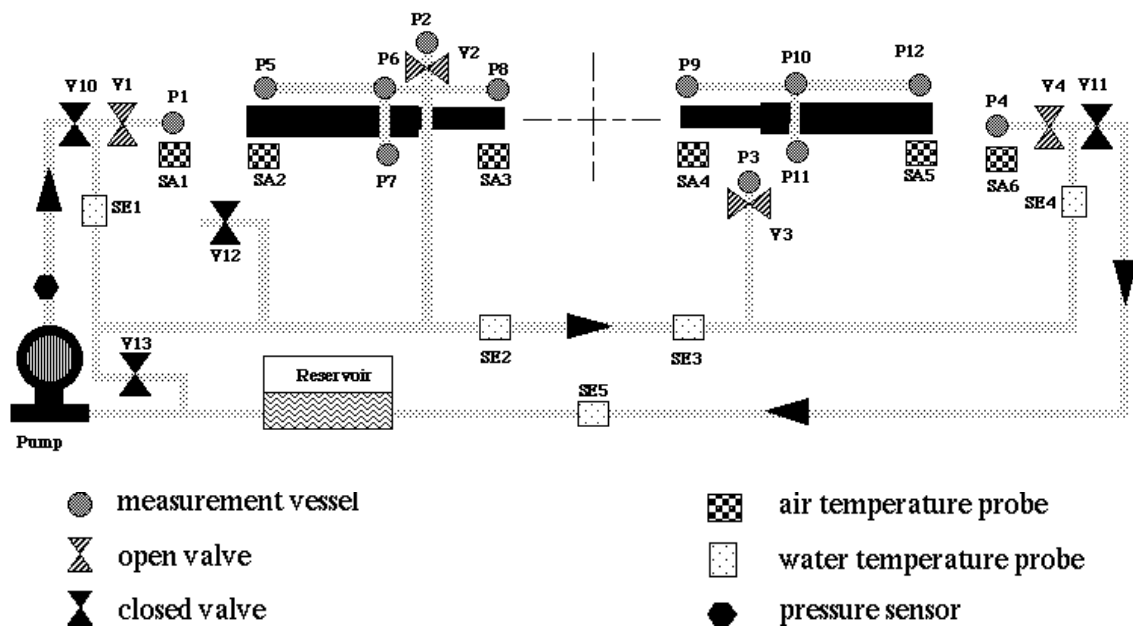


Figure B.1: Schematic view of the hydrostatic levelling system installation at IP 2.

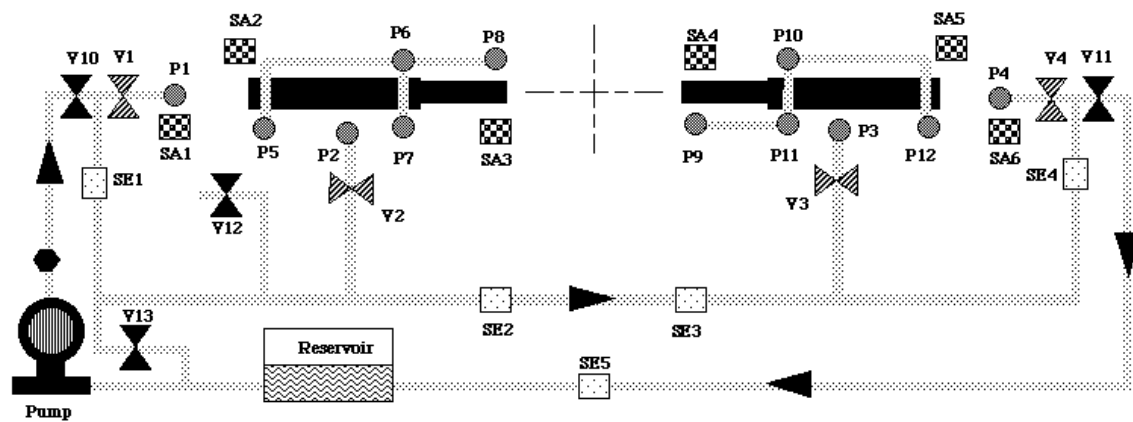


Figure B.2: Schematic view of the hydrostatic levelling system installation at IP 4.

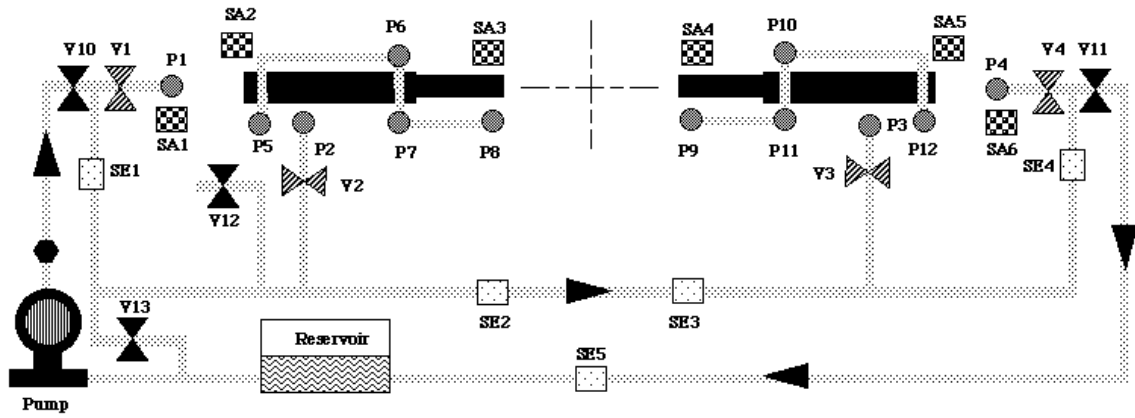


Figure B.3: Schematic view of the hydrostatic levelling system installation at IP 6 and IP 8 (new layout).

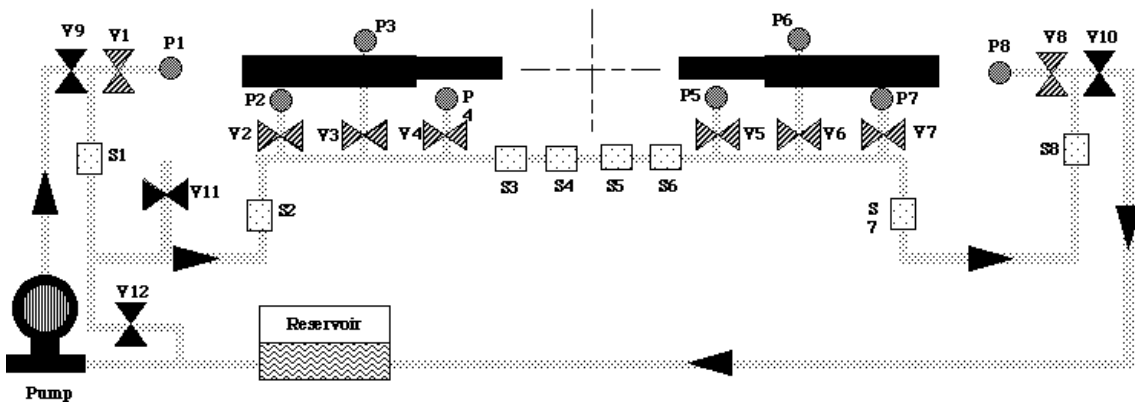


Figure B.4: Schematic view of the hydrostatic levelling system installation at IP 8 before the modification for the 1997 running period.

B.3 Proportionality factors

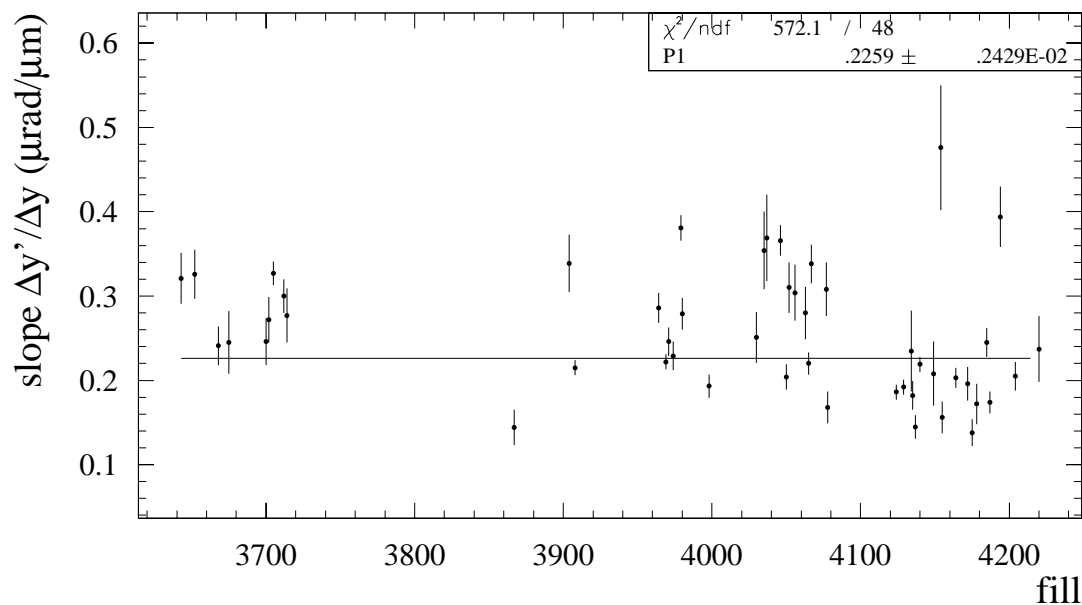


Figure B.5: Proportionality factors between the observed movements and calculated orbit correction kicks at IP2. The factors are shown as a function of the fill for the 1996 and 1997 running period. Only fills where the calculated kick exceeded $\Delta y' = 5 \mu\text{rad}$ are shown.

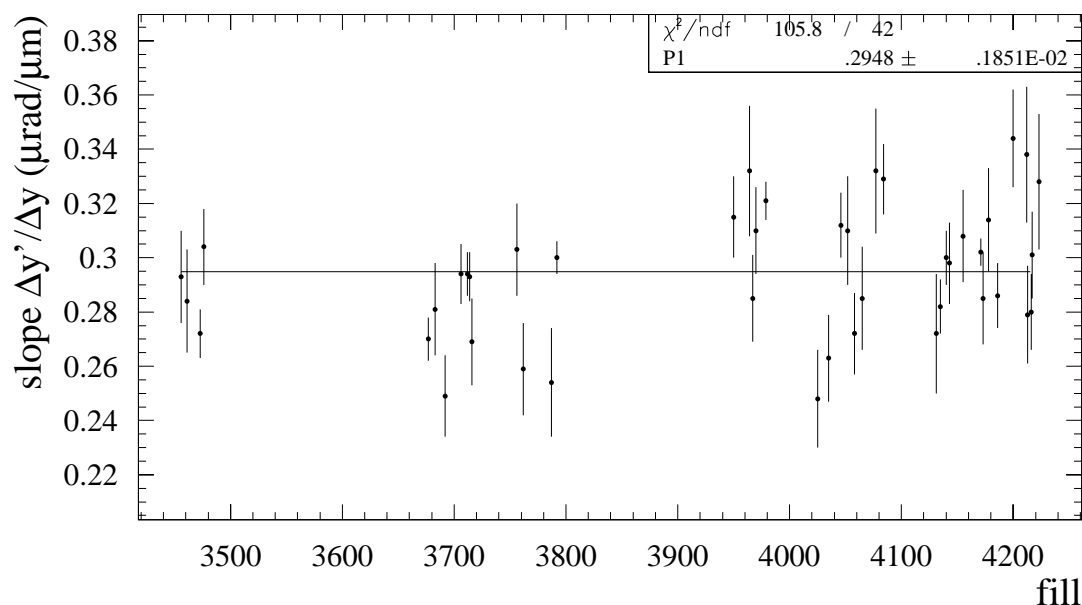


Figure B.6: Proportionality factors between the observed movements and calculated orbit correction kicks at IP4. The factors are shown as a function of the fill for the 1996 and 1997 running period. Only fills where the calculated kick exceeded $\Delta y' = 8 \mu\text{rad}$ are shown.

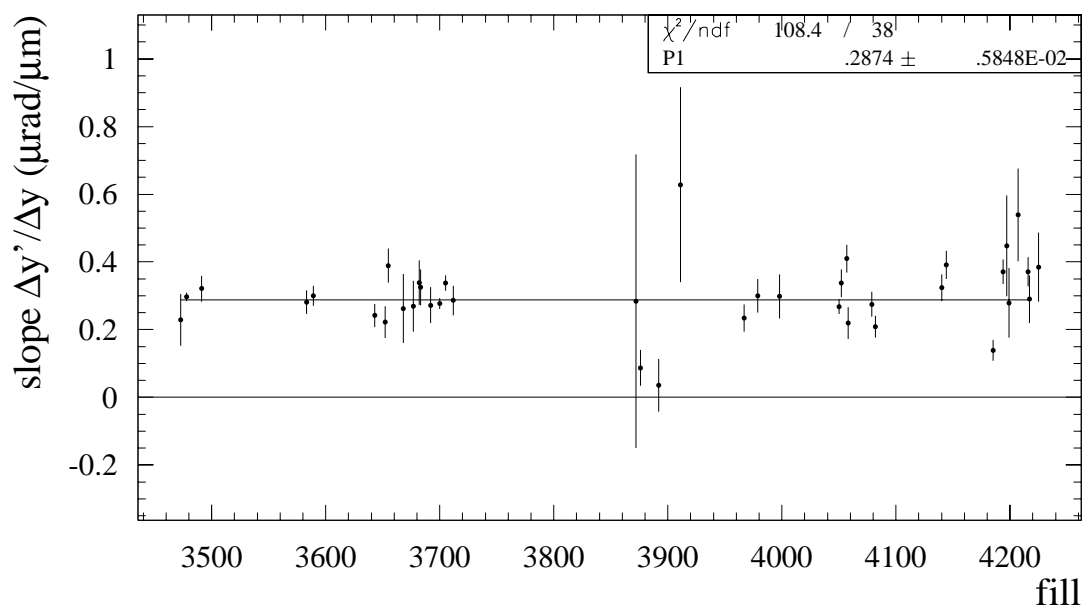


Figure B.7: Proportionality factors between the observed movements and calculated orbit correction kicks at IP 6. The factors are shown as a function of the fill for the 1996 and 1997 running period. Only fills where the calculated kick exceeded $\Delta y' = 2.5 \mu\text{rad}$ are shown.

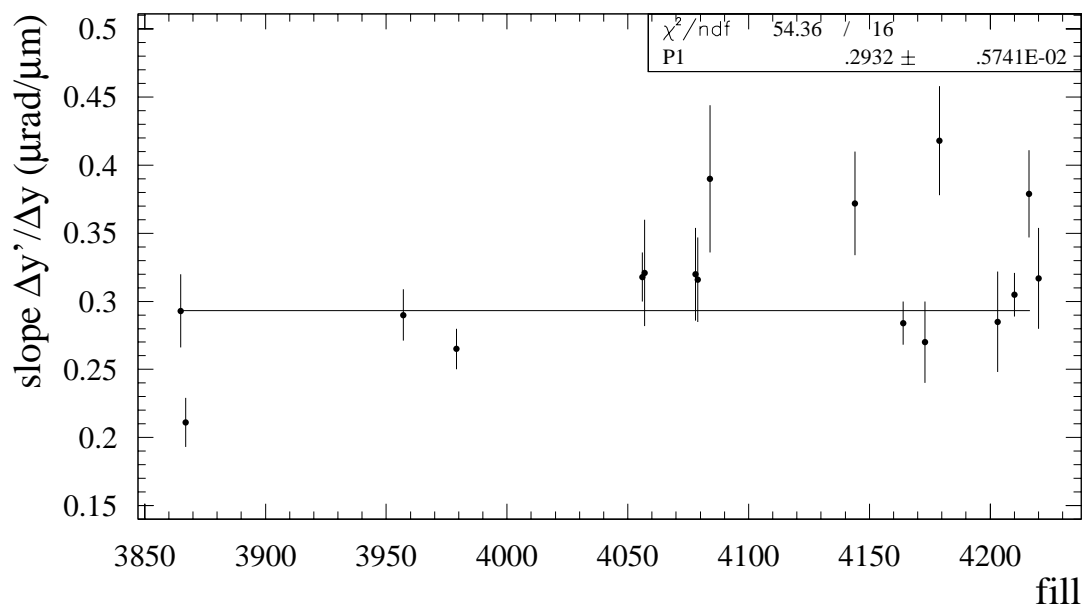


Figure B.8: Proportionality factors between the observed movements and calculated orbit correction kicks at IP 8. The factors are shown as a function of the fill for the 1997 running period. Only fills where the calculated kick exceeded $\Delta y' = 5 \mu\text{rad}$ are shown.

Bibliography

- [Alt96] G. Altarelli, T. Sjöstrand, and F. Zwirner, editors, *Physics at LEP2*, volume 1 of *CERN 96-01*, (1996).
- [Arn95] L. Arnaudon *et al.*, “Accurate Determination of the LEP Beam Energy by Resonant Depolarization”, *Z. Phys. C* **66**, 45 (1995).
- [Ass93] R. Assmann, “Results of Polarization and Optimization Simulations”, in *Proceedings of the Third Workshop on LEP Performance*, pp. 341–356, (1993), CERN SL/93-19 (DI).
- [Ass94a] R. Assmann, *Optimierung der transversalen Spin-Polarisation im LEP-Speicherring und Anwendung für Präzisionsmessungen am Z-Boson*, PhD thesis, Ludwig-Maximilians-Universität München, (1994), in German.
- [Ass94b] R. Assmann *et al.*, “Polarization Studies at LEP in 1993”, CERN SL/94-08 (AP), (1994).
- [Aut73] B. Autin and Y. Marti, “Closed Orbit Correction of A.G. Machines Using a Limited Number of Magnets”, (1973), CERN ISR MA/73-17.
- [Bai66] V. Baier and Y. Orlov, “Quantum Depolarization of Electrons in a Magnetic Field”, *Sov. Phys. Dokl.* **10**, 1145 (1966).
- [Bar59] V. Bargmann, L. Michel, and V. Telegdi, “Precession of the Polarization of Particles Moving in a Homogeneous Elektromagnetic Field”, *Phys. Rev. Lett.* **2**, 435 (1959).
- [Bar94] I. Barnett *et al.*, “Dynamic Beam Based Alignment”, in *6th Workshop on Beam Instrumentation Vancouver, Canada, AIP conf. proc. ; no 333*, pp. 530–535, (1994), CERN SL/94-84 (BI).
- [Bee90] G. Beetham and B. Puccio, “TG3-V VME Timing Module”, SL/CO Note 90-1, (1990).
- [Beu93] A. Beuret, P. Castro, M. Placidi, R. Schmidt, and J. Wenninger, “Experiments on K-Modulation in MD Week 31, 1993”, (1993), SL-MD Note 104.
- [Bil90] J. Billan, J. Gourber, K. Henrichsen, and L. Walkiers, “Field Display System for the Forecast of Beam Momentum and Betatron Frequencies in LEP”, *Part. Acc.* **29**, 215 (1990).

- [Bög94] M. Böge, *Analysis of Spin Depolarizing Effects in Electron Storage Rings*, PhD thesis, Universität Hamburg, (1994), DESY 94-087.
- [Bög95] M. Böge and R. Brinkmann, “*Optimization of Spin Polarization in the HERA Electron Ring using Beam-Based Alignment Procedures*”, in *AIP Conference Proceedings 343, High Energy Spin Physics, Bloomington 1994*, pp. 287–293, (1995).
- [Bor90] J. Borer, “*Instrumentation and Diagnostics used in LEP Commissioning, with Accent on the LEP Beam Orbit Measurement System*”, CERN SL/90-107 (BI), (1990).
- [Bor95] J. Borer, D. Cocq, A. Manarin, and G. Vismara, “*The Second Generation and Optimized Beam Orbit Measurement (BOM) System of LEP: Hardware and Performance Description*”, CERN SL/95-60 (BI), (1995).
- [Bra90] D. Brandt, W. Herr, J. Miles, and R. Schmidt, “*A New Closed Orbit Correction Procedure for the CERN SPS and LEP*”, *Nucl. Instr. Meth. A*(293), 305 (1990).
- [Buo89] J. Buon, “*A Stochastic Model of Depolarization Enhancement due to large Energy Spread in Electron Storage Rings*”, in *8th International Symposium on High-energy Spin Physics, Minneapolis, 1988*, K. Heller, ed., volume 187 of *AIP conf. proc.; Particles and fields subser.; no 37*, pp. 963–974, (1989).
- [Bur95] H. Burkhardt, “*What Affects the Stability of LEP?*”, in *Proceedings of the fifth Workshop on LEP Performance*, pp. 14–17, (1995), CERN SL/95-08 (DI).
- [Buu92] G. Buur, P. Collier, K. Lohmann, and H. Schmickler, “*Dynamic Tune and Chromaticity Measurements in LEP*”, in *Proceedings EPAC 92*, pp. 1043–1045, (1992).
- [Cam95] T. Camporesi, F. Harris, E. Migliore, and E. Vallazza, “*Beam Spot Estimation in DELPHI with QSO Position Probes and the LEP BOM System*”, (1995), DELPHI 95-162 LEDI 95-3.
- [Cha81] A. Chao, “*Evaluation of Radiative Spin Polarization in an Electron Storage Ring*”, *Nucl. Instr. Meth.* **180**, 29 (1981).
- [Cha82] A. Chao, “*The SLIM Program and its Limitations*”, in *Workshop on polarized electron acceleration and storage*, (1982), DESY M-82/09.
- [Col95] P. Collier, “*Overview of Operation in Physics During 1994*”, in *Proceedings of the fifth Workshop on LEP Performance*, pp. 92–95, (1995), CERN SL/95-08 (DI).
- [Cou58] E. Courant and H. Snyder, “*Theory of the Alternating Gradient Synchrotron*”, *Ann. of Physics* **3**(1) (1958).

- [Deh95] B. Dehning, *Elektronen- und Positronen-Polarisation im LEP-Speicherring und Präzisionsbestimmung der Masse des Z-Teilchens*, PhD thesis, Ludwig-Maximilians-Universität München, (1995), in German.
- [Deh96] B. Dehning, A. Drees, and M. Geitz, “A Study of the Magnetic Dipole Field of LEP During the 1995 Energy Scan”, CERN SL/96-54 (BI), (1996).
- [Der70] Y. Derbenev, A. Kondratenko, and A. Skrinskii, “The Motion of Particle Spin in an Accelerator with Arbitrary Field”, *Sov. Phys. Dokl.* **15**(6), 583 (1970).
- [Der79] Y. Derbenev, A. Kondratenko, and A. Skrinskii, “Radiative Polarization at Ultra-High Energies”, *Part. Acc.* **9**, 247 (1979).
- [Der96] J. Deregel, P. Galbraith, P. Genevey, K. Henrichsen, and J.-M. Rifflet, “Proposal of a K-Modulation System for the LHC Quadrupoles”, LHC Project Report 4, CERN, (1996).
- [End95] K. Endo, R. Sugahara, and Y. Ohsawa, “Thermally Driven Vertical Displacement of IP Quadrupole Magnet”, in *Proceedings of the Fourth International Workshop on Accelerator Alignment, KEK Proceedings 95-12*, pp. 77–85, (1995).
- [Fog] Fogale Nanotech, 190, Parc Georges Besse, 30000 Nimes, France, *Sensors and Actuators for Alignment of Large Machine Components*.
- [Gla70] S. Glashow, J. Iliopoulos, and L. Maiani, “Weak Interactions with Lepton - Hadron Symmetry”, *Phys. Rev.* **D2**, 1285 (1970).
- [Gro90] H. Grote and F. Iselin, *The MAD Program*, (1990), CERN SL/90-13 (AP).
- [Har78] F. Harris, “On the Use of Windows for Harmonic Analysis with the Discrete Fourier Transform”, *Proc. of IEEE* **66**(1) (1978).
- [Her94] W. Herr, “Bunch Trains Without a Crossing Angle”, in *Proceedings of the Fourth Workshop on LEP Performance, CERN SL/94-06 (DI)*, pp. 323–332, (1994).
- [Hol96] G. Holtey, “Interaction Regions”, In Altarelli et al. [Alt96], pp. 45–57, CERN 96-01.
- [Iva48] D. Ivanenko and A. Sokolov, *Doklady Akad. Nauk (SSSR)* **59**, 1551 (1948).
- [Jow91] J. Jowett, “8-Bunch Pretzel Scheme, Description”, in *Proceedings of the First Workshop on LEP Performance, CERN SL/91-23 (DI)*, pp. 295–318, (1991).
- [Kew83] J. Kewisch, “Simulation of Electron Spin Depolarization with the Computer Code SITROS”, DESY 83-032, (1983).
- [Kou88] J.-P. Koutchouk, “Systematic Integer Spin Resonances”, in *High Energy Spin Physics*, K. Heller, ed., volume 2 of *AIP Conf. Proceedings No. 187*, pp. 1004–1012, (1988).

- [Kun96] Z. Kunszt and W. Stirling, “*Determination of the Mass of the W Boson*”, In Altarelli et al. [Alt96], pp. 141–205.
- [LEP84] “*LEP Design Report*”, CERN-LEP/84-01, (1984), Vol. I, II.
- [LEP95] LEP Electroweak Working Group, “*A Combination of Preliminary LEP Electroweak Measurements and Constraints on the Standard Model*”, CERN/PPE 95-172, (1995).
- [LEP96] “*LEP Design Report*”, CERN-AC/96-01 (LEP2), (1996), Vol. III.
- [LHC95] “*LHC The Large Hadron Collider, Conceptual Design*”, CERN/AC/95-05 (LHC), (1995).
- [Lit85] R. Littauer, “*Report of Machine Workshop on the 6-GeV Synchrotron Radiation Source*”, (1985), Appendix D-3.
- [Man90] S. Mane, “*Synchrotron Sideband Spin Resonances in High-Energy Electron Storage Rings*”, *Nucl. Instr. Meth.* **292**, 52 (1990).
- [Mar89a] A. Marin, O. Pagano, and L. Vuffray, “*A Position Detector for the L3 Support Tube*”, (1989), internal note CERN/LEP-MA/op.
- [Mar89b] A. Marin, O. Pagano, and L. Vuffray, “*A VME-based Control System for the Positioning of L3 Support Tube*”, (1989), internal note CERN/LEP-MA/op.
- [Mon84] B. Montague, “*Polarized Beams in High Energy Storage Rings*”, *Physics Reports* **113**(1), 1 (1984).
- [Moo95] C. D. Moore, “*Vibrational Analysis of Tevatron Quadrupoles*”, in *Proceedings of the Fourth International Workshop on Accelerator Alignment, KEK Proceedings 95-12*, pp. 119–131, (1995).
- [Pla96] M. Placidi, “*Beam Energy Measurement at LEP2*”, in *Physics at LEP2*, volume 1, pp. 59–74, (1996), CERN 96-01.
- [Rei94] I. Reichel, “*Beam Position Measurement by Modulation of Quadrupole Strengths*”, Diplomarbeit, Pitha Nr. 94/54, RWTH Aachen, (1994), also CERN SL/95-50.
- [Ric83] D. Rice *et al.*, “*Beam Diagnostic Instrumentation at CESR*”, *IEEE Transactions on Nuclear Science* **NS-30**(4), 2190 (1983).
- [Röj94] P. Röjssel, “*A Beam Position Measurement System Using Quadrupole Magnets Magnetic Centra as the Position Reference*”, *Nucl. Instr. Meth. Phys. Res.* **A**(343), 374 (1994).
- [Ros85] R. Rossmanith and R. Schmidt, “*Compensation of Depolarizing Effects in Electron Positron Storage Rings*”, *Nucl. Instr. Meth. Phys. Res.* **A**(236), 231 (1985).
- [Sal68] A. Salam, “*Weak and Electromagnetic Interactions*”, in *Elementary Particle Theory*, W. Svartholm, ed., p. 367. Almqvist and Wiksell, Stockholm, (1968).

- [San70] M. Sands, “*The physics of Electron Storage Rings - An Introduction*”, SLAC-121, UC-28, (1970).
- [Sch82] R. Schmidt, *Polarisationsuntersuchungen am Speicherring PETRA*, PhD thesis, Universität Hamburg, (1982), DESY M-82-22, in German.
- [Sch93] R. Schmidt, “*K-Modulation Discussion*”, Notes of the 1st meeting of the k-modulation project, (1993).
- [Sch95] O. Schneider and R. Forty, “*Beam Position Determination at IP4 Using LEP BOM Data and QSO Position Measurements*”, (1995), ALEPH 95-122, BOM 95-003.
- [Sok64] A. Sokolov and I. Ternov, “*On Polarization and Spin Effects in the Theory of Synchrotron Radiation*”, *Sov. Phys. Dokl.* **8**, 1203 (1964).
- [Son98] F. Sonnemann, “*Increase of Spin Polarization for Energy Calibration at LEP*”, Diplomarbeit, RWTH Aachen, (1998), to be published.
- [Tec96] F. Tecker, “*Low-Beta Quadrupole Movements as Source of Vertical Orbit Drifts at LEP*”, (1996), CERN-SL/96-40 (BI).
- [Tho27] L. Thomas, *Philos. Mag.* **3**, 1 (1927).
- [Uyt97] J. Uythoven, “*A LEP (60,60) Optics for Energy Calibration Measurements*”, CERN SL/97-58 (OP), (1997).
- [Vos94] L. Vos, “*Ground Motion in LEP and LHC*”, CERN SL/94-69, (1994).
- [Wei67] S. Weinberg, “*A Model of Leptons*”, *Phys. Rev. Letters* **19**, 1264 (1967).
- [Wen96] J. Wenninger, “*New Tools for Beam-beam Optimisation*”, in *Proceedings of the Sixth Workshop on LEP Performance*, pp. 16–20, (1996), CERN SL/96-05 (DI).
- [Wie93] H. Wiedemann, *Particle Accelerator Physics, Basic Principles and Linear Beam Dynamics*, Springer-Verlag, Berlin (1993).
- [Wil92] K. Wille, *Physik der Teilchenbeschleuniger und Synchrotronstrahlungsquellen*, Teubner Studienbücher, Stuttgart (1992), in German.
- [WWW96] “*LEP Hydrostatic Levelling Systems*”, <http://www.cern.ch/CERN/Divisions/SL/groups/bi/hls/WelcomeHLS.html>, (1996).
- [Yok83] K. Yokoya, “*Effects of Radiative Diffusion on the Spin-Flip in Electron Storage Rings*”, *Part. Acc.* **14**, 39 (1983).

Acknowledgements

I would like to express my gratitude to Mr. Priv. Doz. Dr. Manfred Tonutti for his constant support during my studies and this thesis. His initiative opened the possibility for me to work at CERN.

I thank Dr. Rüdiger Schmidt for his supervision of my work in the doctoral student programme at CERN. He was a steady source of ideas and his hints triggered part of this work. I enjoyed very much the vivid discussions with him.

I am very grateful to Dr. Bernd Dehning with whom I discussed many parts of this work in detail.

I would like to show my appreciation to Dr. Claude Bovet for my integration in the Beam Instrumentation group.

I owe Dr. Jörg Wenninger a debt of gratitude for his help and for implementing the feedback in the operation software of LEP.

I thank Antonio Marin, Willieme Coosemans, Kirill Rybaltchenko and Pierre Charrue for their work on the installation, maintenance and software of the Hydrostatic Levelling Systems.

During my stay at CERN, I very much appreciated the company – at work and in free time – of my colleagues and friends Dr. Angelika Drees, Natalie Pocock, Dr. Michael Böge, Enrico Bravin, Dr. Pedro Castro, Marc Geitz, Dr. Massimo Placidi, Dr. Patrick Puzo and Florian Sonnemann.

Last but not least, I would like to thank anybody else in the SL division and at the RWTH Aachen who gave me support or help in any way.

Lebenslauf

- | | |
|--------------|---|
| 12 März 1968 | Geboren in Haan als Sohn der Eheleute Günter Tecker und Marlis Tecker, geborene Herzog |
| August 1974 | Einschulung in die Grundschule Bollenberg, Haan |
| Mai 1987 | Abitur am Städtischen Gymnasium Haan |
| Juli 1987 | Wehrdienst |
| Oktober 1988 | Beginn des Studiums der Physik an der RWTH Aachen |
| Oktober 1990 | Vordiplom in Physik |
| Juli 1992 | Aufenthalt am europäischen Forschungslabor CERN in Genf
Diplomarbeit in der <i>Beam Instrumentation Group</i> der
SL Division (SPS und LEP) |
| Juni 1994 | Diplom in Physik |
| Juni 1994 | Aufenthalt am CERN, Genf |